University of Leoben


Doctoral Thesis

# Two-Phase Flow Investigations of Gas-Kick Scenarios

*Application of Computational Fluid Dynamics to Kick Analysis in Wellbores*

**Claudia Carina Gruber**

A thesis submitted in partial fulfilment of the requirements for the degree of
"Doktor der montanistischen Wissenschaften"

Leoben, May 2016

I declare in lieu of oath, that I wrote this thesis and performed the associated research myself, using only literature cited in this volume.

……

Claudia Gruber, Leoben, May 2016

# DANKSAGUNG

Viele Menschen haben dazu beigetragen, dass diese Dissertation entstehen konnte.

Herrn Prof. Wilhelm Brandstätter möchte ich für die Betreuung dieser Arbeit danken, sowie für die Möglichkeit der mittlerweile langjährigen Mitarbeit in seinem Arbeitskreis. Durch ihn erhielt ich viele interessante Einblicke in die angewandte Thermofluiddynamik und konnte mir durch seine Unterstützung eine gut fundierte Wissensbasis aneignen. Er hat diese Arbeit in vielfältiger Weise unterstützt, nicht zuletzt auch in organisatorischer und menschlicher Hinsicht.

Im Besonderen möchte ich mich bei Prof. Gerhard Thonhauser für die freundliche Unterstützung zur Fertigstellung dieser Arbeit bedanken. Ich danke Herrn Dr. Hermann Spörker für die Initiative sowie der OMV für die finanzielle Unterstützung dieser Arbeit. Des Weiteren möchte ich mich bei allen Mitarbeitern des Lehrstuhls für die gute und freundliche Arbeitsatmosphäre bedanken, die ich stets sehr zu schätzen wusste.

Mein besonderer Dank gilt meiner Familie. Im Speziellen meinen beiden Kindern, Ines und Daniel. Die für mich stets eine große Unterstützung waren, und mir den nötigen Antrieb gaben diese Arbeit fertigzustellen.

# ABSTRACT

Common approaches in kick modeling are based on the assumption of a more or less single "gas bubble" present in the annulus and slowly migrating upwards after shut-in. While this assumption satisfies straightforward volumetric well control aspects, it ignores species transport and chemical reaction kinetics leading to drill string corrosion. Especially when dealing with sour gas influxes, the assessment of corrosive damage to high-strength drill string components caused by sulfide stress cracking becomes essential. Therefore a better insight on the flow morphology and associated mechanisms during a kick event is needed to assess the associated corrosive risk.

The aim of the work presented in this thesis is to provide a better understanding of the two-phase flow situation resulting from selected kick scenarios. A Computational Fluid Dynamics (CFD) approach was chosen to simulate the dissolution and distribution of influx gas. The selection of a two-phase flow model within CFD is usually based on the expected flow pattern. Since a gas-kick is a fundamentally transient event accompanied by many unknowns the intention was not to make any a-priory assumptions regarding the evolving flow field. Consequently the focus was put on a spatially highly resolved computational model combined with the application of the Volume of Fluid Method. Thereby no restriction on specific flow patterns was active and two-phase interactions could be observed at a close-up view. However the involved computational costs demanded a limitation in model size to the near bottom-hole section of the wellbore. This section shows certain characteristics that are dominated by the inflow conditions of the gas as well as by the configuration of the mud stream entering the annulus.

Several inflow scenarios are investigated and methodologies are described to characterize flow aspects that are of potential interest to corrosion engineers. One of the major difficulties in modeling the corrosive risk to the drill string during a gas-kick is the determination of liquid-gas phase interface. As mass transfer and significant chemical reactions are related to the size of the phase interface area, a sound estimate of the same is of utmost importance. Simulation results illustrate two-phase flow morphology and associated specific phase interface area, as well as local mass transfer coefficients and the distribution of dissolved gas. The transient and spatial change of flow patterns in a wellbore during a kick event is discussed. It is explained how the flow pattern is affected by gas expansion and how it may be influenced by gas dissolution. Finally based on the findings of the detailed simulation studies, a coarser full scale kick modeling approach covering the entire wellbore is suggested.

# ZUSAMMENFASSUNG

Bei der Modellierung von plötzlichen Gaseintritten in Bohrlöchern wird oftmals von der Annahme ausgegangen, dass sich das eingetretene Gas nach Verschluss des Bohrlochs wie eine zusammenhängende Blase verhält während ihres Aufstiegs im Ringspalt. Für eine rein volumetrische Betrachtungsweise ist diese Annahme ausreichend, allerdings werden hierbei der Transport chemischer Spezies und mögliche chemische Reaktionen welche zu Korrosionsschäden am Bohrstrang führen nicht berücksichtigt. Vor allem wenn Sauergas bei der Bohrung angetroffen wird, ist es wesentlich den möglichen Schaden bedingt durch Spannungsrisskorrosion am aus hoch-festen Stählen bestehenden Bohrgestänge abzuschätzen. Folglich ist klares Verständnis der Strömungsverhältnisse, und damit verbundenen Vorgänge während eines Gaseintritts, zur besseren Einschätzung eines etwaigen Korrosionsrisikos notwendig.

Ziel der vorliegenden Arbeit ist es, ein besseres Verständnis für die gegenständliche Zweiphasenströmung anhand ausgewählter Kick-Szenarien zu vermitteln. Mittels numerischer Strömungssimulation wird die Phasenverteilung und Löslichkeit des Gases berechnet. Grundsätzlich erfolgt die Auswahl eines geeigneten Zweiphasen-Modellierungsansatzes basierend auf einer a-priori Annahme der Strömungsverhältnisse. Da es sich bei einem plötzlichen Gaseintritt allerdings um ein fundamental transientes Ereignis begleitet von diversen Unbekannten handelt ist von einer Vorwegnahme oder Einschränkung des Strömungsbildes abzusehen. Der Einsatz eines hoch-auflösenden Berechnungsgitters in Verbindung mit der Volume of Fluid Methode ermöglicht eine detailreiche und uneingeschränkte Nachbildung beliebiger Strömungsmuster. Allerdings verlangt der damit verbundene erhöhte Berechnungsaufwand eine Einschränkung in der Modellgröße auf den unmittelbaren Bereich ab Bohrlochsohle. Dieser Abschnitt des Bohrlochs zeigt besondere Strömungscharakteristika aufgrund des Gaseintritts sowie der Strömungsmuster bedingt durch die Umlenkung der Bohrspülung.

Verschiedene Gaseintrittsszenarien werden untersucht und Methoden zur Charakterisierung korrosionsrelevanter Strömungsparameter beschrieben. Die Bestimmung der Phasengrenzfläche zwischen Bohrspülung und Gas stellt dabei die größte Herausforderung dar. Eine möglichst genaue Bestimmung der Phasengrenzfläche ist deshalb so bedeutend, da mit ihrer Ausdehnung wesentliche Mechanismen wie Stoffübergang und chemische Reaktionen korrelieren. Die Simulationsergebnisse illustrieren das Erscheinungsbild der Zweiphasenströmung, sowie die damit verbundene Phasengrenzfläche, die lokalen Stoffaustauschkoeffizienten und die Verteilung des gelösten Gases. Die zeitliche und örtliche Änderung der Strömungsmuster im Bohrloch während eines plötzlichen Gaseintritts wird diskutiert. Der Einfluss der Dichteänderung der aufsteigenden Gases sowie der Gaslöslichkeit auf das Erscheinungsbild der Strömung wird beschrieben. Basierend auf den Erkenntnissen der Detailstudien wird ein möglicher Ansatz zur Modellierung des gesamten Bohrlochs vorgeschlagen.

*für Ines und Daniel*

# TABLE OF CONTENTS

# 1.Introduction

## *Background*

During drilling operations the control of the well at all times is of utmost importance. Consequences of a loss in well control can be devastating for the drilling rig, the crew and the environment. The loss of well control can be initiated by the inflow of formation fluids into the well encountered when drilling into formations with pressures higher than anticipated. Such a fluid intrusion is called a kick.

Gas-kicks are especially dangerous because gas reduces the wellbore pressure more quickly than liquids do and confinement at the surface is more difficult. Thus, gas-kicks more often result in loss of well control and in surface fires and explosions. Therefore formation fluids that have flowed into the wellbore and begin displacing the drilling fluid must be removed quickly. Emergency procedures to manage the unexpected inflow and its effects are referred as well-control operations. Common procedures like “wait and weight” and drillers method have been applied successfully over decades to remove formation fluids from the wellbore.

However the physical phenomena occurring thereby are still purely understood, in particular the movement and distribution of the kick fluids as they are pumped to the surface. Often kick detection methods are too slow and inaccurate. Several minutes may elapse before a kick is detected at the surface. During this time a considerable amount of gas may find its way into the wellbore and can cause a hazardous situation.

Apart from the efforts taken to regain well control, a kick can also have a considerable impact with respect to corrosion. The inflow of formation fluid may even be so low and occurring continuously that it is not identified directly as a kick but still poses an issue in terms of corrosion. Numerous conditions encountered during drilling operations cause corrosion to the drilling equipment and can be differentiated by their nature of attack.

In hydrocarbon reservoirs large quantities of hydrogen sulfide ($H_2S$) are often encountered, especially when drilling deep wells. Hydrogen sulfide is known to induce and/or accelerate the rate of cracking of high strength steels in acidic, aqueous environments due to the migration of atomic hydrogen into the metal lattice and subsequent recombination to hydrogen modules. This type of metal deterioration is called sulfide stress-cracking (SSC) and is typical for steels above certain yield strength. Generally the higher the yield strength, the more susceptible the steel will be to SSC.

Naturally sulfide stress-cracking is extremely important in oil and gas production. Drilling operations are faced with a requirement for high-strength steel tubulars, which should generally not come in contact with sour reservoir fluids, but will potentially be exposed to high $H_2S$ concentrations when influxes of reservoir fluids are taken. Casing and tubing materials for wells expected to produce sour fluids are selected based on the principles and recommendations of the NACE MR0175 standard. The selection process is based on the

drilling mud type, the $H_2S$ partial pressure, the system pressure and the gas to oil ratio in the system.

Since presence of a "sour" environment depends on the $H_2S$ partial pressure, the trend to deeper and higher-pressure wells leads to even small concentrations of $H_2S$ in the reservoir gas triggering this threshold level. At the same time, the requirement to access deeper reservoirs triggers a necessity of utilizing high-strength drill pipe while at the same time assessing and controlling the risks stemming from potentially exposing these high-strength steels to sour wellbore environments. Naturally there is considerable economic interest to estimate the need of equipment exchange and/or define accurate limits for the use of drill pipe equipment in such environments.

## *State of the Art*

Kick detection and killing methods have changed very little over the years. The traditional way to detect kicks is to monitor the drilling mud balance and the change in pit volume. Flow measurements are often done indirectly by multiplying the number of pump strokes with the pumps volumetric displacement. This approach is rather inaccurate and has the disadvantage that kicks are detected rather late and small kicks may even remain undetected. Once a kick is detected, corrective action is taken to regain control over the well. The well is shut in and a kick killing procedure is launched. The driller has to make decisions under intense stress. Mistakes in the design of the killing strategy can lead to formation damage or loss of the well. Due to the slow kick detection method a considerable amount of gas has already entered the wellbore and needs to be safely circulated out of the wellbore.

Although a considerable amount of work has been done in well control, little attention has been given to the issue of multiphase flow mechanisms during a gas-kick. Experimental investigations at flow loops such as Schlumberger Cambridge Research Center have shown that during a simulated kick, the incoming gas rises in a complex way and does not occupy the entire cross section of the annular channel.

Numerous kick simulators have the capability to model various kick sizes and intensities for any given geometry. These simulators are extremely useful in predicting pressure profiles during the kick removal circulation. By doing so many kick simulators model the kick as a single bubble migrating upward as a single slug. Any mixing between the formation fluid and the drilling mud is neglected. These simulators are good in predicting the pressure profiles during well control operations but lack the description of multiphase flow phenomena. Such phenomena include the description of the movement of each individual phase, the evolution and deformation of the phase interface, and phase exchange processes such as the dissolution of gas in the liquid and associated corrosion risks.

# *Experimental Investigations*

Extensive physical experiments simulating gas-kicks, both academic and by the oil and gas industry, have been conducted using flow loops and test apparatus. Among these only a few will be mentioned in this chapter based on their relevance to the subject of this work.

## Test Rigs

During the 1980's and 1990's several full scale gas-kick experiments have been performed by Rogaland Research Institute (RRI), nowadays known as ***IRIS***, in a 2020 m long and 63 degrees inclined research well at ***ULLRIGG***. Ullrigg is a full size offshore-style triple rig, located onshore at Ullandhaug in Stavanger, Norway. The site contains 7 different test wells and was founded 1982 by Shell for research purposes. The gas-kick experiments were carried out with air/water-based mud as well as nitrogen/oil-based mud. The gas was injected into the well at a controlled rate through a coiled tubing at the bit. Experiment parameters like mud density, gas concentration, gas type, mud flow rate, injection depth, and mud type were varied. The active pit volume, standpipe pressure and return mud flow rate were logged during the experiments. The main focus of the research project laid on improvement of safety during drilling by data analysis and development of new kick detection methods. The tests were conducted to gain a better understanding of the kick process and provided important implications regarding kick detection and well control, see Rommetveit et al. (1989) and Hovland (1992).

## Research Flow Loops

Compared to experiments conducted at test rigs, experimental setups at research flow loops mostly located at Universities and or national research centers generally provide a higher grade of information due to the intensive measurement infrastructure. However these research flow loops are limited in size and applicable pressure conditions.

Intensive research was done at the ***Schlumberger Cambridge Research (SCR)*** focusing on two phase flow characteristics. The multiphase flow loop test facility built in 1985 at SCR offers a straight flow length of almost 12 m with a 9.5 m section permitting visual evaluation of the flows. The piping is mounted on a 15 m long table which can be pivoted, enabling tests to be carried out in all orientations from horizontal to vertical. The facility is designed to operate at pressures up to 10 bars. Johnson et al. (1991, 1993) preformed tests on gas migration velocities in this realistic drilling geometry with rheological accurate drilling fluids in inclined and vertical. The majority of the tests were made with a polymer mud analogue which permitted visual observations of the flow field. Their results showed that the gas rises faster than previously believed and that kicks will rise faster in a viscous drilling mud than in water. This is due to a change in the flow pattern causing the formation of large slug-type bubbles. Gas rise velocity and bubble size is independent of void fraction. They also reported significant differences between the effect of deviation on gas migration characteristics in pipe and annular flows.

Of certain interest is the transient two-phase flow test facility ***TOPFLOW*** located at the Helmholtz-Zentrum Dresden-Rossendorf (HZDR). The facility was designed to investigate steady-state and transient two-phase flows at realistic operational parameters. Numerous two-phase flow experiments are planned and executed in close collaboration with the Computational Fluid Dynamics (CFD) community for the evaluation of multiphase flow models. The testing facilities are highly instrumented and equipped with wire-mesh sensors which make them ideally suited for the purpose of model development and CFD code validation. CFD grade experiments as conducted at HZDR are usually very rare.

***SINTEF*** multiphase laboratory facilities located in Trondheim, Norway: These laboratories are especially designed to gain knowledge about the link between chemistry and fluid mechanics. SINTEF operates several multiphase flow loops of different scales to provide flow assurance related research for the petroleum industry. It is the world's largest flow laboratory and is financed by industry as well as public contracts and the research council of Norway. The development of the OLGA multiphase pipe flow simulator was continued and experimentally verified in this institution.

$H_2S$ related corrosion is a topic of great concern but poses difficulties to be studied in the laboratory due to the hazardous nature of $H_2S$. Especially for the case of sour gas entering a wellbore at pressures of 20 MPa and more it is impossible to carry out similar experimental investigations on a flow-loop. Both the high absolute pressure needed and the aggressive nature of hydrogen sulfide prohibits such investigations. The ***Institute for Corrosion and Multiphase Technology*** at the University of Ohio is probably the only institution who owns a hydrogen sulfide multiphase testing facility. The environmentally isolated corrosion flow loop allows investigations of the erosion-corrosion process in sour gas environments. Gas mixtures of methane, nitrogen, and/or carbon dioxide are mixed with flowing liquid mixtures of water and/or oil producing flow regimes of stratified flow, slug flow, or annular flow in the multiphase environment. Three separate test sections for corrosion monitoring where various types of corrosion-monitoring equipment can be installed are available. The flow loop can be operated at system temperatures ranging from 40°C to 90°C and pressures from atmospheric to 70 bars. The system allows investigating the influence of various concentrations of hydrogen sulfide gas on corrosion rate in a controlled multiphase environment.

# *Industry Standards*

The information gathered by the oil and gas production industry on the handling of $H_2S$-containing process streams is summarized in several standards for material requirements (MR standards) and test methods (TM standards). These standards are published by the worldwide corrosion authority NACE (National Association of Corrosion Engineers).

Among them is the NACE MR0175 or ISO 15156, which gives requirements and recommendations for the selection and qualification of carbon and low-alloy steels, corrosion-resistant alloys, and other alloys for service in equipment used in oil and natural gas production and natural gas treatment plants in H2S-containing environments, whose failure could pose a risk to the health and safety of the public and personnel or to the equipment

itself. The standard delineates the partial pressures and conditions under which sulfide stress-cracking can be expected and sets forth a list of materials suitable for handling sour gases and aqueous streams.

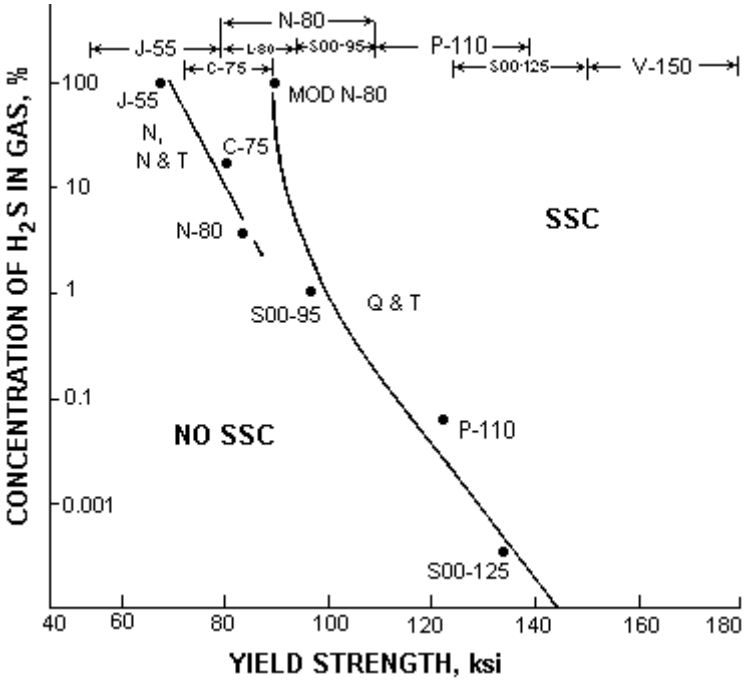


**Figure 1: Effect of H2S on Sulfide Stress Cracking, NACE**

Another important standard is MR0103-2012, which defines material requirements for resistance to sulfide stress cracking (SSC) in sour refinery process environments. One of the types of material damage that can occur as a result of hydrogen charging is sulfide stress cracking (SSC) of hard weldments and microstructures, which is addressed by this standard. This standard is intended to be utilized by refineries, equipment manufacturers, engineering contractors, and construction contractors.

# *Outline of the Thesis*

Subject of this thesis is to investigate the ability of a Computational Fluid Dynamics (CFD) based approach to simulate the distribution of influx gas in the drilling fluid during kick situations. Special focus is put on the bottom-hole inlet region of a vertical well, with the aim of obtaining a highly resolved phase distribution. The modeling approach has to be able to describe the unsteady motion of a compressible gas phase, taking into account turbulence as well as non-Newtonian rheology and no a priori assumptions regarding flow patterns are allowed. The outcome of this investigation shall provide a basis for a subsequent modeling effort covering the chemical reaction kinetics with respect to $H_2S$ influxes in high-pH drilling fluid environments. This thesis builds a basis for a sound understanding of the complex two-phase flow morphology and associated mechanisms, which is needed to establish an adequate model for corrosion risk assessment.

This thesis begins with an introduction to two-phase flow and its characteristics. In chapter 2 typical flow patterns in two-phase flow in vertical pipes are described. The commonly known concept of flow pattern maps is illustrated and its advantages and disadvantages are discussed. Chapter 3 deals with multiphase flow modeling approaches. The basic definition of the governing flow equations for single phase flow is given. It is explained how a fluid-mechanical problem can be analyzed based on dimensionless numbers. Next the concept of dimensional analysis is elucidated and a selection of dimensionless groups defining the problem at hand is suggested. After this an overview of two-phase flow modeling approaches according to their complexity is provided. Beginning with 1-d mechanistic models up to multiphase flow modeling approaches in Computational Fluid Dynamics. The issue of corrosion in drilling engineering is summarized and discussed in chapter 4. The actual modeling approach and model setup for the numerical simulation of gas-kick scenarios is described in chapter 5. Results and discussion of the conducted simulation cases is given in chapter 6. Finally project conclusions and recommendations for future work are provided in the last chapter.

# 2. Two-Phase Flow Morphology

Single-phase flow can be classified according to the external geometry of the flow channel as well whether the flow is laminar or turbulent. In contrast multiphase flow is classified according to the internal phase distributions or morphology of the flow. In general multiphase flow is defined as the concurrent or countercurrent movement of two or more immiscible phases, which can be solid, liquid or gas. Each phase can consist of several chemical components.

In this work only two-phase flows of gas and liquid are considered. The associated physical phenomena are especially complex, since they combine the characteristics of a deformable interface and the compressibility of one of the phases. Gas-liquid flows play an important role in many industrial processes and can cover a wide spectrum of different scales. However any two-phase flow is characterized by a moving boundary between the phases. Geometry, fluid properties and boundary conditions effect the geometric distribution of the phases within the flow and hence the interfacial area available for mass, momentum or energy exchange between the phases. Moreover, the flow within each phase will clearly depend on that geometric distribution. This illustrates the complicated two-way coupling between the flow in each of the phases and the geometry of the flow. The complexity of this two-way coupling presents a major challenge in the study of two-phase flows.

## *Phase Distribution & Flow Patterns*

The most difficult thing in multiphase flow simulation is the prediction of the phase distribution and phase interface. The phase interface is the boundary between bulk regions of two fluids. The interface is a region where physical quantities vary continuously but it's extend is only of a few molecules. Therefore it is a practical concept to consider a so-called "functional interface" with a zero thickness and a jump in physical properties across it. The detection and tracking of the phase interface in multiphase flow can only be accomplished by the means of Computational Fluid Dynamics. Nevertheless this poses a challenging modeling task and is naturally very computationally intensive and still quite limited. It may be possible at some time in the future to compute the Navier-Stokes equations for each of the phases and to resolve every detail of a multiphase flow but with current capabilities we are still far from this.

Before appropriate computational power was available researches introduced flow pattern maps for the qualitative description and classification of phase distribution in their models. When observing gas-liquid flow in a given channel the distribution of the phase interface can be of any arbitrary form. But researchers soon noticed that these forms can be summarized into a few types of interfacial distribution and used for classification of multiphase flow. Thereby a particular type of geometric phase distribution is termed flow. Detailed discussions of these patterns are given by Hewitt (1982), Whalley (1987) and Dukler and Taitel (1986). The macroscopic behavior of the flow like pressure drop, wall heat exchanges or mechanical

interaction with structures is strongly correlated to the flow pattern and can vary from one pattern to another. Almost all multiphase flow models are based on the concept of flow patterns. This is of great ease for modeling but also introduces the disadvantage of discontinuities between the individual flow pattern types.

It is necessary to define flow patterns independently for vertical and horizontal channel orientation. In vertical pipes, two-phase flow can be classified into four flow patterns:

- Bubble flow
- Slug flow
- Churn flow
- Annular flow

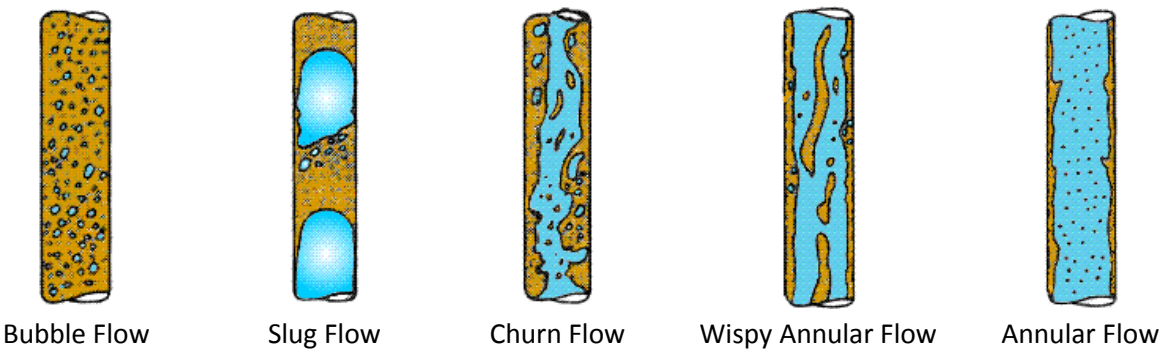


**Figure 2: Flow Patterns in Vertical Flow (G.F. Hewitt)**

The flow pattern depends on the fluid properties, the size of the conduit and the flow rates of each of the phases. The flow pattern can also depend on the configuration of the inlet. It can take some distance for the flow pattern to fully develop and the flow pattern can change with distance. This is certainly true for a well-bore, where the change in pressure affects the gas density and consequently alters the gas flow rate. For fixed flow conditions and fluid properties, the flow rates are the independent variables that can be correlated to a certain flow pattern.

## Bubble Flow

Initially when gas is introduced into a liquid, bubbles are generated. The size of bubbles detaching from the bubble source depends on the geometrical properties of the inlet (e.g. diameter of holes) as well as on the gas and liquid properties and the gas flow rate. The bubble size is typically much smaller than the diameter of the tube. Bubble flow is observed at low superficial gas velocities. In this case gas is the dispersed phase. One of the most important features of dispersed flows is that mass, momentum and energy transfer between the phases are carried out from each bubble to the surrounding continuous phase. Therefore, the mechanisms of mass, momentum and energy transfer from a single bubble basically control the interaction between phases. The most important interaction term is the drag

force acting on the bubble. According to the magnitude of interactions between the bubbles and the surrounding fluid as well as between the bubbles, bubble flow can be sub-classified in ideally-separated bubble flow, interacting bubble flow, churn turbulent bubble flow, and clustered bubble flow, shown in Figure 3. With increasing gas flow rate the bubbles start to interact more strongly initiating a transition from bubble flow to slug or churn flow.

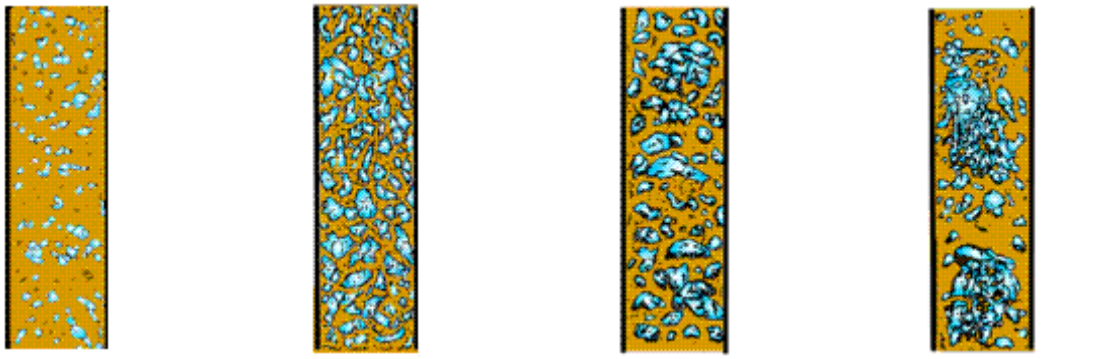


**Figure 3: Bubble Flow Regimes, taken from Thermopedia (2006)**

## Slug Flow & Churn Flow

These types of intermittent flows are characterized by a highly complex phase interface and a strong unsteady nature. Slug flow typically can be initiated by a number of mechanisms. For example, hydrodynamic slugs are formed by waves growing at the phase interface. Typical for the slug flow pattern is the occurrence of large axi-symmetric bullet shaped bubbles, also referred to as Taylor bubbles, which occupy almost the entire cross section of the flow channel. Taylor bubbles are separated from one another by slugs of liquid, which may include small bubbles. A thin liquid film is surrounding the Taylor bubbles next to the channel wall. This liquid film may even flow downwards due to gravity, even though the flow direction of the gas is upward. The intermittency of slug flow is characterized by the slug frequency. The slugs cause large pressure and liquid flow rate fluctuations. The pseudo-periodical character of slug flow has attracted so many researchers to study it using various methods including correlations, one-dimension mechanistic methods to multi-dimension exact solution of continuum equations and momentum equations (Mao and Dukler, 1990; Clarke and Issa, 1997; Kawaji et al., 1997 Anglart and Podowski, 2000). Numerous experimental investigations focused on the measurement of slug length and frequency in pipes. These values are important parameters in slug flow models. Various researchers reported so-called stable slug length in dependence on pipe diameter D from their experiments. For horizontal slug flow, Dukler and Hubbard (1975) reported a stable slug length of about 12 – 30 D. For vertical slug flow, Fernandes (1981) found a stable slug length of about 10 – 20 D.

Different to the previously mentioned researchers, Caetano et al. (1992) investigated Taylor bubbles in upward flow through a vertical annulus. There experiments showed that the Taylor bubble in annuli exhibits neither a spherical cap nor a complete symmetry around the axial

coordinate, as it normally does in circular pipe. Caetano mentions that the deformations are caused by the existence of the axial inner pipe inserted across the bubble. Furthermore they observed a stronger bubble distortion in concentric annuli compared to eccentric annuli and in both cases a preferred channel through the rising bubble where the liquid flows backwards. Rising velocity of the bubble in the annulus is larger than the predicted rising velocity in a circular pipe with a diameter equal to the outer diameter of the annulus.

In vertical or nearly vertical pipes churn flow is showing up at the transition from slug to annular flow. Churn flow shows highly irregular phase interfaces, strong intermittency, and intense mixing. Fluid is travelling up and down in an oscillatory fashion but with a net upward flow. This flow instability is caused by shear force and gravity force acting in opposing direction on the liquid film of the Taylor bubbles. For small-diameter tubes the oscillations may not occur and a smoother transition between the slug flow and annular flow may be observed.

Both flow patterns, slug and churn flow, appear in a wide range of applications and are very common in wellbores. Intermittent flow patterns are generally flow situations to be avoided in corrosive environments, due to the destructive impact the mass of the slugs has on protective scales.

## Annular Flow

With increasing gas flow rate the flow pattern is changing from churn flow to annular flow. In annular flow, the liquid coats the walls. The flow pattern is characterized by a phase interface separating a thin liquid film from the gas flow in the core region. The shear force exerted by the high velocity gas on the liquid film becomes dominant over the gravity force acting on the liquid. The liquid is expelled from the center and left to flow as a thin film on the wall. The gas flows as a continuous phase up the center of the pipe, with some liquid droplets entrained. The interface between the phases is not smooth but instead consists of a multitude of waves induced by the high velocity gas flow. The waves may vary in amplitude and wavelength and have a dominate influence on mass and heat transfer.

Experimental studies of interfacial structures in vertical upward annular flow as done for instance by Hewitt et al. (1964), show that ripples i.e. waves of low amplitude are always present but there are also large amplitude waves. Due to the breakup of the large amplitude waves, part of the liquid phase is entrained as droplets in the gas core. Mass, momentum, and energy transfers are strongly affected by entrainment of the droplets. Hewitt and Hall-Taylor (1972) state that for any given gas and liquid flow rate combination, geometry and physical properties, the fraction entrained is arbitrarily variable and can be altered by changes in the conditions upstream of the point under consideration. The fraction entrained is strongly dependent on position within the channel and on the method of phase introduction. By the means of photographs they illustrated that heavy entrainment occurs in the region of the main disturbance waves. The wave acts as a pump by picking up liquid from the film and ejecting droplets to the gas core. Hall-Taylor et al. (1963) have developed a flow map showing the different regions of interfacial structures observed in air-water flow.

For very low gas rates the phase interface remains smooth. With increasing gas rate small ripples arise which quickly turn into two-dimensional waves. When the gas flux is increased further the waves break up into characteristic three-dimensional squalls. Eventually roll waves form on the surface. On further increasing the gas flow rate, the liquid is torn apart and becomes dispersed in the gas phase.

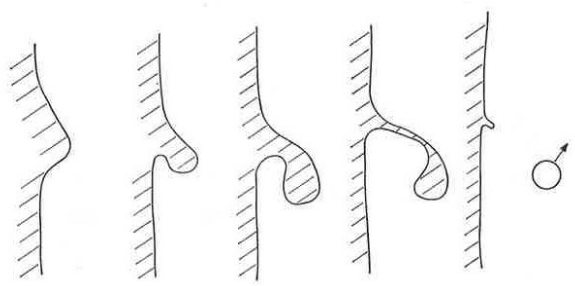

**Figure 4: Breakdown of Disturbance Wave (Hewitt and Hall-Taylor 1972)**

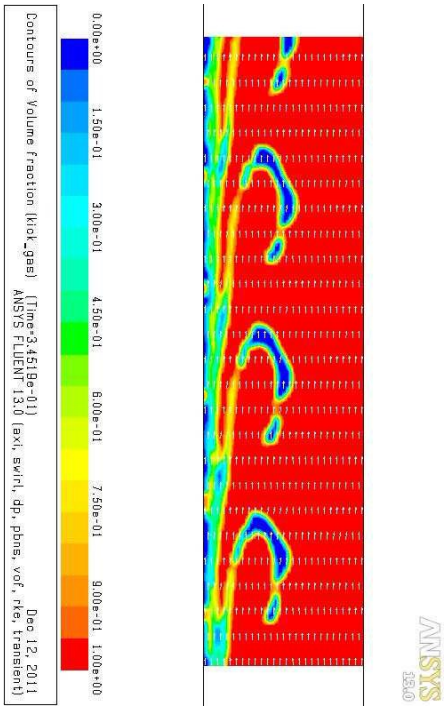


**Figure 5: CFD Simulation of Wave Breakup**

Annular flow is a stable flow pattern. Its distinct separation of phases provides a good basis for analytical studies. This flow pattern has received the most attention, both analytically and experimentally, because of its practical importance and the relative ease with which analytical treatment may be applied.

## Wispy Annular Flow

Wispy annular flow was first identified by Bennett et al. (1965). It is characterized by the nature of the entrained phase. Wispy annular flow is similar to annular flow with the difference that the liquid entrained in the gas core is flowing in large agglomerates. Droplet coalescence in the gas core leads to the formation of large lumps or agglomerates. Bennett et al. (1965) also reported that there is a significant amount of gas entrained in the liquid wall film. Wispy annular flow is typical for high mass velocity flows of both phases.

# *Flow Pattern Maps*

When dealing with two-phase flows it is a common practice two categorize the flow based on a flow pattern map and consequently apply different models to each flow pattern. A flow pattern map is a 2-dimensional diagram that displays flow patterns and their boundaries in terms of particular system parameters. Lines in the flow pattern map illustrate the boundaries between the various flow patterns. Although in reality there are no distinct boundaries between flow patterns but rather transition zones. Similar to the transition from laminar to turbulent flow in single phase flow a certain flow pattern becomes unstable when it approaches the boundary and the growth of the instabilities causes transition to another flow pattern.

Flow pattern maps can be categorized into two groups: empirical flow pattern maps and mechanistic flow pattern maps. Empirical flow pattern maps are based on a large number of experimental data and usually limited by experimental parameters such as fluid properties, tube diameter, and mass flux. The results from the empirical observations are then illustrated in a graph or flow pattern map using appropriate pairs of parameters to represent the multidimensional parameter space in two dimensions.

The difficulty lies in the definition of parameters that distinctly identify a flow pattern. Generally, flow patterns are observed by visual inspection. But the use of completely visual observations for determining flow patterns has the disadvantage of being subjective. There is a wide variety of flow pattern maps and a large number of different parameters have been used to present the data. Conventional parameters used are the superficial velocities of the phases. Superficial velocity is defined by considering a single phase and assuming it occupies the entire flow channel cross-sectional area. Superficial velocity is obtained by dividing the volumetric flow rate by the channel cross-sectional area. Other common macroscopic flow parameters used in flow pattern maps are component flow rates or dimensionless numbers. The flow rates used may be volume fluxes, mass fluxes, momentum fluxes, or other similar quantities depending on the author. Apart from that there are also other means like the analysis of the spectral content of the unsteady pressure fluctuations, or fluctuations in the volume fraction which can be helpful for the identification of flow patterns. Jones and Zuber (1974) demonstrated that the probability density function (PDF) of the fluctuations in void fraction may be used as an objective and quantitative flow pattern discriminator for the three dominant flow patterns of bubbly, slug, and annular flow. The shapes of the probability density functions of void fraction obtained by an x-ray void measurement system are shown in Figure 6.

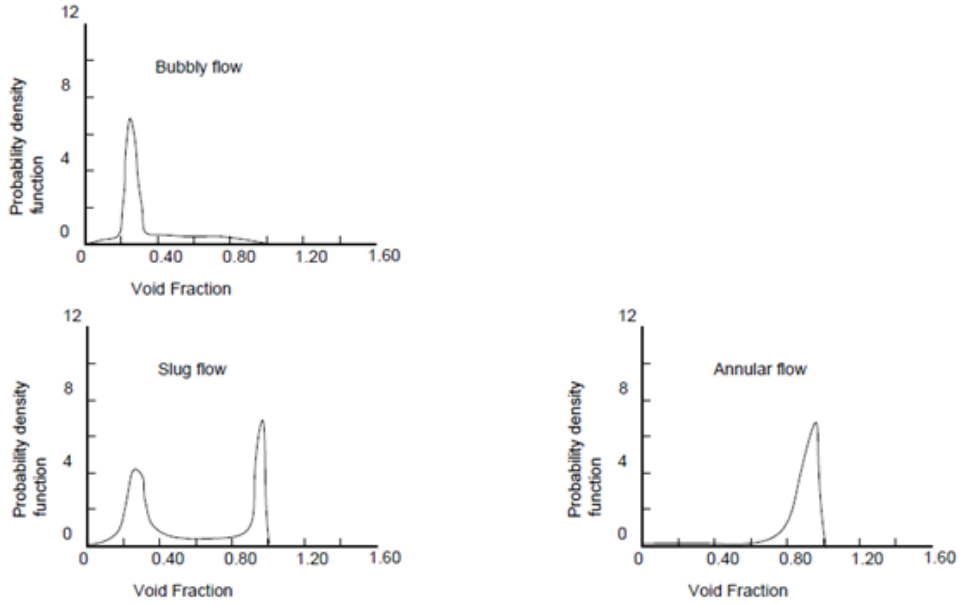


**Figure 6: X-ray Absorption Probability Density Functions of Void Fraction (Jones and Zuber 1975)**

Hubbard and Dukler (1966) showed that the analysis of the frequency of pressure drop fluctuations might be used to distinguish between flow patterns for air–water flow. They found that all of the spectral distributions were seen to fall into three regimes: separated flow, intermittent flow, and dispersed flow as shown in Figure 7.

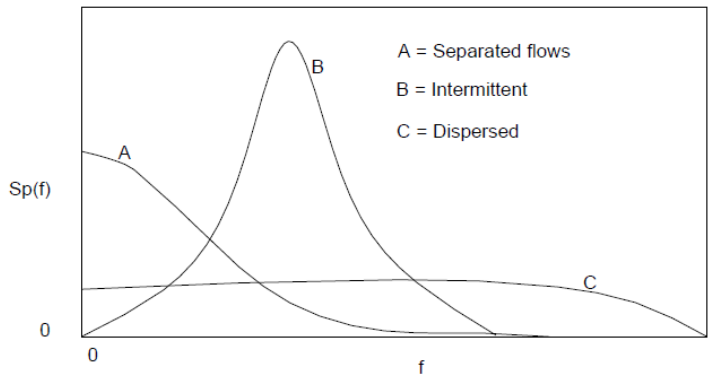


**Figure 7: Power Spectral Density of Wall Pressure Fluctuations (Hubbard and Dukler 1966)**

## Flow Pattern Maps for Pipes

Probably the earliest flow pattern map was published by Baker (1954). The map is shown in Figure 8 and is valid for horizontal flow in tubes. Baker was the first researcher to acknowledge the importance of flow patterns for the calculation of pressure drop, heat and mass transfer in tubes. The Baker map works well for water/air and oil/gas mixtures in horizontal tubes with small diameters, not bigger than 50 mm according to Whalley (1987). The axes are defined in terms of $G_g/\lambda$ and $G_L/\psi$, where

$$G_g = mass\ flux\ of\ gas = \frac{gas\ mass\ flow\ rate}{cross - sectional\ area}$$

$$\lambda = \sqrt{\frac{\varrho_g \varrho_L}{\varrho_{air}\varrho_{water}}}$$

$$G_L = mass\ flux\ of\ liquid = \frac{liquid\ mass\ flow\ rate}{cross - sectional\ area}$$

$$\psi = \frac{\sigma_{water}}{\sigma}\left(\frac{\mu_L}{\mu_{water}}\left[\frac{\varrho_{water}}{\varrho_L}\right]^2\right)^{1/3}$$

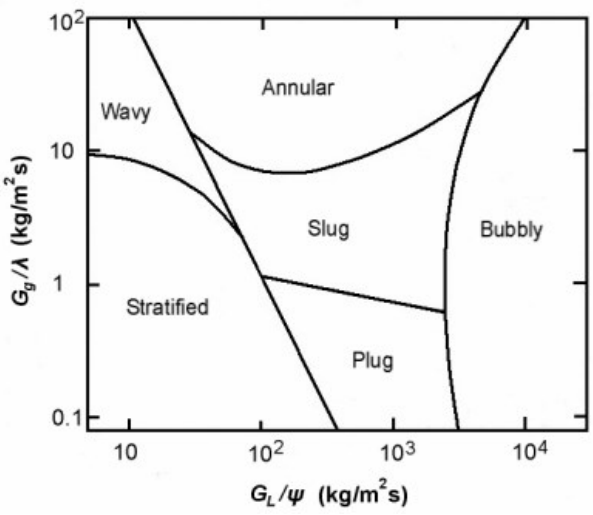


**Figure 8: Baker Flow Pattern Map for Horizontal Flow in Pipes (Baker 1954)**

Tailtel and Dukler (1976) proposed a complex flow pattern map for horizontal flow in tubes based on a combination of their analytical investigations and the use of empirical parameters. The map consists of three graphs and is shown in Figure 9. The parameters used are the Martinelli parameter X, the gas Froude number Fr, and the parameters K and T.

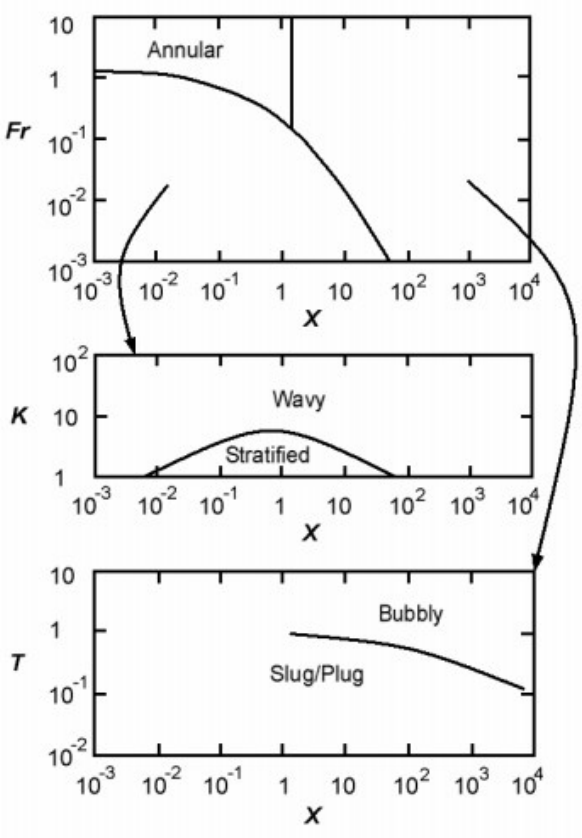


$$X = \left[\frac{(dp/dz)_L}{(dp/dz)_g}\right]^{1/2}$$

$$Fr = \frac{G_g}{\left[\varrho_g(\varrho_L - \varrho_g)dg\right]^{1/2}}$$

$$K = Fr\left[\frac{G_L d}{\mu_L}\right]^{\frac{1}{2}}$$

$$T = \left[|(dp/dz)_L|/g(\varrho_L - \varrho_g)\right]^{1/2}$$

**Figure 9: Two-phase Flow Pattern Map for Horizontal Flow in Tubes (Taitel and Dukler 1976)**

The frictional pressure gradients (dp/dz) needed to compute the parameters, are either defined for the liquid or the gas flowing alone in the tube of diameter d. To use the map one first determines the Martinelli parameter and the gas-phase Froude number. Looking up the coordinates in the first graph provides information, if an annular flow regime is present. In case the coordinates fall into the other regions one determines the next parameter K, and proceeds to the next graph and so on. A detailed explanation of this map can be found in Whalley (1987).

The flow pattern map of Griffith and Wallis (1961) shown in Figure 10 provides a general guide of flow patterns in vertical flow. Several flow patterns are grouped together, and only three flow pattern groups are differentiated. It uses dimensionless ratios for the representation of the flow patterns. $Q_g$ and $Q_l$ are the volumetric flowrates of the gas and liquid phases respectively. A is the cross sectional area and $d_0$ is the equivalent diameter. The vertical axis indicates how much space is occupied by the gas phase and the horizontal axis indicates the kinetic energy of the total flow.

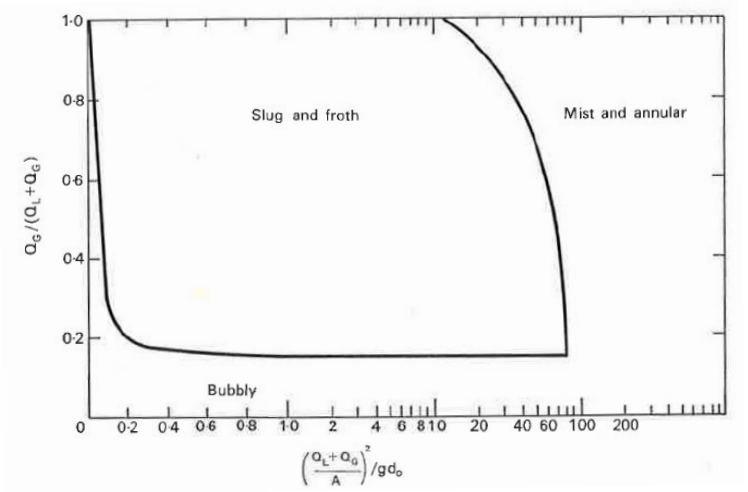


**Figure 10: Flow Pattern Map of Griffith and Wallis (1961)**

For 2-phase flow in vertical tubes the flow pattern maps of Fair (1960) and Hewitt and Roberts (1969) are still among the most widely quoted maps. Figure 11 shows the flow pattern map of Fair (1960), it is based on the overall mass velocity on the vertical axis and a parameter combining the information on vapor quality x, viscosity and density ratio of gas and liquid on the horizontal axis.

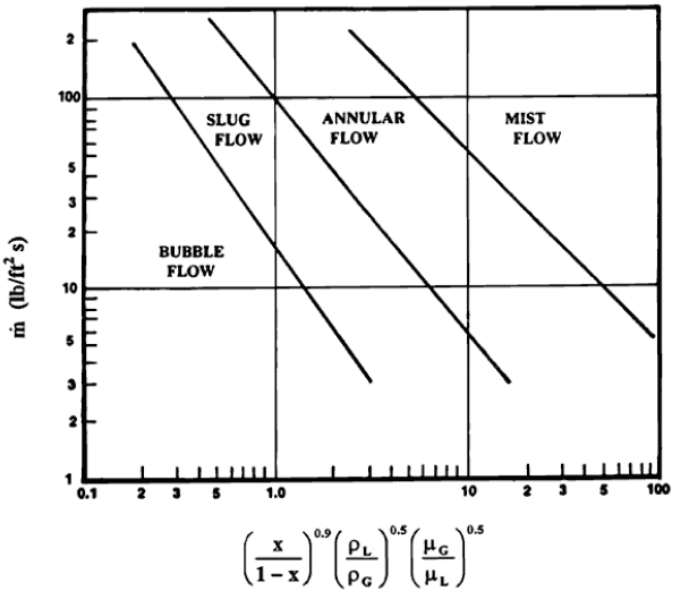


**Figure 11: Two-phase Flow Pattern Map for Vertical Tubes, Fair (1960)**

The flow pattern map introduced by Hewitt and Roberts in 1969 is shown in Figure 12. This is an empirical flow pattern map describing the flow patterns for co-current upward flow in a vertical pipe. Hewitt and Roberts correlated both air/water data at atmospheric pressure and steam/water flow at high pressure. The map is based on the gas and liquid superficial momentum flux rather than volumetric or mass fluxes, and is valid for a wide range of flow rates.

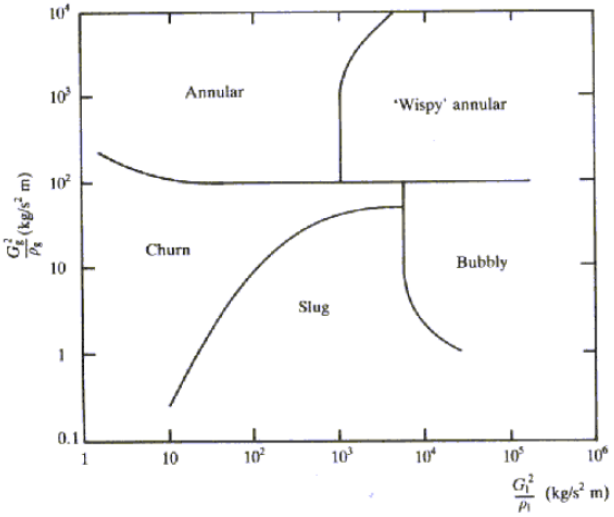


**Figure 12: Hewitt and Roberts Flow Pattern Map for Vertical Upward Flow in a Pipe (Whalley, 1987)**

In contrast to empirical flow pattern maps mechanistic flow pattern maps are based on fundamental considerations and identification of dominant forces found through examination of various flow transition phenomena. These types of maps cover a wider range of experimental conditions than the empirical ones due to having incorporated system parameters. Taitel et al. (1980) presented an alternative to the experimental methods of obtaining flow pattern maps. They considered the conditions necessary for the existence of each of the flow patterns and postulated mechanisms by which the transitions between the various flow patterns might occur. The widely applied models by Taitel et al. (1980), Jayanti and Hewitt (1992) and Barnea (1986) describe the bubble to-slug, slug-to-churn and churn-to-annular flow transitions. Jayanti and Hewitt (1992) improved the modeling of the flooding mechanism given by McQuillan and Whalley (1985) which is dominating the transition from slug to churn flow. At the onset of churn flow a sharp increase in pressure gradient can be observed, this was investigated and reported by Owen (1986). The differentiation of flow patterns based on his results is illustrated in Figure 13.

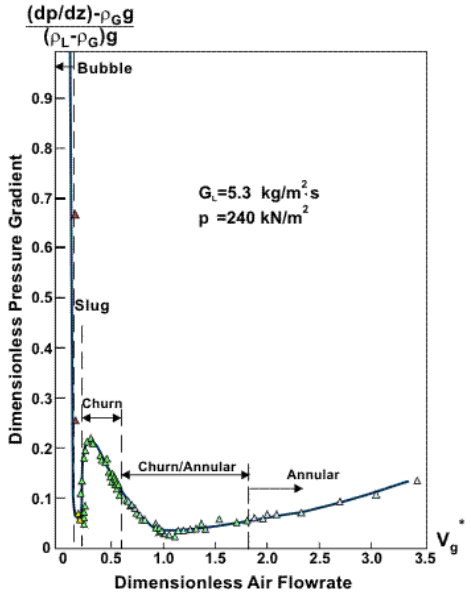


**Figure 13: Pressure Gradient Data of Fully Developed Air-water Flow in a Vertical Tube, Owen (1986)**

Barnea (1987) mentions a unified model for flow pattern transitions for the whole range of pipe inclinations. His work especially focused on the transition from annular to intermittent flows. According to literature the most widely recommended flow pattern maps for vertical tubes are those of Barnea et al. (1987), Fair (1960), Hewitt and Robertson (1969), and Chen et al. (2006).

## Flow Patterns in Annular Geometries

In the literature only few studies can be found on flow patterns in annular flow geometries. One of them is the work done by Caetano et al. (1992), who conducted experimental and theoretical studies on gas-liquid flow through an annulus. Their studies covered vertical upward flow in both concentric and fully eccentric annuli. Air-water and air-kerosene mixtures were used as flowing fluids. Their analysis revealed that application of the hydraulic diameter concept as a characteristic dimension for annuli configurations is not always adequate, especially for small Reynolds number flows. When studying Taylor bubble rise velocity they observed bubble velocity to rise at a faster velocity as the pipe diameter ratio increases. The shape of the Taylor bubbles in the annuli configuration showed no spherical cap or rotational symmetry as it does in pipes. The presence of the inner pipe causes a deformation of the Taylor bubbles as if it is cutting through the bubble. Additionally there appears a channel through the torus bubble body where the fluid is flowing backwards.

The work of Caetano presents flow pattern definitions and experimental flow pattern maps for annuli configurations, based on a modification of Taitel et al. (1980) model for flow pattern transitions in pipe flow. Figure 14 and Figure 15 show the flow patterns occurring in concentric and eccentric annuli. The same flow patterns can be found as in pipe flow, however with substantially different characteristics.

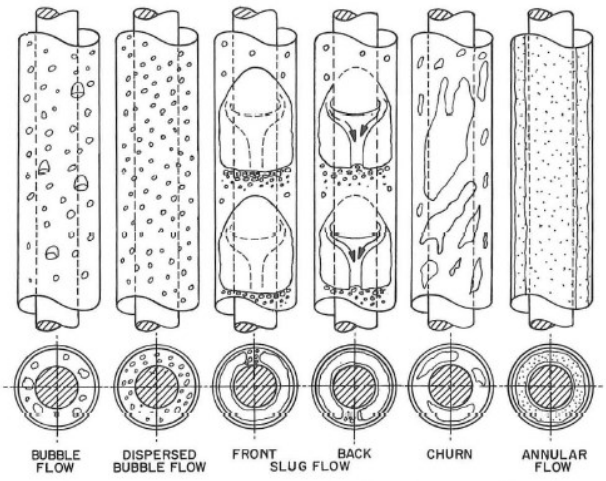


**Figure 14: Flow Pattern in Upward Vertical Flow Through a Concentric Annulus, taken from Caetano et al. (1992)**

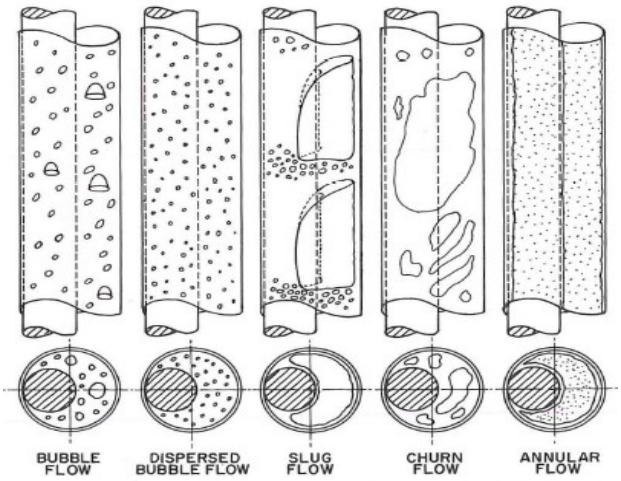


**Figure 15: Flow Pattern in Upward Vertical Flow Through a Fully Eccentric Annulus, taken from Caetano et al. (1992)**

Figure 16 shows a flow pattern map based on the studies of Caetano et al. (1992).

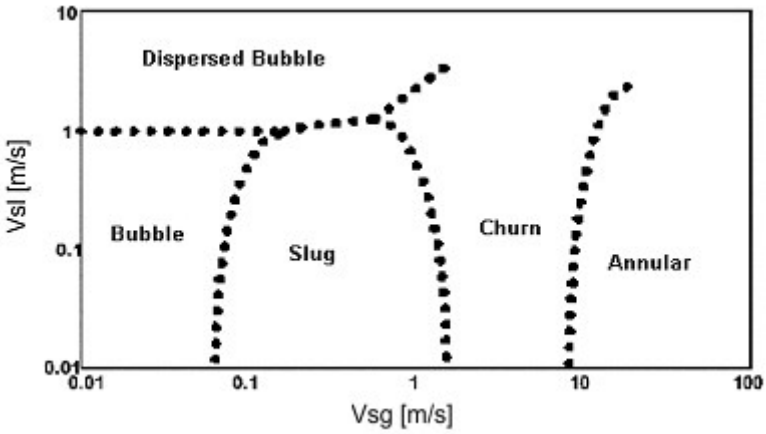


**Figure 16: Flow Pattern Map for Upward Two-phase Flow in Annulus after Caetano et al. (1992)**

## Conclusion on Flow Pattern Maps

Flow pattern maps and transition criteria are developed from experiments and carried out for steady-state, fully developed flows. Taitel et al. (1980) discussed the various flow pattern map parameters available, and argued that the various flow pattern transitions cannot all be represented by any given coordinate pair. The flow pattern depends on multiple dimensions/parameters containing the physical properties of the phases as well as the geometric configuration of the flow domain. Another basic issue regarding flow pattern maps is that they are often dimensional and therefore apply only to a specific two-phase flow setup. Some flow pattern maps attempt to take account of channel geometry and fluid physical properties by suitable adaptation of the parameters which are plotted. A number of investigators (for example Baker 1954, Schicht 1969, Weisman and Kang 1981) have attempted to find generalized coordinates that would allow the map to cover different fluids and pipes of different sizes. Brennen (2005) pointed out that such generalizations are only of limited value because several transitions are represented in most flow pattern maps and the corresponding instabilities are governed by different sets of fluid properties. For example, one transition might occur at a critical Weber number, whereas another boundary may be characterized by a particular Reynolds number. Macroscopic parameters like superficial velocities and flow rates of the phases alone are often not sufficient to characterize the flow pattern because they are missing essential information. Even the assumption that there exists a unique flow pattern for given fluids with given flow rates is not correct. Hewitt and Hall-Taylor (1972) found out that one of the most important variables in determining the flow pattern is the manner in which the phases are introduced into the channel. Similarly, Brennen (2005) showed that even very simple models of multiphase flow can lead to conjugate states. Naturally there could be several possible flow patterns at certain flow conditions only depending on the initial condition i.e. how the multiphase flow was initiated. This fact is often completely ignored. A certain flow pattern is in fact a function of multiple parameters and can therefore only be coarsely described in 2-dimensional flow pattern map.

In general flow patterns depend on:

- Gas and liquid fluid properties (i.e. density, viscosity, etc.)
- Operational parameters (i.e. pressure, temperature, flow rates and direction, inclination angle, etc.)
- Flow channel geometry (i.e. cross sectional area, diameter, annular clearance, eccentricity, etc.)
- Inlet condition (i.e. geometric inlet configuration, inlet boundary condition)

As a consequence there exists no universal, dimensionless flow pattern map that incorporates the full parametric dependence of the flow pattern on the fluid characteristics, boundaries and initial conditions. One has to be aware, that the concept of flow patterns is merely qualitative and subjective.

# 3. Two-Phase Flow Modeling

Basically one can investigate and model two-phase flow experimentally and/or theoretically. In petroleum engineering the most common task in modeling two-phase flow in pipe or annular geometries is the identification of a flow-pattern map. The identification of flow patterns has historically been used to assess the success of drilling and production, since the morphology of the flow determines physical phenomena like mass and heat exchange, mechanical wear and pressure drop. Regarding the two-phase flow situation of a gas-kick the ability to set up an experimental model is very limited and costly. Due to the hazardous nature of $H_2S$ and high pressure conditions needed to reproduce bottom-hole conditions, large-scale experiments can hardly be found in literature. It is more common to conduct sour gas experiments in an autoclave or other small volume test apparatus to gain information for the characterization of reactions and by-products in the corrosion process. However such an approach lacks the mechanical impact of the flow pattern on the corrosion process. Especially the slug flow pattern is assumed to cause an increase in corrosion rate, due to the removal of protective scales by the flow fluctuations. So as a consequence of the extreme dimensions and pressure conditions this flow problem demands for a reliable theoretical or computational model instead.

The mathematical description and its physical model for numerical computation can be done on different levels of sophistication according to the degree of information needed and the means available. For the mathematical and physical description of two-phase flow one may consider the flow field to be composed by single-phase regions with moving boundaries in between. The difficulties in modeling two-phase flow arise from the unsteady nature of this boundary and its influence on the flow field. Additionally processes like heat and mass transfer at the phase interface increase the set of equations that need to be solved. Modelling the detailed distribution of the interfaces in time and space for any particular flow is clearly impossible. Instead simplifications according to the degree of information needed are required.

The goal of this work is to investigate and analyze gas-liquid flow in great detail. To achieve this, computational modeling appears to be the most appropriate choice. The next sections will give a general overview on the governing forces and modeling approaches in two-phase flow.

# *Navier-Stokes Equations*

The fundamental continuum mechanics equations to describe the motion of fluids are the Navier-Stokes equations. These equations are a set of equations that contain the conservation laws for mass, momentum and energy for a single phase.

Looking at single phase flow we know that any movement of a fluid is caused by forces acting on the fluid element. Basically these forces can be grouped into three categories according to their proportionality to dimensions in space, i.e. volume forces, surface forces, and line forces.

**Table 1: Forces acting on a fluid element**

| **Volume Forces** | **Surface Forces** | **Line Forces** |
|---|---|---|
| Gravity force<br>Inertia force<br>Buoyancy force | Pressure force<br>Viscous force | Surface tension force |

Regarding the fluid as a continuum and applying Newton's second law of motion combined with the assumption that the stress state in the fluid is made up by a pressure term and a viscous term, one derives the equation of motion for a fluid element:

$$\rho \frac{d\mathrm{v}}{dt} = \nabla \cdot \sigma + F$$

where σ is the stress tensor, and F accounts for body forces present.

This equation basically states the conservation of momentum, i.e. the sum of all forces acting on a fluid element is equal to its temporal change in momentum. The change in flow, acceleration or deceleration of the fluid element is dependent upon the force exerted on it and is proportional to its mass. This is the property of conservation of momentum and is simply Newton's second law.

The time-derivative of the fluid velocity is defined as:

$$\frac{d\mathrm{v}}{dt} = \frac{\partial \mathrm{v}}{\partial t} + \mathrm{v} \cdot \nabla \mathrm{v}$$

The stress tensor can be split up into two terms, the pressure p times the identity matrix I and the deviatoric stress tensor T.

$$\sigma_{ij} = \begin{pmatrix} \sigma_{xx} & \tau_{xy} & \tau_{xz} \\ \tau_{yx} & \sigma_{yy} & \tau_{yz} \\ \tau_{yz} & \tau_{zy} & \sigma_{zz} \end{pmatrix} = -\begin{pmatrix} p & 0 & 0 \\ 0 & p & 0 \\ 0 & 0 & p \end{pmatrix} + \begin{pmatrix} \sigma_{xx}+p & \tau_{xy} & \tau_{xz} \\ \tau_{yx} & \sigma_{yy}+p & \tau_{yz} \\ \tau_{yz} & \tau_{zy} & \sigma_{zz}+p \end{pmatrix} = -p\mathrm{I} + \mathrm{T}$$

Updating the equation of motion gives the following general form:

$$\rho \frac{d\mathrm{v}}{dt} = -\nabla p + \nabla \mathrm{T} + F$$

This equation is still needs information about the unknown stress tensor T. A constitutive law is needed describing the viscous stress state in the fluid. This constitutive law describes the viscous behavior or rheology of the fluid. In case of Newtonian fluids, there is a linear relationship between applied stress and resulting strain, so fluid viscosity is a constant, applying this relationship leads to:

$$\mathrm{T}_{ij} = \mu \left( \frac{\partial u_i}{\partial x_j} + \frac{\partial u_j}{\partial x_i} \right) + \delta_{ij} \lambda \nabla \cdot \mathrm{v}$$

were $\delta_{ij}$ is the Kronecker delta, μ and λ are proportionality constants associated with the assumption that stress depends on strain linearly, μ is called the first coefficient of viscosity and λ is the second coefficient of viscosity. The value of λ, which produces a viscous effect associated with volume change, is very difficult to determine, the most common approximation is $\lambda \approx -\frac{2}{3}\mu$.

Substitution of $\mathrm{T}_{ij}$ yields the equation of motion for a Newtonian fluid:

$$\rho \left( \frac{\partial \mathrm{v}}{\partial t} + \mathrm{v} \cdot \nabla \mathrm{v} \right) = -\nabla p + \nabla \cdot \left( \mu (\nabla \mathrm{v} + (\nabla \mathrm{v})^T) - \frac{2}{3} \mu (\nabla \cdot \mathrm{v}) \mathrm{I} \right) + \rho g$$

with gravity applied as external force. If one wants to account for the surface tension force at the phase interface in two-phase flow, then exact knowledge about the phase interface is needed. The treatment of the phase interface will be discussed in a later chapter.

The equation of motion can also be expressed in the following terms:

$$Inertial\ forces = pressure\ forces + viscous\ forces + external\ forces$$

Additionally the continuity principle imposes that mass is conserved unless it passes out of the domain. The conservation of mass, without any sources or sinks, is defined as:

$$\frac{\partial \rho}{\partial t} + \nabla \cdot \rho \mathrm{v} = 0$$

Compressible flow additionally requires an equation of state and the conservation of energy formulation. The ideals gas law is often used as an equation of state, but basically the relationship to be used depends on the fluid and the operating conditions.

Conservation of energy is defined as:

$$\rho \frac{dh}{dt} = \frac{dp}{dt} + \nabla \cdot (k \nabla T) + \Phi$$

where h is the enthalpy, k is a heat conduction coefficient, $T$ is the temperature, and Φ is a function representing the dissipation of energy due to viscous effects.

This set of three equations is termed the Navier-Stokes equations, which build the heart of fluid flow modeling. Once the velocity field is calculated, other quantities of interest, such as pressure or temperature, may be found. For certain flow situation simplifications can be made allowing an analytical solution of the set of equations. Nevertheless the full Navier-Stokes equations can only be solved numerically. The Navier-Stokes equations can describe the motion of every phase in every detail, i.e. in every drop or bubble and surrounding fluid when resolving the whole range of spatial and temporal scales. But the computer power required to do this, which is called a direct numerical simulation, is far beyond present capability for most of the flows that are commonly experienced.

The Navier-Stokes equations can be applied to each phase up to an interface but not across it. Special treatment is needed at the interface to account for the sharp changes in variables and to specify the exchange of mass, momentum and energy between the phases. A multitude of different approaches have been put forward to cover the wide spectrum of multiphase flow of different scales. These approaches basically involve the solution of the Navier-Stokes equations combined with additional flow specific models and assumptions. When one or both of the phases becomes turbulent the computational challenge can become enormous. Therefore, simplifications are essential in realistic models of most multiphase flows. Reasonable simplifications of the governing equations can only be based on a clear understanding of the flow and investigation of the dominant forces and mechanisms. Traditionally an engineer starts the characterization of the flow under investigation by the means of dimensionless numbers.

# *Dimensionless Numbers*

When looking at the forces in multiphase flow (Table 1) and their magnitude, the governing forces are pressure force, inertia force, gravity force, buoyancy force, viscous force and surface tension force. Naturally, all these forces are covered in the Navier-Stokes equations. When formulating the forces individually and putting them into relation, non-dimensional groups can be derived. These groups are referred to as dimensionless numbers in fluid mechanics. With these numbers flow problems can be categorized and more important dominant forces are identified. For many decades this approach was used to introduce simplifications in flow modeling. Before setting up a computational model, it is still good engineering practice to analyse the flow problem by assessing its dominant forces and their key basic relations. This provides the basis for a sound modeling approach and is often forgotten, as computational modeling tools and computational power become more and more easily available. This section summarizes the definition and importance of dimensionless numbers in fluid mechanics relevant to multiphase flow.

Based on the six fundamental forces in fluid mechanics the following five independent dimensionless groups can be derived. A detailed explanation and the corresponding equations are given subsequently.

**Table 2: Dimensionless Groups in Fluid Mechanics**

| | | |
|---|---|---|
| **Re** | **Reynolds number** | $\frac{interia\ force}{viscous\ force}$ |
| **Eu** | **Euler number** | $\frac{pressure\ force}{inertia\ force}$ |
| **Fr** | **Foude number** | $\frac{interia\ force}{force\ of\ gravity}$ |
| **We** | **Weber number** | $\frac{interia\ force}{surface\ tension\ force}$ |
| **Eo** | **Eötvös number** | $\frac{buoancy\ force}{surface\ tension\ force}$ |

The first three of them are well known from single phase flow, but do also play an important role in the characterization of multiphase flow. More dimensionless numbers apart from the ones listed in Table 2 can be found in literature. But basically they can be derived by rearranging the five fundamental groups. For instance Archimedes number (Ar), Capillary number (Ca), inverse viscosity number ($N_f$), Morton number (Mo), Ohnesorge number (Oh), and Suratman number (Su) can be derived by combining two or more dimensionless numbers as follows:

$$Ar = \sqrt{\frac{1}{Mo}} = Ri \cdot Re^2, \qquad Ca = \frac{Fr}{\sqrt[4]{MoEo}} = \frac{We}{Re}, \qquad N_f = \sqrt[4]{\frac{Eo^3}{Mo}},$$

$$Mo = \frac{EoWe^2}{Re^4} \quad , \qquad Oh = \frac{\sqrt{We}}{Re} \quad , \qquad Su = \frac{Re^2}{We}$$

The most popular dimensionless number in fluid dynamics is probably the ***Reynolds number***. It represents the ***ratio between inertia and viscous forces,*** or in other words relates the fluids momentum to its viscosity. It is primarily used to characterize single phase flow as either turbulent or laminar.

$$Re = \frac{F_I}{F_V} = \frac{\rho L U}{\mu}$$

ρ fluid density
L characteristic length, i.e. hydraulic radius
U mean velocity of the fluid
μ dynamic fluid viscosity

Multiphase flows are usually considered turbulent, although laminar flow can occur when the flow channel or conduit is aligned horizontal. In inclined flows buoyancy is affecting the flow causing the lighter phase to accelerate and generate turbulences. Naturally in multiphase flow the concept of the Reynolds number needs to be revised. One approach is to use mixture quantities to compute a mixture Reynolds number. This approach might be valid in case of dispersed flow with low slip velocity. But in case of segregated flow, where fluid velocities differ considerably, this approach is not sufficient to describe the flow situation. In this case the Reynolds number should rather be computed for each phase using the individual phase velocities and properties. However there is no general consensus on what to use for an appropriate definition of Reynolds number for multiphase flow. It is up to the researcher to select a definition that best describes the flow under investigation.

The ***Euler number*** represents the ***ratio between pressure forces and inertia forces***. It relates a local pressure gradient to the kinetic energy of the fluid volume. It is used to characterize losses in the flow and is defined as:

$$Eu = \frac{F_P}{F_I} = \frac{\Delta p}{\rho U^2}$$

Δp pressure gradient

A perfect frictionless flow corresponds to an Euler number of 1.

The ***Froude number*** describes different flow regimes of open channel flow. It is defined as the ***ratio of the flow inertia and gravity***:

$$Fr = \frac{F_I}{F_G} = \sqrt{\frac{\frac{\rho U^2}{2}}{\rho g h}} = \frac{U}{\sqrt{gL}}$$

g acceleration due to gravitation
h hydraulic depth
L characteristic length, i.e. height of the liquid film

The Froude number is of importance whenever there is a fluid flow with a free interface. This is certainly true in separated two-phase flow. For this type of flows the Froude number seems a good correlating parameter. Flows with the same Froude number have similar wave patterns at the phase interface. The denominator represents the speed of a small surface wave relative to the speed of the bulk fluid, called wave celerity. Based on the Froude number open channel flow is classified into three types:

Fr = 1, critical flow
Fr > 1, supercritical flow
Fr < 1, subcritical flow

At critical flow wave celerity equals bulk flow velocity. Any disturbance to the flow will remain stationary. In subcritical flow the bulk flow velocity is slower than the wave velocity and hence flow disturbances are transmitted upstream and downstream. This condition leads to backwater effects. In supercritical flow the bulk flow is faster than the surface wave causing disturbances to be transmitted only downstream. It is only in supercritical flows that hydraulic jumps can occur.

The above definition of the Froude number and of flow classification is only valid for free surface, i.e. flows in horizontal channels with the denser fluid flowing at the bottom. Several extensions of the Froude number exist to cover effects like inclination (pressure potential and gravity potential), fluid rotation, and buoyancy (Densimetric Froude number).

The relevance of the Froude number to characterize gas-liquid flow in pipes can be seen in the work of Taha and Cui (2005). Their work presents a numerical study investigating the motion of a single Taylor bubble. Based on a dimensional analysis the following definition of the Froude number, as the ***ratio between inertia and buoyancy forces,*** is used:

$$Fr_{gas} = \frac{U_{TB}}{\sqrt{gd\dfrac{\rho_l - \rho_g}{\rho_l}}}$$

$U_{TB}$ Taylor bubble velocity
$\rho_g$ gas density
$\rho_l$ liquid density
d pipe diameter

The publication of Taha and Cui (2005) contains a good literature overview on previous work done regarding dimensionless groups to characterize slug flow. Their study of single Taylor bubble movement in stagnant and flowing liquid is a good basis to understand the complicated nature of slug flow.

The ***Weber number*** represents the ***ratio of inertia force to surface tension force***.

$$We = \frac{F_I}{F_S} = \frac{\rho L U^2}{\sigma}$$

$\sigma$ surface tension

Inertia is the driving force causing partial disruption of flow structures and is counteracted by the resistance due to interfacial tension. Increased Weber numbers are associated with a greater tendency for droplet deformation and breakup to occur at higher shear, i.e. with more intense mixing. The Weber number is useful for the determination of stable bubble diameters and bubble distortion tendency under certain flow conditions. When surface tension forces are dominant, the bubble tends to be spherical and when inertial forces are dominant, the bubble tends to have a hemispherical shape.

The ***Eötvös number,*** also called ***Bond number,*** represents the ***relative significance of buoyancy and surface tension***.

$$Eo = Bo = \frac{F_B}{F_S} = \frac{(\rho_l - \rho_g) g d^2}{\sigma}$$

A small Eötvös number indicates a strong influence of surface tension resulting in a rather spherical bubble shape whereas a large Eötvös number results in distorted bubble shapes and increased bubble velocity. The Eötvös number is often used in combination with the Morton number to characterize bubble and droplet shapes.

In multiphase flow, forces like the surface tension force can have a significant effect on the flow morphology and hence need to be considered. Based on the assumption that the inertia and viscous forces in the gas are much smaller than those in the liquid a group of three dimensionless numbers is well suited to cover the relationship of relevant forces. Typical groups of dimensionless numbers so characterize gas-liquid flow that are frequently found in literature are:

- Froude & Morton & Eötvös number
- Froude & Eötvös & $N_f$ number
- Froude & $N_f$ & Archimedes number

An example for the use of the first dimensionless group is shown in Figure 17, representing the correlation of experimental data on the rise of Taylor bubbles obtained by White and Beardmore (1962). Taylor bubbles were observed in vertical tubes rising through several different stagnant fluids. The Morton number shown in the graph represents the fluid properties, the Froude number represents the bubble rising velocity and the Eötvös number illustrates the influence of surface tension. For certain Morton numbers bubbles may not even rise below a critical Eötvös number. There is a region for Eo < 70 where the Froude number i.e. rising velocity is a function of Eötvös number only. At Eo > 200 there is an inertial region where liquid viscosity and surface tension are less important.

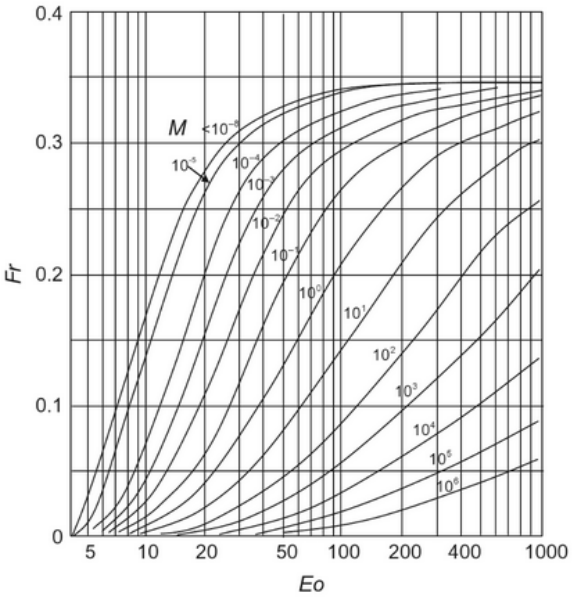


**Figure 17: Correlation of the Rise Velocity of Cylindrical Bubbles (White & Beardmore 1962)**

The ***inverse viscosity*** dimensionless number ***Nf*** represents the influence of liquid viscosity and geometry on phase mixing in slug flow.

$$N_f = \frac{\sqrt{gd^3}}{\nu_l}$$

$\nu_l$ kinematic viscosity of liquid

Guedes de Carvalho (1988) used the inverse viscosity number to classify the wake behind Taylor bubbles. They identified three different patterns, i.e a closed axisymmetric wake for Nf <500, closed unaxisymmetric wake for 500<Nf<1500 and opened wake with recirculatory flow for $N_f$>1500. Their experimental results were simulated by Taha and Cui (2005) and matched favorably as shown in Figure 18.

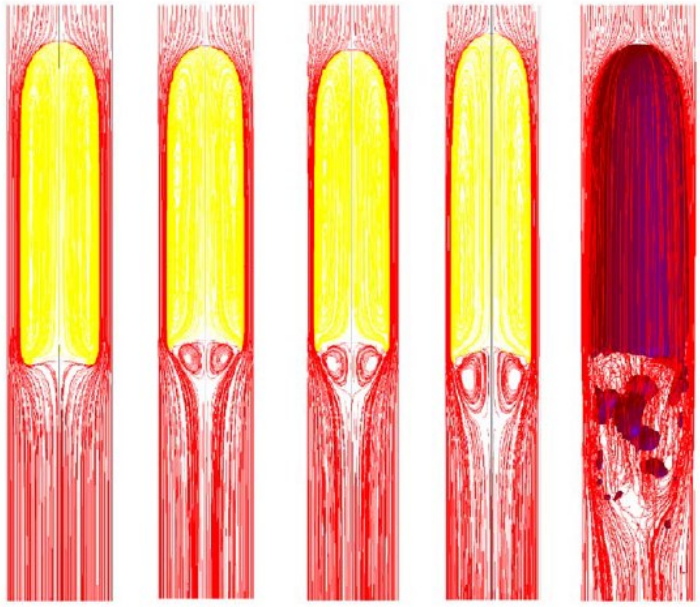

| | | | | | |
|---|---|---|---|---|---|
| 0,066 | 0,064 | 0,064 | 0,063 | 0,064 | **Eo** |
| 0,30 | 0,341 | 0,351 | 0,351 | 0,341 | **Fr** |
| 84 | 176 | 205 | 325 | 1528 | **$N_f$** |

**Figure 18: Wake Flow Pattern at Different Values of $N_f$, taken from Taha and Cui (2005)**

Extending the inverse viscosity number with the fluid densities one derives the ***buoyancy Reynolds number R***, defined as

$$R = \frac{\sqrt{gd^3(\rho_l - \rho_g)\rho_l}}{\mu_l}$$

Viana et al. (2003) gathered extensive experimental data on the rise velocity of Taylor bubbles in stagnant fluids for their universal correlation approach. They used a group of dimensionless velocity, buoyancy Reynolds number, and Eötvös number to characterize the flow. Figure 19 illustrates the shape of the wake behind the Taylor bubble in dependence of dimensionless numbers, R and Eo respectively. With decreasing viscosity the perfect shape of the bubble gets more and more distorted until eventually a highly turbulent region with small bubbles forms in the wake.

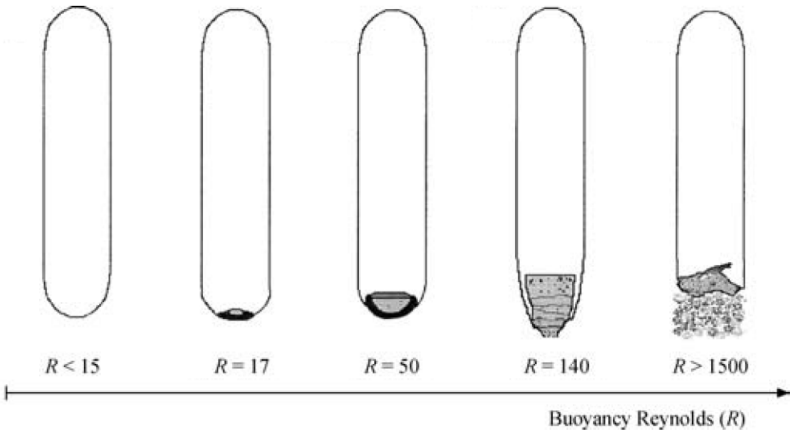


**Figure 19: Taylor Bubble Wake Morphology according to Buoyancy Reynolds Number, taken from Viana et al. (2003)**

The ***Morton number*** is defined as

$$Mo = \frac{F_B F_V^4}{F_I^2 F_S^3} = \frac{g(\rho_l - \rho_g)\mu_l^4}{\rho_l^2 \sigma^3}$$

$\mu_l$ dynamic viscosity of liquid

The ***Morton number*** is used to characterize dispersed two phase flows. It is only dependent on fluid properties and is sometimes referred to as the property group. At atmospheric pressure the density of gas is often neglected in the definition of the number. The Morton number relates viscous forces to surface tension forces. According to the Morton number fluids can be arranged into two groups, those with high Morton numbers (Mo > $10^{-2}$) and those with low Morton numbers (Mo < $10^{-6}$). Water for instance has a Morton number of 1.1e-11. High viscosity drilling fluids typically show high Morton numbers.

***Ohnesorge Number*** relates the ***viscous forces to inertial and surface tension forces***.

$$Oh = \frac{F_V}{\sqrt{F_I F_S}} = \frac{\mu}{\sqrt{\rho \sigma L}}$$

The combination of these three forces into one masks the individual effects of every force. It is used in spray technology to describe bubble and droplet distortion. Larger Ohnesorge numbers indicate a greater effect of the viscosity.

***Suratman number,*** also known as Laplace number, is used for characterization of free surface flows. It is defined as the ratio of surface tension to momentum-transport:

$$Su = \frac{\rho_l d\sigma}{\mu_l^2} = \frac{Re^2}{We}$$

This number depends only on the properties of the liquid and the pipe diameter, and does not depend on the flow rates of the liquid or gas. It is used in some flow pattern maps to account for channel geometry and fluid properties.

***Richardson number*** describes the ***ratio of potential to kinetic energy***.

$$Ri = \frac{E_p}{E_k}$$

There are several variants of the Richardson number. In general it is an essential parameter describing turbulence of sheared stratified flows. The Richardson number indicates the onset of the ***Kelvin Helmholtz instability***. An instability that arises in parallel shear flows, where small-scale perturbations draw kinetic energy from the mean flow. A typical example is the formation, rise, and braking of waves. Another important fluid dynamic phenomenon is the ***Rayleigh-Taylor instability***. This instability describes the distortion of an interface between two fluids of different density which occurs when the lighter fluid is pushing the heavier fluid.

Some other important dimensionless numbers of relevance when dealing with mass transfer in two-phase flow are the Sherwood number and the Schmidt number.

The ***Sherwood number*** is the dimensionless form of the mass transfer coefficient. It is defined as the ratio of

$$Sh = \frac{kL}{D}$$

k mass transfer coefficient
L characteristic length scale
D mass diffusivity

***Schmidt number*** relates the ***diffusivity of momentum to the diffusivity of mass***:

$$Sc = \frac{\nu}{D}$$

$\nu$ kinematic viscosity
D diffusivity

The Schmidt number plays a role in mass transfer. It relates the molecular ability of a fluid to transport momentum to its ability to transport species. The Schmidt number of gases is typically in the order of unity. In liquids where molecules are packed closely together diffusion is much slower but momentum is efficiently transmitted through molecular interactions. Therefore, Schmidt numbers in liquids are typically three orders of magnitude larger than those in gases.

# *Dimensional Analysis*

Although some of the fluid flow relevant forces can be neglected in certain cases, it is a challenging task to determine which one is dominant at specific conditions. The sensible selection of relevant forces can provide great benefits in the subsequent modeling effort. Such simplification of the problem can lead to even analytical solutions of the Navier-Stokes equation; see literature on Hagen-Poiseuille flow or Couette flow as an example.

Dimensional analysis is the mathematical tool to assess the relation of physical quantities without knowing an exact formulation of the problem at hand. This approach has been well applied in fluid dynamics to realize geometrically similar experimental setups or simplified computational models representing a far more complex flow problem at first. Dimensional analysis is the basis for similitude theory. Physicians like Ludwig Prandtl, Theodore von Karman, Johann Nikuradse and many others used this theory at the end of the 19$^{th}$ century to reproduce flows of different length scales in their lab experiments by altering fluid viscosity and density.

The prior task in dimensional analysis is to highlight the dominant forces, their relevant relations and effects in the physical system under investigation. This information is best summarized via dimensionless numbers. There are basically two approaches to identify the relevant dimensionless numbers of a fluid-flow problem, either by applying the Π-Theorem, or by reformulation of the governing equations so that they only contain dimensionless variables.

The first approach will be shortly addressed in the next section. However, it has to be recognized that the dimensional analysis provides answer to what group of parameters affect the problem and not the answer to the problem.

## Π-Theorem

The Buckingham Π-Theory requires no knowledge about the underlying equations. Due to its simplicity this approach may sometimes yield insufficient knowledge, but the method has its usefulness when no governing equations are found. In this technique only the dimensions or the properties of the problem at hand are analyzed.

The basic set of seven dimensions that can describe any physical problem consists of length, mass, time, electric current, temperature, luminous intensity, and quantity of substance. These dimensions can be recombined to create derived dimensions, like for instance velocity, acceleration, density, viscosity and so on. When describing a fluid mechanics problem a reduced set of fundamental dimensions is usually sufficient. The choice of whether to use fundamental dimensions or derived dimensions is not unique it is only a matter of preference. For example, one could use the combination of mass, time, length or instead force, time, length.

The following five out of the seven afore mentioned fundamental dimensions are relevant in the description of multiphase flow including mass transfer:

- Length (L)
- Mass (M)
- Time (θ)
- Temperature (T)
- Quantity of substance (N)

They build the basis to describe all physical phenomena occurring during a gas-kick in a wellbore. The number of basic dimensions a problem has determines the number of the combinations which affect the physical situations. The total number of dimensions, i.e. the sum of fundamental and derived dimensions, a problem has can therefore be reduced because these dimensions are repeating or reoccurring.

The Buckingham method is based on the fact that all equations must be consistent with their units and that they can be divided to create dimensionless equations. The terms in the equations are then dimensionless parameters or also termed Π-Factors. This idea leads to the assumption that these dimensionless parameters can be found without any knowledge of the governing equations.

The analysis starts with the preparation of a list of parameters that are presumed to define the behavior of interest. Considering a gas-kick in a wellbore and its fluid dynamic effect on drill-pipe corrosion, the following list of parameter is assumed to define the flow system:

| | |
|---|---|
| $U_{LS}$ | Superficial mud velocity |
| $U_{GS}$ | Superficial gas velocity |
| $\rho_l$ | Mud density |
| $\rho_g$ | Gas density |
| $\mu_l$ | Mud viscosity |
| $\mu_g$ | Gas viscosity |
| $\sigma$ | Surface tension |
| d | Annular clearance |
| g | gravity |
| $C_{H2S}$ | Concentration of dissolved $H_2S$ |
| k | Mass transfer coefficient |
| D | Molecular diffusion coefficient |
| S | Gas solubility |

This list is valid for fully developed flow and restricted to a limited section of the wellbore. No entrance effects are considered. This is expressed by the independence on time and an absence of a z-coordinate. Gas phase density is based on bottom-hole pressure and assumed to stay constant in this section.

The corrosive threat caused by the flow can be expressed as the following functional dependence:

$$corrosive\ threat = \mathrm{f}\left\{U_{LS}, U_{GS}, \rho_l, \rho_g, \mu_l, \mu_g, \sigma, d, g, C_{H2S}, k, D, S\right\}$$

The term corrosive threat is used because the actual corrosive attack depends on far more variables than only the presence of dissolved $H_2S$ and the flow conditions. The corrosive attack itself is not subject of this investigation. Corrosive threat is used as an arbitrary expression and is neither given an exact definition nor units. It is a theoretical contribution of the 2-phase flow to the corrosion of the drill-pipe.

The main factors of contribution are the concentration of dissolved $H_2S$ and flow induced erosion. The fluid-mechanical erosion of the drill pipe, protective coatings, and corrosive products is caused by the flow field next to the pipe wall. This flow field exerts pressure and viscous forces on the drill pipe surface. At a local scale of observation these forces are dependent upon the drill pipe roughness, the fluid density and the local instantaneous fluid velocity only. However for the dimensional analysis the flow field cannot be described at such a high temporal and spatial resolution, instead macroscopic flow variables with respect to time and space are needed. For instance the fluid mechanical damage of the drill pipe can more abstractly be explained by transient pressure fluctuations as a function of two-phase flow pattern and an assumption of single phase flow adjacent to the drill pipe surface exerting an abrasive shear stress. Or even coarser by replacing the single phase wall shear stress with the phase kinetic energy based on the superficial fluid velocities. The occurrence of transient pressure fluctuations is dependent on the two-phase flow pattern in the channel. As discussed earlier two-phase flow patterns are a function of multiple flow variables and can probably best described with the aid of dimensionless groups.

The minimum number of independent dimensionless groups i required to describe the fundamental behavior is defined as:

$$i = n - m$$

where n is the number of variables and m is the number of fundamental dimensions.

For the current problem the number of variables is 13 and five fundamental units. Using the Buckingham Pi theorem, this yields 13 – 5 = 8 independent dimensionless parameters.

The selection of a dimensionless group is arbitrary and there are different methods to determine the set of dimensionless groups. Common methods are the method of combination, the algebraic method, and the method of speculative reduction.

The next step is to prepare a matrix of the variable's dimensions. Based on the problem at hand the resulting matrix reads:

| | $U_{LS}$ | $U_{GS}$ | $\rho_l$ | $\rho_g$ | $\mu_l$ | $\mu_g$ | $\sigma$ | d | g | $C_{H2S}$ | k | D | S |
|---|---|---|---|---|---|---|---|---|---|---|---|---|---|
| **L** | 1 | 1 | -3 | -3 | -1 | -1 | 0 | 1 | 1 | -3 | 1 | 2 | -3 |
| **M** | 0 | 0 | 1 | 1 | 1 | 1 | 1 | 0 | 0 | 0 | 0 | 0 | 0 |
| **θ** | -1 | -1 | 0 | 0 | -1 | -1 | -2 | 0 | -2 | 0 | -1 | -1 | 0 |
| **T** | 0 | 0 | 0 | 0 | 0 | 0 | 0 | 0 | 0 | 0 | 0 | 0 | 0 |
| **N** | 0 | 0 | 0 | 0 | 0 | 0 | 0 | 0 | 0 | 1 | 0 | 0 | 1 |

From inspection of the above matrix the following dimensionless groups can be formed:

$$Re_L = \frac{\rho_l U_{LS} d}{\mu_l}, \quad Re_G = \frac{\rho_g U_{GS} d}{\mu_g}, \quad We = \frac{\rho_L d (U_{LS} - U_{GS})^2}{\sigma}$$

$$Mo = \frac{g(\rho_l - \rho_g)\mu_l^4}{\rho_l^2 \sigma^3}, \quad Eo = \frac{(\rho_l - \rho_g) g d^2}{\sigma}, \quad Fr_{gas} = \frac{U_{LS}}{\sqrt{gd\frac{\rho_l - \rho_g}{\rho_l}}}$$

$$Sh = \frac{kd}{D}, \quad Sc = \frac{\nu}{D}, \quad \frac{C_{H2S}}{S}, \quad \frac{\mu_g}{\mu_l}$$

These dimensionless groups seem most appropriate to describe the corrosive threat induced by the flow at an arbitrary section of the wellbore.

Looking at the section where the gas-kick is entering the wellbore (which the actual simulation model is representing) the set of variables changes. Instead of the two superficial velocities, four alternative variables are introduced, namely the entrance area and mass rate for each phase. Based on these variables the kinetic energy rate delivered by each phase into the system can be computed and will be used to introduce a new dimensionless group.

$$\dot{E}_{kin,g} = \dot{m}_g \frac{U_{G,in}^2}{2}$$

$$\dot{E}_{kin,l} = \dot{m}_l \frac{U_{L,in}^2}{2}$$

$$U_{S,mix} = \frac{\left(\frac{\dot{m}_g}{\rho_g} + \frac{\dot{m}_l}{\rho_l}\right)}{A_{annulus}}$$

The updated set of dimensionless groups is defined as

$$Re_{L,in} = \frac{\rho_l U_{L,in} \frac{A_l}{d}}{\mu_l}, \qquad Re_{G,in} = \frac{\rho_g U_{G,in} \frac{A_g}{d}}{\mu_g}, \qquad We = \frac{\rho_L d (U_{L,in} - U_{G,in})^2}{\sigma}$$

$$Mo = \frac{g(\rho_l - \rho_g)\mu_l^4}{\rho_l^2 \sigma^3}, \qquad Eo = \frac{(\rho_l - \rho_g) g d^2}{\sigma}, \qquad Fr_{gas} = \frac{U_{S,mix}}{\sqrt{gd \frac{\rho_l - \rho_g}{\rho_l}}}$$

$$Sh = \frac{kd}{D}, \qquad Sc = \frac{\nu}{D}, \qquad \frac{C_{H2S}}{S}, \qquad \frac{\mu_g}{\mu_l}$$

$$\dot{E}_{kin} \text{ ratio} = \frac{\left|\dot{E}_{kin,l} - \dot{E}_{kin,g}\right|}{\dot{E}_{kin,l} + \dot{E}_{kin,g}}$$

| | |
|---|---|
| $\dot{E}_{kin,g}$ | rate of kinetic energy delivered by gas |
| $\dot{E}_{kin,l}$ | rate of kinetic energy delivered by mud |
| $U_{G,in}$ | gas inflow velocity |
| $U_{L,in}$ | mud inflow velocity |
| $A_g$ | gas inlet area |
| $A_l$ | mud inlet area |
| $\dot{m}_g$ | gas mass flow rate |
| $\dot{m}_l$ | mud mass flow rate |
| $U_{S,mix}$ | superficial mixture velocity |

This set of dimensionless groups is suggested to characterize the two-phase flow of gas-kicks in vertical wellbores. The corresponding values are calculated for all simulation cases presented in this work. The relevance of the dimensionless numbers is discussed based on the selected simulation parameters in the result section of this thesis.

# *Overview on 2-Phase Modeling Approaches*

In 2-phase flow modeling we can distinguish between different degrees of sophistication and different approaches to model the phase interaction. In the following an overview of common modeling methods is given and the approaches are briefly described.

## Mechanistic 1D Models

Mechanistic modeling is a mixture of applying conservation equations, observation and empirical correlations. Mechanistic models are 1D models with the need of closure relations to compensate local flow characteristics, like velocity, wall shear stress, liquid holdup, etc. Apart from the closure relationships usually obtained by empirical correlations, these models have a much wider range of application compared to mere empirical approaches. The major uncertainty of mechanistic models lies in the closure relations. These relations are often obtained from experiments at low pressure and temperature laboratory conditions using alternative fluids and reduced pipe diameters. Upscaling of the experimental results does often fail to represent actual field conditions.

Mechanistic models approximate the physical phenomenon by taking into consideration the most important processes and neglecting other less important effects that can complicate the problem but not add accuracy considerably. For instance, if a flow is dominated by one dimension then the other two dimensions may be neglected. Taitel & Dukler (1976) developed the first mechanistic model for determining flow pattern transitions. With the help of flow pattern transition models the development of comprehensive models began. Comprehensive models can handle different flow patterns and pipe geometries by using different flow models for different flow patterns. Among the most common models to solve two-phase flow problems are the drift-flux model and the two-fluid model. These models need constitutive relationships to solve some of the unknowns. Therefore, the flow pattern needs to be assigned a priori to determine the constitutive relations to be used in the solution.

Almost all mechanistic models are specifically developed to model two-phase flow in pipes; the annular conduit is largely being neglected. Only a limited number of studies can be found that is dealing with the adaption of correlations developed for vertical two-phase pipe flow to the annular geometry. Worth mentioning is the work of Caetano et al. (1992a) who conducted experiments of air-water and air-kerosene flow in annuli configurations. Based on the experimental data Caetano et al. modified the Taitel et al. (1980) model for flow pattern prediction to apply it to annuli flows. Caetano et al. (1992b) present mechanistic models to predict pressure gradient specifically for vertical two phase flow in an annulus. These models cover bubble, dispersed bubble, slug and annular flow patterns. The models are based on two-phase flow physical phenomena and incorporate annulus characteristics such as casing and tubing diameters and degree of eccentricity. Ozar et al. (2008) provide a well-structured overview on experimental investigations and existing models for gas-liquid two-phase flow in vertical annuli.

There are two main categories of mechanistic models used to simulate two-phase flow. The simpler category is the drift-flux model, which considers the flowing mixture as a whole, with slip between individual phases. It requires some assumptions to be made across the various phases and is not as accurate or as flexible as two-fluid model. The two-fluid model considers each flowing phase separately and accounts for the interactions between them.

## *Drift Flux Models*

Drift flux models were first developed by Zuber (1965) and Wallis (1969). The drift-flux technique is an approximate formulation for two-phase flow. Due to its simplicity and applicability to a wide range of two-phase flow problems it is of practical interest and applied in many wellbore simulators.

In the drift flux modeling approach one phase is assumed to be dispersed in the other. The 1-dimensional flow of the mixture of both phases is described by a combined momentum and continuity equation and a continuity equation for the gas phase. The focus of the model lies on the relative motion of the disperse phase rather than on the motion of the individual phases. The relative motion is described by a subset of channel-averaged flow parameters, like for instance the relation of the dominant forces acting on the individual phases. Drift flux models are particularly well suited to flow problems where the relative motion of the fluids is dominated by an external force like gravity. Instead of solving the momentum and energy equations the relative motion can be approximated as a function of gravity, volume fraction and physical fluid properties.

The general expression for the area-averaged drift-flux model is given by

$$U_G = \frac{U_{GS}}{\alpha} = C_0 U + U_d$$

where,

| | |
|---|---|
| $\alpha$ | void fraction |
| $U_G$ | gas velocity |
| $U_{GS}$ | superficial gas velocity |
| $U$ | total superficial velocity |
| $C_0$ | phase distribution parameter |
| $U_d$ | drift velocity |

Various drift flux correlations present procedures to compute the empirical parameters $C_0$ and $U_d$. The phase distribution parameter is due to the non-uniform radial distribution of total volumetric flux and void fraction. Depending on the flow pattern and channel geometry different correlations to compute $C_0$ and $U_d$ can be found in literature. Especially Ishii and Hibiki proposed numerous relationships for different flow patterns.

The drift flux model has widespread application to bubble flow and plug flow but is not particularly suitable to annular flow. In annular flow the liquid phase shows two characteristic velocities, i.e. the liquid film velocity and the liquid drop velocity, a situation the drift flux

model cannot handle. In general the drift flux modeling approach is inadequate to model separated flows due to the strong dependence of the fluid motion to the local pressure and velocity gradients in the phases instead to an external force.

## *2-Fluid Model (1D)*

The 2-fluid model is an advanced modeling approach where each fluid is modeled explicitly allowing the computation of each phase velocity, temperature and pressure. The model was initially developed by Wallis (1969), Drew (1971), and Ishii (1975). A multitude on 2-fluid model approaches can be found in literature. Probably the most accurate formulation of the model is provided by Ishii and Hibiki (2010).

The two-fluid model is based on the mass, momentum and energy conservation equations for each phase, along with corresponding balance equations at phase interfaces. A volume average treatment is used for each phase. To close the model interface transport coefficients are defined and need constitutive relation models for completion. These interface transport coefficients signify the phase interactions at the phase interface and define the terms added to the phase conservation equation. These interface transport coefficients, accounting for momentum and heat transfer, need to be specified. The usual method of modeling pressure differences between the fluids is to assume that the pressure is equal in both phases. Otherwise one needs to introduce a local constitutive relation which accounts for this pressure difference due to dynamic and interfacial effects. The other interface transport coefficients are complicated functions of the fluid velocities and their local properties that require great insight on the two-phase flow morphology. These kinetic models are strong function of the flow pattern. The interfacial transfer terms, contain the interfacial area concentration, which is defined as the total phase interface area per unit mixture volume (Ishii 1975, Ishii and Hibiki 2010), and the void fraction. There are two approaches to define the interface area concentration. The first approach is based on experiments and correlates the interface area concentration with flow patterns. This approach has the disadvantage of numerical instabilities in the overall model due to the jumps at the flow pattern boundaries. A smoother solution is provided by the use of an interfacial area transport equation, which can dynamically model the evolution of interfacial structures across the flow pattern transition boundaries through mechanistic modeling of phase interaction phenomena (Hibiki and Ishii 2000).

## Computational Fluid Dynamics

In recent years, Computational Fluid Dynamics (CFD) has emerged as a powerful tool for both scientists and engineers. With the technological development of numerical models along with advanced computational systems, remarkable progress in multiphase flow modeling has been reached over the past decades. Computational Fluid Dynamics allows the most detailed and accurate modeling of multiphase flow compared with the previous mentioned modeling approaches, but may also be the computationally most expensive approach. It is the tool to most accurately model transient flow phenomena. However multiphase flow modeling with the means of CFD is still not as mature as other simulation branches. There exists a variety of physical modeling approaches for the numerical computation of multiphase flows. In general a CFD modeling approach comprises the application of several models depending on the flow problem under investigation and the degree of information needed. The models and their interaction is illustrated in Figure 20. The basic fluid flow is modeled by the conservation laws for mass, momentum and energy using time-averaged quantities. The small-scale, short-time and random fluctuations of flow quantities are covered by a turbulence model. Depending on the flow morphology different multiphase flow models are available and reaction kinetics can be simulated with an appropriate reaction model. All models are coupled with each other by the exchange of flow quantities.

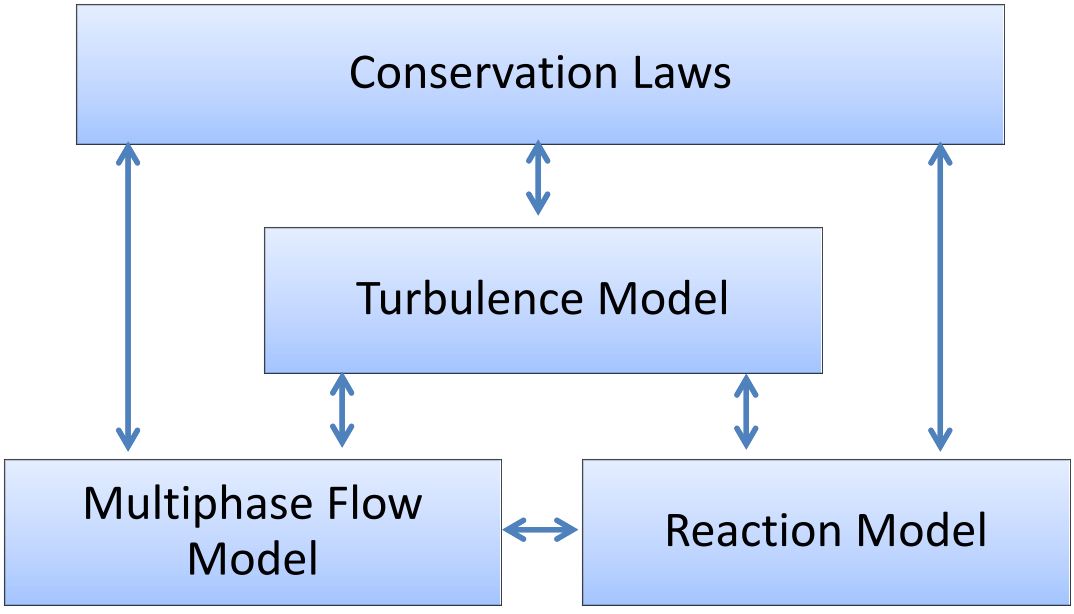


**Figure 20: Model Relationship and Hierarchy**

The largest difficulty in numerical modeling of multiphase flows arises from the fact that the phase interface is moving and that flow quantities like density, viscosity, pressure are discontinuous across the interface. The construction of phase interaction terms represents the core problem in modeling multiphase flows and there exists no universally applicable methodology that is independent of the topology of the flow. Based on the structure of the

gas-liquid interface one distinguishes between segregated, transitional and dispersed two-phase flow, as shown in Figure 21.

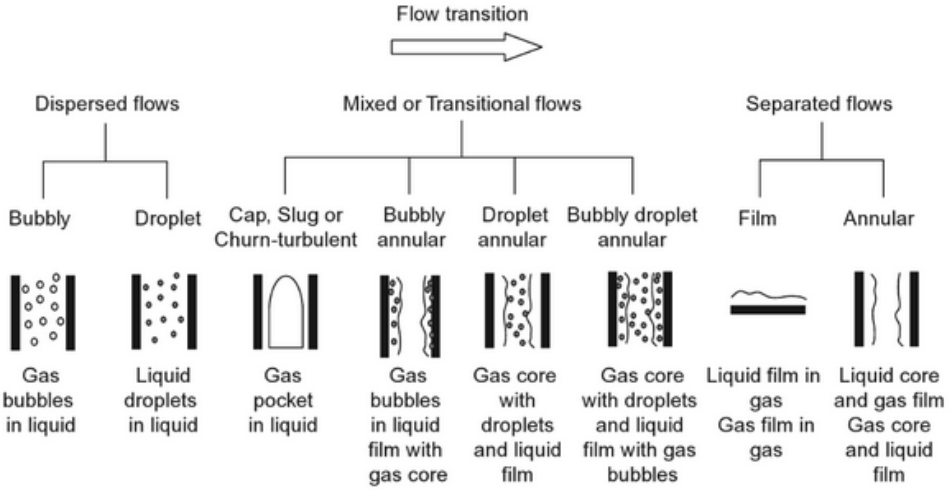


**Figure 21: Classification of Gas-Liquid Flows, Hibiki (2006)**

Different multiphase flow models are available depending on the flow structure. The scale of the interfacial structure and the desired degree of resolution is the dominant factor in multiphase flow model selection. Each multiphase flow model approach involves certain assumptions and hence differs in its strength, limitations and applicability to model a certain flow manifestation. It is the modeler's task to do a proper selection on the physical model and its settings for a specific flow problem under consideration. The modeling decision may be further challenged by the occurrence of a wide size range in interface structures and transitions between them. An overview of the multiphase flow modeling categories is shown in Figure 22.

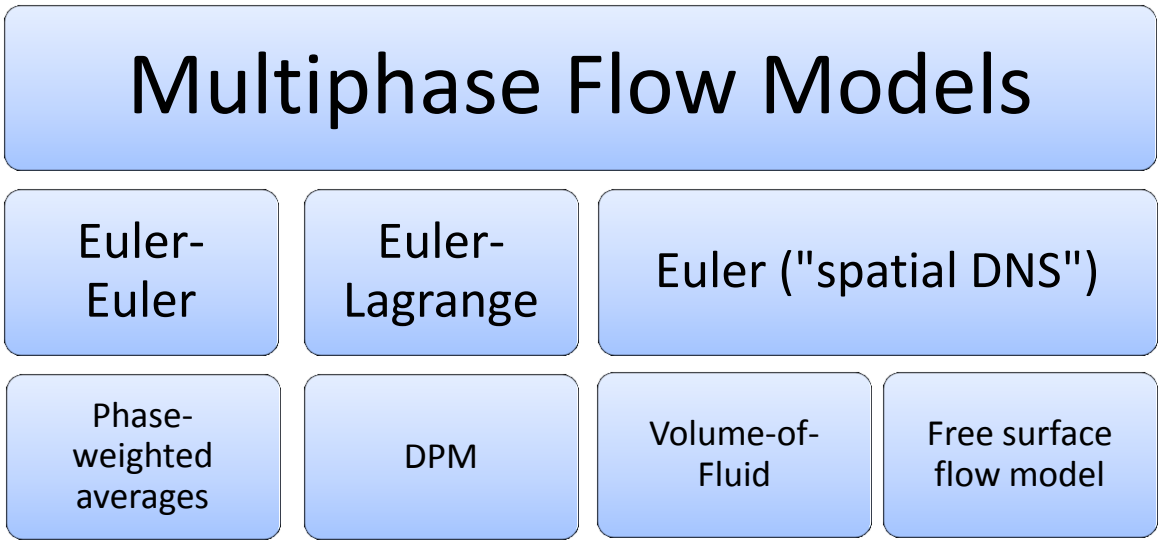


**Figure 22: Multiphase Flow Model Categories, ANSYS (2015)**

In general there are two basic modeling strategies when modeling fluid flow, one is the Lagrangian approach and the other is the Euler approach. In the Lagrangian specification of the flow field one is looking at the fluid motion by following individual fluid parcels moving through space and time. In other words the reference frame used to compute flow variables is moving with the flow. In the Eulerian specification of the flow field the observer's frame of reference is fixed. Fluid motion is observed at specific locations in space, i.e. computational grid, through which the fluid flows as time passes. According to these specification possibilities of the computational reference frame, multiphase flow models use these approaches according to their benefits to compute the flow field of the individual phases. The decision on what basic model to use for the computation of a two-phase flow phenomenon strongly depends on the ability to resolve the gas-liquid interface within the computational mesh.

## *Euler-Euler Model*

In the Euler-Euler approach the flow domain is discretized into control volumes. The flow across the control volume boundaries is observed. Phases are treated as interpenetrating continua with non-equal velocity and temperature. Since the volume of a phase cannot be occupied by the other phases, the concept of phase volume fraction is introduced. These volume fractions are assumed to be continuous functions of space and time and their sum is equal to one. Conservation equations for momentum and continuity are solved for each phase. Balance equations and relations for interface coupling describing interfacial momentum and heat transfer are used to close the equations. The main steps in Euler-Euler modeling are illustrated in Figure 22.

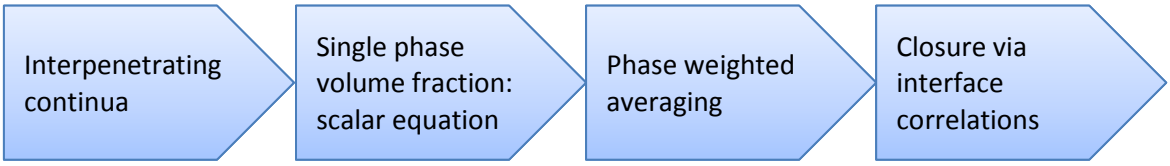


**Figure 23: Euler-Euler Modeling Approach**

There are several variants of the Euler-Euler modeling strategies. For instance the CFD simulator ANSYS Fluent provides the following two approaches:

- the mixture model
- the Eulerian model

The ***mixture model*** is solving the three conservation equations for the mixture, the volume fraction equation for the secondary phase, and computes relative velocities based on an algebraic slip relation. The algebraic slip relation can be specified by the user or taken from the drift flux model approach as mentioned earlier. The mixture model is well suited to model dispersed multiphase flows.

The ***Eulerian model*** is the most complex variant of the Euler-Euler models listed here. It solves the momentum and continuity equations for each phase. Coupling is achieved through the pressure and interphase exchange coefficients. Depending on the type of phases involved the coupling is achieved by different models. The Eulerian model is used to model dispersed multiphase flows like bubble columns, risers, particle suspension, and fluidized beds.

A general drawback of phase weighted averaging is the loss of information on the flow details. Since the phase interface is not resolved, a certain phase volume fraction may correspond to different flow morphologies. This is illustrated by the following two images, showing two different types of flow but both showing an averaged volume fraction of 0.5. As a consequence this approach should only be applied to model dispersed flow regimes.

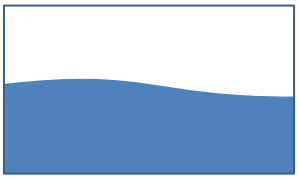

**Figure 24: Segregated Flow with $\alpha = 0.5$**

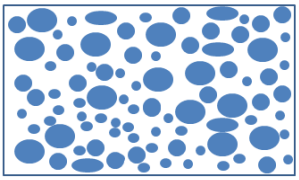

**Figure 25: Dispersed Flow with $\alpha = 0.5$**

In general for an averaged two-fluid approach bubble sizes have to be smaller than the discretized cell size. The approach is thus well suited to describe small-scale dispersed flow like bubbly or droplet flow, where the scale of the interfacial structure is smaller than the computational cell size.

## *Euler Lagrangian Approach*

The Lagrangian discrete phase model (DPM) follows the Euler-Lagrange approach. The fluid phase is treated as a continuum by solving the time-averaged Navier-Stokes equations, while the dispersed phase is solved by tracking a large number of particles, bubbles, or droplets through the calculated flow field. For the particles a Lagrangian approach is used, applying the physical laws directly to each particle. Particle position, velocity are described as a function of time. Particles can interact with the continuous (Euler) phase by exchanging momentum, mass and energy. The main steps in Euler Lagrangian modeling approach are illustrated in Figure 22. General simplifying assumption that are commonly made include

- negligence of particle volume in the continuous phase solver
- spherical particle shape
- flow details in particle vicinity
- representative particle used to model particle group

Depending on the assumptions made the validity of the modeling approach can be limited to a certain volume fraction of the dispersed phase. Usually a dispersed phase volume fraction of less than 10 – 12 % allows particle-particle interactions and the effect of the dispersed phase on the continuous phase to be neglected.

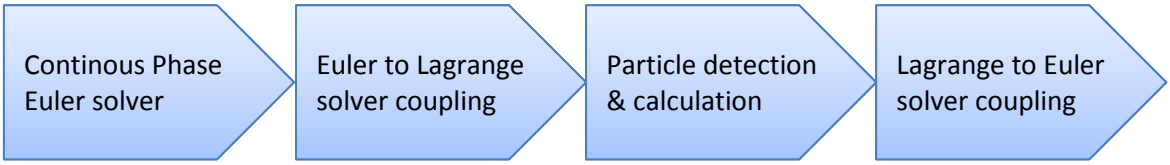


**Figure 26: Euler-Lagrange Modeling Approach**

In general, the Euler Lagrangian modeling approach is appropriate for simulation of sprays, and some particle laden flows, but inappropriate for the modeling of liquid-liquid mixtures, fluidized beds or any application where the volume fraction of the secondary phase is not negligible.

## *Euler Spatial DNS Approach*

All afore mentioned multiphase flow models require a priori knowledge on the flow. Especially in case of dispersed flow, assumptions need to be made regarding the bubble or droplet size of the dispersed phase. In contrast the Euler Spatial Direct Numerical Simulation (DNS) approach aims to describe in detail the deformation and topological evolution of the phase-interface separating the two fluids. Sharp interfaces between immiscible fluids can be modeled using interface tracking methods. The use of interface tracking algorithms minimizes the modeling efforts on the bulk flow substantially. These methods involve a single-fluid formalism, solving a set of conservation equations with variable material properties and surface forces and are more accurate than the mere phase-average model. Mathematically, the interface is treated as a surface of discontinuity. Basically there are two groups of methods available for the computation of the phase interface according to their reference frame:

**Table 3: Interface Tracking Methods**

| **Interface Tracking Methods** | |
|---|---|
| Surface Methods:<br>• Surface-attached moving meshes<br>• Boundary element methods | Volume Methods:<br>• Volume of Fluid Method (VOF)<br>• Level-Set Method |

Volume tracking (Eulerian) methods differ fundamentally from surface-tracking (Euler-Lagrange) methods. The interface is not explicitly defined but instead needs to be reconstructed from a single volume variable (phase fraction) at every time step. Therefore the main issue in volume tracking methods is that the detailed physical features involved cannot be fully resolved due to smearing of the information. To keep the interface numerically sharp and to avoid artificial smearing due to numerical diffusion special numerical methods have been developed. The most established volume based interface tracking methods used for this task are the volume of fluid (VOF) method and the Level-set method.

The ***volume of fluid method*** was initially presented by Hirt and Nichols (1981). Since then it has been continuously developed and improved. The method is based on the idea to model the movement of two immiscible fluids by one fluid with mixture properties. This reduces the modeling effort to the solution of a single set of conservation equations and tracking the phase volume fraction throughout the domain. The fields for all variables and properties are shared by the phases and represent volume-averaged values, based on the local volume fractions. Thus the variables and properties in any cell are either fully representative of a single phase or a mixture of both phases. A scalar quantity f is used to define the ***volume fraction*** $\alpha$ of each phase in a cell. The ***phase indicator*** f represents the fraction of the volume of a mesh cell occupied by a phase. Thus the volume fraction of the phases is defined as

$$\alpha_l = f, \qquad \alpha_g = 1 - f$$

$\alpha_l$ volume fraction of liquid phase
$\alpha_g$ volume fraction of gas phase
f phase indicator

The phase indicator f of a cell is either 1 if the cell is fully occupied with one phase or zero when it is fully occupied with the other phase. Computational cells with a value of 0<f<1 indicate the instantaneous presence of both phases and are consequently cells that contain a phase interface, as illustrated in Figure 27. The volume fractions of both phases sum to unity.

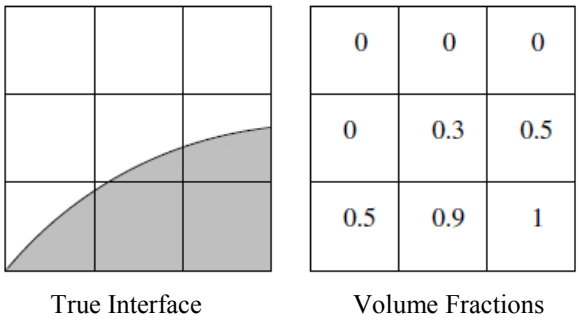


**Figure 27: Volume Fractions on a Discrete Mesh (Pilliod and Puckett 2004)**

The ***mixture properties*** needed for the transport equations are determined by the presence of the phases in each computational cell. For two phase flow the definition is given by

$$\rho_m = \alpha_l \rho_l + (1 - \alpha_l)\rho_g$$

$$\mu_m = \alpha_l \mu_l + (1 - \mu_l)\rho_g$$

$\rho_m$ mixture density
$\mu_m$ mixture viscosity
$\mu_l$ viscosity of liquid phase
$\rho_g$ density of gas phase
$\alpha_l$ volume fraction of liquid phase

Based on the mixture properties a single ***equation of motion*** is solved for the mixture fluid. The resulting mixture velocity is valid for both phases.

$$\rho_m \left(\frac{\partial \mathrm{v}}{\partial t} + \mathrm{v} \cdot \nabla \mathrm{v}\right) = -\nabla p + \nabla \cdot \left(\mu_m (\nabla \mathrm{v} + (\nabla \mathrm{v})^T)\right) + \rho g$$

This equation is dependent on the volume fractions through the material properties only. The volume fractions are propagated through the domain by solving a scalar convection equation defined by

$$\frac{\partial f}{\partial t} + \nabla \cdot f U_m = 0$$

$U_m$ mixture velocity
$f$ phase indicator

The transport equation for the volume fraction is satisfying mass conservation of both phases.

Within the volume of fluid method a ***continuity equation*** based on the volume fraction is defined for each phase. The tracking of the phase interface in case of two phase flow is accomplished by the solution of the volume fraction equation of one phase. The volume fraction of the other phase is computed based on the constraint that the volume fractions of both phases sum to unity.

$$\frac{\partial}{\partial t}(\alpha_l \rho_l) + \nabla \cdot (\alpha_l \rho_l \mathrm{v}) = S_{\alpha_l} + \left(\dot{m}_{gl} - \dot{m}_{lg}\right)$$

$$\alpha_g + \alpha_l = 1$$

$S_{\alpha_l}$ source term
$\dot{m}_{gl}$ mass transfer rate, gas to liquid
$\dot{m}_{gl}$ mass transfer rate, liquid to gas

Using the explicit time discretization leads to

$$\frac{\alpha_l^{n+1}\rho_l^{n+1} - \alpha_l^n \rho_l^n}{\Delta t} V + \sum_f \left(\rho_l U_f^n \alpha_{l,f}^n\right) = \left[S_{\alpha_l} + \left(\dot{m}_{gl} - \dot{m}_{lg}\right)\right] V$$

$n+1$ index of current time step
$n$ index of previous time step
$U_f$ volume flux through cell face
$\alpha_{l,f}$ volume faction value at cell face (computed by interface reconstruction scheme)
$V$ volume of cell

Storing phase volume fractions per cell rather than explicit interface geometry eases the simulation of multiphase flows. However in order to compute the phase fluxes at the cell faces information is need about the interface geometry and orientation. Since the volume fraction has large gradients at the interface the application of a standard difference scheme for spatial discretization would result in numerical smearing and interfaces would lose their definition. Waclawczyk and Koronowicz (2005) showed that most convective differencing schemes applied to the volume fraction convection equation introduce too much numerical diffusion and smear the step profile of the interface over several cells. To avoid this smearing,

the use of higher order or blending differencing schemes like CICSAM (Ubbink 1997) or geometrical reconstruction of the phase interface (Youngs 1982) are suggested. The CICSAM scheme is particularly suitable for fluid pairs with a high viscosity ratio. This is the crucial task to provide accurate advection of the fluid phases (Pilliod and Puckett 2004). The phase fluxes are obtained by these interface reconstruction schemes. Within the CICSAM scheme the computation of convection and diffusion fluxes through the cell faces is based on the following donor-acceptor scheme

$$\phi_f = \phi_d + \beta \nabla \phi_d$$

$\phi_f$ volume fraction value at cell face
$\phi_d$ donor cell volume fraction value
$\beta$ slope limiter value
$\nabla \phi_d$ donor cell volume fraction gradient

The scheme identifies one cell as a donor of an amount of fluid from one phase and neighboring cell as the acceptor of that same amount of fluid. More details on the theory of the compressive interface capturing scheme (CICSAM) can be found in the work of Ubbink (1997).

Finally the ***energy equation*** within the volume of fluid method is defined as

$$\frac{\partial}{\partial t}(\rho_m E) + \nabla \cdot \left(\mathrm{v}(\rho_m E + p)\right) = \nabla \cdot \left(k_{eff} \nabla T\right) + S_h$$

$k_{eff}$ effective thermal conductivity, shared by the phases
$S_h$ source term

Energy E and temperature T are defined as mass averaged variables according to

$$E = \frac{\alpha_l \rho_l E_l + \alpha_g \rho_g E_g}{\alpha_l \rho_l + \alpha_g \rho_g} \qquad T = \frac{\alpha_l \rho_l T_l + \alpha_g \rho_g T_g}{\alpha_l \rho_l + \alpha_g \rho_g}$$

Compared with the Euler-Euler and the Euler-Lagrange approach described earlier, the volume of fluid method and other interface capturing approaches can be thought of as an Euler Spatial Direct Numerical Simulation (DNS) of interface motion (not of turbulence), where no closure assumptions for the interfacial area evolution are needed. A prerequisite for the application of interface capturing methods is that interfacial length scales have to be several times larger than the grid size. Meaning the computational grid needs to be refined to such an extent that most computational cells are occupied by a single fluid and phase interfaces are represented by as few cells as possible. The volume of fluid method has its strength in modeling large-scale interfacial structures, with a grid fine enough to capture the phase interface allowing a detailed resolution of surface phenomena. Interface tracking methods are best suited for these flows as they represent the interface topology rather accurately and are built within a single fluid formalism. Applications of the VOF model include stratified and free-surface flows, as well as steady or transient tracking of any liquid-gas interface.

## *Multi-Phase Flow Simulators*

In this section existing multi-phase flow simulators are listed that are most relevant for the simulation of multi-phase flow in pipelines and wellbores. It is not the intention to give a complete summary of existing simulation tools but to list the most common commercial products and models behind.

Transient simulations of gas-liquid flow in pipelines and wellbores involve elaborate computer codes and require considerable computational efforts. Consequently it has always been desired to simplify the modeling effort but still achieve realistic answers. Several codes have been proposed for this task so far, and supported by the oil and gas industry.

Historically, OLGA is the first of these codes. It is today probably the most well documented and advanced multi-phase transient pipe flow simulator with a global market share of about 90%. OLGA, the name is short for “oil and gas simulator”, was originally developed in the 80s by Statoil (Bendiksen et al. 1987, 1991) and then continued further by SINTEF. The code is capable of modeling a wide range of scenarios by varying fluid properties, pressure, temperature, geometry, trajectory, influx rate, circulation rate, friction, etc. The software is based on a one-dimensional, two-fluid model. For the gas and liquid phases, the model consists of separate conservation equations for both mass and momentum. A single energy conservation equation is used for the liquid and gas phase. Solving the system of conservation equations requires averaging and simplification. OLGA also involves flow-pattern predictions and requires closure relationships to replace the information lost in the simplification process.

Also to mention is the PLAC code developed in England (Black et al. 1990), it is also a two-fluid model. Then there is the TACITE code developed at the Institut français du pétrole, it is based on drift flux type models (Pauchon et al. 1993, 1994). Another simulator based on a drift flux model is TRAFLOW, developed by the Shell Oil Company. Then there is LedaFlow another multiphase flow simulator developed by Sintef in Norway in partnership with Total and ConocoPhillips and finally commercialized by Kongsberg. LedaFlow is a highly sophisticated flow simulator solving mass, energy, and momentum conservation for each phase.

# 4. Corrosion Issue in Drilling

Corrosion is the principal cause of damage to metals in wells and production facilities and results in costly maintenance of these facilities and the loss of production. Corrosion attacks casing during drilling and producing operations through electrochemical and mechanical processes in the presence of electrolytes and corrosive agents. There are many mechanisms of corrosion that are associated with drilling wells, as illustrated in Figure 28. The most prominent factors affecting corrosion are the oxygen content in the drilling fluid, the wellbore temperature, the pH-value of the drilling fluid, dissolved salts, the presence of acidic gases in drilling fluid and high stress and pressure situations.

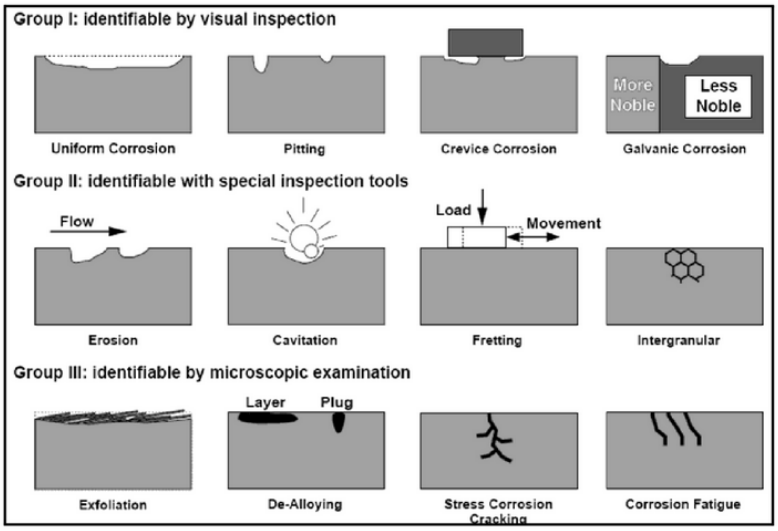


**Figure 28: Different Types of Corrosion (Roberge, 2000)**

In general drilling operations the mud composition ensures a non-corrosive environment to drill pipe. Corrosion inhibitors are often added to drilling fluids. The purpose of these additives can range from specially engineered pH additives to corrosion inhibitors that control corrosion, neutralize hazardous acid gas and prevent scale. Typical products contain both amine and phosphorus-based substances and other specially engineered chemicals. However in case formation fluids enter the wellbore and mix with the drilling mud the composition of the drilling mud gets altered and the electrochemical protection by the mud may no longer be ensured. Formation fluids may also come in direct contact with the drill pipe.

Especially kick fluids containing $H_2S$ are regarded extremely corrosive to the drilling equipment. The presence of hydrogen sulfide promotes sulfide stress cracking (SSC) or embrittlement, a corrosion mechanism that is difficult to be detected. The nature of the attack on metal is related to the alloy composition and strength of steel. Material selection for drill string design is based on the NACE MR0175 standard. Since this standard defines the maximum tensile threshold for $H_2S$-compatible steels as 110 ksi, higher grades can only be utilized as long as SSC is avoided by controlling the drilling environment. This is done by ensuring that the following four prerequisites are met:

- Maintain the drilling fluid density to minimize formation fluid influx
- Neutralize inflowing $H_2S$ by maintaining a mud pH of 10 or higher
- Utilize sulfide chemical scavengers and/or corrosion inhibitors
- Use oil-base drilling fluids

These requirements are fulfilled during controlled drilling operations. During a kick situation three of the aforementioned preconditions can be lost rapidly (sufficient fluid density/hydrostatic head, high mud pH and sufficient presence of scavengers) and drill string is exposed to a highly corrosive environment. Even without prolonged exposure of the drill string to such environments, due to the practical inability to actually measure SSC it is difficult to assess whether the drill pipe needs to be replaced or can stay in place. Therefore, if it is possible to accurately predict downhole pH developments due to influx and mixing of $H_2S$-containing reservoir fluids with the high-pH drilling mud, this will provide a decision criteria to whether circulate the kick out, kill the well and continue drilling or to kill the well and immediately pull the string out of the hole to replace it. Such simulations ultimately help to develop a sound risk assessment based on pH, $H_2S$ concentration, pressures and exposure times.

## *Corrosion Modeling*

Corrosion prediction in multiphase flow is a challenging task. Most existing corrosion models are only applicable to single phase flow. To extend the corrosion model capability to multiphase flow, the mass transfer and the turbulent diffusivity correlations in the models have to be modified to properly calculate the mass flux of corrosion species (Wang et.al. 2003).Very little work has been done so far identifying the phase interface area development through CFD modeling – mostly due to the massive computational effort required to model these environments. To assess the role of $H_2S$ in the corrosion process a detailed understanding of the underlying multiphase flow mechanisms is needed. Flow features and spatial distribution of phases are often described by a set of well-known flow patterns. Each flow pattern shows certain characteristics with respect to corrosion rate. This is certainly true as each flow pattern determines the mass transfer rate and phase interface area available for $H_2S$ dissolution.

For pipeline and wellbore applications, corrosion models need to be able to predict corrosion rates, in both single and multiphase flow conditions. It is well known that the flow variations along pipelines, such as flow regime, water wetting and liquid flow velocity, have significant effects on the corrosion process in multiphase flow conditions (Jepson et al. 1997). Flow patterns like slugging are very turbulent and can remove corrosion protection as well as corrosion products. Corrosion can be self-limiting, due to formation of corrosion scales that protect the metal underneath. The problem with slug flow is that it removes these scales and the pipe is always exposed to the corrosive environment the repeated impact of the slugs. Therefore corrosion models need to be adapted and coupled with multiphase flow simulators to compute the effects of multiphase flow.

There have been efforts to provide this coupling in the area of acid gas corrosion. Past research efforts resulted in the implementation of $CO_2$ corrosion models into the three–phase fluid flow simulator OLGA. Three empirical and semi-empirical corrosion models, NORSOK M-506, de Waard 1995, and IFE top-of-line corrosion, have been embedded as modules in OLGA. Wand and Nesic 2003 describe the coupling of a more mechanistic corrosion model with a comprehensive multiphase fluid flow model. But sour gas corrosion involving $H_2S$ is currently not considered.

## *Sulfide Stress Cracking*

High-strength steel pipes used in drilling and completion of oil and gas wells may exhibit delayed failure in environments containing hydrogen sulfide. This type of failure is referred to as sulfide stress cracking (SSC) and occurs when metal is in tension and exposed to $H_2S$ and water. The basic cause of sulfide stress cracking is embrittlement resulting from hydrogen absorbed into steel during corrosion in sour environments.

Sour gas is natural gas or any other gas that is corrosive due to a significant content of hydrogen sulfide ($H_2S$). Sour environments are defined when the partial pressure of hydrogen sulfide is above 0.0003 MPa. Partial pressure is determined by multiplying the mole fraction of $H_2S$ in the gas with the system pressure. At higher partial pressures, the corrosion rate on carbon steel is substantially increased by means of making the water phase more acidic and by forming iron sulfide scale.

The presence of water due to its electrolytic nature is needed for corrosion to take place. Although hydrogen sulfide gas can cause embrittlement, water must be present for sulfide stress cracking to occur. Hydrogen sulfide is moderately soluble in water compared to oil based fluids. Hydrogen sulfide can be destroyed by oxidation when dissolved in water. Dissolved $H_2S$ is forming a weak acid and can be regarded as a cathodic species. In contrast to water based drilling mud systems, oil-based drilling muds prevent the completion of the galvanic cell and are therefore very effective in reducing corrosion to the drilling equipment (Chilingar et al. 2008). Certain chemicals, when added to the oil-base muds, make the steel surface oil wet and protect it against corrosion.

Sulfide stress cracking is common in high strength steels containing Martensite. It can also occur in ferritic steels. The NACE standard defines SSC as the cracking of a metal under the combined action of tensile stress and corrosion in the presence of water and hydrogen sulfide. SSC is generally limited to steels having a hardness of 22 or greater on the Rockwell C scale. The occurrence of sulfide stress cracking depends on the interaction of the following parameters:

- pipe material, i.e. chemical composition, strength, heat treatment, and microstructure of the material
- pH value of the solution, i.e. concentration of hydrogen ions
- total tensile stress
- temperature

- exposure time

SSC is a type of hydrogen induced cracking (HIC) in which the primary poison is the evolution of atomic hydrogen. The source of atomic hydrogen is described by the following reaction scheme:

$$Fe + H_2S + H_2O \Leftrightarrow FeS_x + H_2 + H_2O$$

Hydrogen sulfide reacts with iron at the pipe surface, forming iron sulfide (FeS) scale and liberating two hydrogen atoms. The hydrogen ions diffuse into the steel and initially accumulate at anomalies in the metal lattice. Continuous supply and diffusion of hydrogen ions results in combination of atomic hydrogen to hydrogen molecules $H_2$ inside the metal lattice. The size of the molecules exceeds the available interstitial space and causes embrittlement between the grains of the metal. Due to the reduced metal ductility cracks will initiate, leading to crack propagation in a direction perpendicular to the tensile stress. This affects a normally ductile material making it hard and brittle. Delayed cracking is often associated with high strength of steel. High concentrations of hydrogen sulfide may act to inhibit corrosion of mild steel (Watkins and Wright 1953). However, in the case of high-strength steels, high concentrations of hydrogen sulfide produce rapid embrittlement.

## *Influence of Flow Field on Corrosion*

The presence of $H_2S$ leads to the formation of various forms of iron sulfide scales, some of them can be very protective. The formation of surface scales is therefore an important parameter affecting the corrosion rate. Surface scales are predominantly a result of direct chemical reaction between $H_2S$ and the steel surface, but can also result from precipitation in supersaturated solutions over long periods of time (Sun and Nesic 2007).

Sun and Nesic (2007) conducted experiments in galvanic cells to investigate the mechanisms and kinetics of mild steel corrosion in $H_2S$ environments. The dominant iron sulfide scale that formed under their test conditions was Mackinawite. Mackinawite scale has been shown to form extremely fast (less than seconds). *"This film is very thin (<<1µm) but dense and acts as a solid state diffusion barrier for the sulfide species involved in the corrosion reaction. The thin Mackinawite film continuously goes through a cyclic process of growth, cracking and delamination, what generates the outer sulfide layer which thickens over time (typically >1µm) and also presents a diffusion barrier; this outer sulfide layer is very porous and rather loosely attached, over time it may crack, peel and spall, a process aggravated by the flow."* The Mackinawite scale may dissolve into the solution depending on the solution saturation level. Srinivasan and Kane (1996) observed an increase in dissolution with decreasing pH, until a range of pH=2 to pH=3 where no more Mackinawite can be detected on the steel surface.

Figure 29 illustrates the molecular diffusion of both hydrogen sulfide and atomic hydrogen through the scale on the steel surface. The hydrogen sulfide arriving at the steel surface will directly react with the steel and form iron sulfide at the inner interface whereas the hydrogen

ions will permeate into the steel initiating sulfide stress cracking. The growth of the Mackinawite film at the inner interface will eventually cause delamination of the existing film and the process of film buildup will start all over again. Experiments conducted by Sun and Nesic (2007) showed that even in stagnant flow conditions even half of the scale was lost due to spalling.

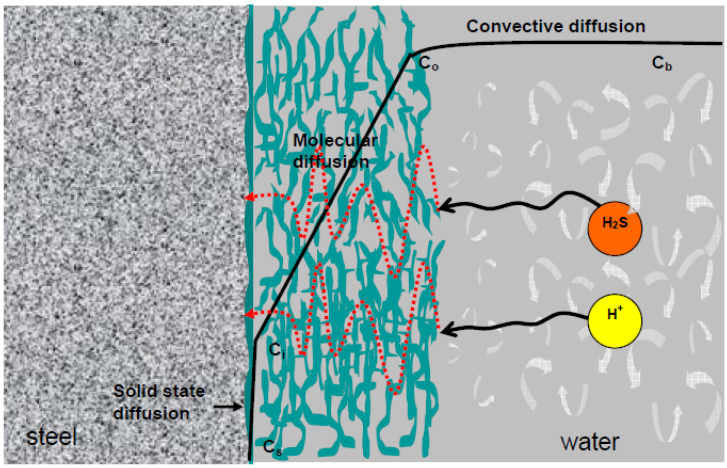


**Figure 29: A Schematic of the $H_2S$ Corrosion Process, taken from Sun and Nesic (2007)**

The passage of fluid at high velocities in case of single-phase flow, or for instance the impact of slugs in multiphase flow may remove the thin scaling film that protects the metal surface. Sun and Nesic (2007) observed a higher scaling tendency at stagnant conditions compared to flowing conditions. They concluded that a much larger fraction of the iron sulfide scale is lost to the solution due to the hydrodynamic impact of the flow.

# *Corrosion Modeling Approach*

It is known that sulfide stress cracking is influenced by three general classes of variables: environment, metallurgy, and state of stress. This work focuses on the effect of environmental factors like flow morphology, concentration of $H_2S$, and temperature (the susceptibility to sulfide stress cracking increases with increasing $H_2S$ concentration and decreases with increasing pH). Although hydrogen sulfide gas, like gaseous hydrogen, can cause embrittlement, water ordinarily must be present for sulfide stress cracking to occur. This puts water based muds into the focus when trying to predict the corrosive attack of a gas-kick event. To calculate the amount of dissolved H2S in the flow, models for gas solubility and mass transfer need to be specified.

## Gas Solubility

The gas solubility defines the maximum amount of gas that can be dissolved in a fluid at a specific temperature and pressure. Whereas bubble pressure determines at which pressure this gas would evolve from solution. The formation volume factor of the saturated fluid describes the volume variation of the saturated fluid due to the dissolved gas. These properties play an important role when dealing with the invasion of formation gas into oil-based drilling muds. According to literature larger amounts of gas can be dissolved in oil based muds compared to water-based muds. This fact is important when considering the volumetric expansion of rising gas bubbles with decreasing depth. The high solubility of natural gas in oil-based drilling fluids poses a difficulty in detecting gas-kicks. Surface responses are initially dampened and reduced well below those normally seen with water based muds. When a gas-drilling fluid mixture is circulated toward the surface, gas will evolve from solution and expand rapidly, due to the reduced pressure. This swelling behavior is not so pronounced in water based muds as a consequence of the lower gas solubility.

The problems associated with natural gas solubility in drilling fluids have been studied since 1981. The main focus of these studies was put on oil based drilling fluids and the danger associated with the volumetric expansion when the gas evolves from the solution. O'Brien (1981) suggested that the gas solubility in an oil based drilling fluid could be 10 to 100 times greater than in a water based mud. Therefore the high solubility of $H_2S$ in oil based muds is of crucial importance when it comes to kick detection. As a consequence literature presents a large number of studies dealing with the dissolution of natural gas in oil based or synthetic drilling fluids, but these types of mud are not subject of this work

For water based mud, gas solubility is generally neglected when predicting gas-kick behavior. The volumetric influence of the gas on the water based mud is insignificant. Instead the chemical processes are of great importance. The corrosive potential in water based drilling fluids is much larger compared to oil based drilling fluids. The presence of hydrogen sulfide ($H_2S$) and free water can cause severe corrosion problems. The first step in this process is the dissolution of the gas.

To characterize the dissolution of gas in a liquid the following mechanistic view of dissolution as a stepwise process is very helpful. Initially gas and liquid molecules are in separate phases. When dissolution begins a gas molecule has to be separated from its adjacent molecules and transferred to the phase interface. This transport is done by convection and/or diffusion. At the interface the molecule dissolves into the other phase and is then transported again by convection and/or diffusion to fill a vacancy in the liquid. This simplistic view helps us to think about dissolution as a transport process and allows its modeling as mere mass transfer and inherently interfacial phenomenon.

The process of dissolution will continue until a maximum concentration of gas molecules in the liquid phase is reached, termed the gas solubility. In general the maximum amount of gas that can go into solution is proportional to pressure, temperature, and chemical constituents of the liquid. For instance polar solutes tend to dissolve best in polar solvents while non-polar solutes tend to dissolve best in non-polar solvents. $H_2S$ is considerably more soluble in organic compounds than in aqueous solutions, except at high pH, the solubility increasing with increase in aromatic nature and decreasing with increase in paraffin and polar nature.

In the wellbore gas solubility is mainly affected by temperature and pressure condition. At high pressure conditions the behavior of gas deviates from non-ideal gas behavior. This can be expressed by the compressibility factor Z:

$$Z = \frac{PV}{nRT}$$

where

| | |
|---|---|
| P | pressure |
| V | gas volume |
| n | number of moles of gas |
| R | universal gas constant |
| T | temperature |

The solubility of gas in water is commonly calculated by Henry's law. This approach is appropriate as long as the pressure is low and the gas is behaving ideal. In case of high pressure conditions the solubility computations need to be improved by using a modified form of Henry's law. The modification of Henry's law is usually based on experimental data, and is specific for a certain gas and solvent.

There have been many experimental studies on the solubility of $H_2S$ in aqueous solutions. However, as $H_2S$ solutions are very corrosive, experimental measurements a generally limited to a relatively small range of temperatures, pressures, ionic strength, and the data is in general very scattered and difficult to use (Duan et al. 2007). Duan et al. summarized existing solubility models for $H_2S$ in aqueous solutions as well as existing experimental data. Based on the chemical potential of $H_2S$ in the liquid and in the gas phase, they presented a novel model covering a large temperature and pressure range with high accuracy. Calculated gas solubilities based on this model are illustrated in Figure 30. A big advantage of the model is

that it can also be applied to more complex systems, i.e. aqueous solutions with multiple components.

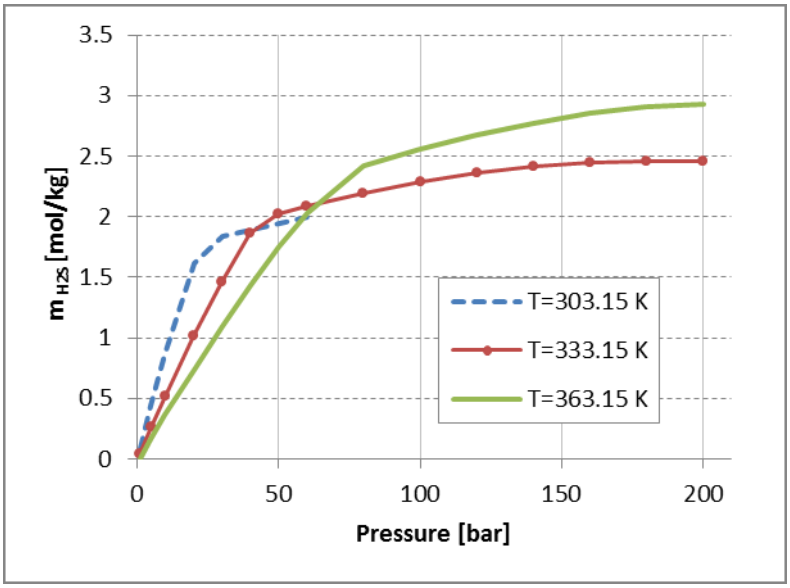


**Figure 30: Solubility of H2S in Pure Water Calculated by the Model of Duan et al. (2007)**

The solubility of $H_2S$ first increases linearly with increasing pressure, but at high pressures the slope gradually decreases.

## Mass Transfer Formulation

Gas dissolution can be described as the transfer of gas particles from the gas phase into the liquid solvent. This process can be regarded as a stepwise process. At the beginning of this process the gas and the liquid particles are spatially separated in the gas and liquid phases. The dissolution process starts with the separation of a single gas particle (solute) from the gas phase without leaving a hole. Next the gas particle is transported to the phase interface, where it gets transferred from the gas phase to the liquid phase (solvent), and eventually transported and inserted into a vacancy in the liquid phase. The dissolution process is accompanied by a change in the Gibbs free energy of the system, meaning the overall Gibbs free energy of the solution is decreased compared to the Gibbs free energy of the separated gas and liquid phases. The Gibbs energy is a thermodynamic potential that is minimized when a system reaches chemical equilibrium.

Dissolution is a kinetic process, and is generally quantified by a mass transfer rate. This rate is defined as the amount of solute that goes in solution per unit time under certain conditions regarding temperature, pressure, phase interface, solvent composition, flow regime etc. Mass transfer rate prediction is of great importance in computing corrosion rates.

The simplest approach to calculate mass transfer rate is by using Henry's law. This gas law, formulated by William Henry in 1803 states *"At a constant temperature, the amount of a given gas that dissolves in a given type and volume of liquid is directly proportional to the*

*partial pressure of that gas in equilibrium with that liquid."* The proportionality factor relating partial pressure and gas solubility factor is called the Henry's law constant.

$$k = \frac{C_S}{p_{gas}}$$

$C_S$ gas solubility
k Henry's law constant
$p_{gas}$ partial pressure of the gas under equilibrium

Henry's law describes the solubility of a specific gas in a particular stagnant solvent at a fixed temperature. Therefore Henry's law constants can be found in literature for a variety of solute and solvent pairs. Henry's law has a couple of limitations, i.e. it works only for molecules at equilibrium, it cannot be applied when there is a chemical reaction between the solute and the solvent, and moreover it does not work for gasses at high pressures. For instance Zheng et al. (2002) mention that gas dissolution computed by Henry's law deviates significantly from actual values in high-pressure conditions. Using Henry's law to calculate mass transfer is equivalent to determine the maximum amount of gas that will be dissolved at steady state conditions. Such an approach is not taking into account the movement of fluids, gas concentration variations in the solvent and available interface area between the phases.

When interested in the transient simulation of the gas dissolving process in a liquid it is necessary to formulate a model for mass transfer rate calculation. To do so the dissolution operation is understood as an interfacial phenomenon driven by a concentration difference. The temporal course of dissolution is also strongly affected by interfacial and bulk phase hydrodynamics responsible for the convective transport of species apart from molecular diffusion. The dissolution process is usually characterized by a mass transfer coefficient, K, relating the mass transfer rate with concentration gradient and available interface area as follows:

$$\frac{dm}{dt} = KMA(C_S - C_0)$$

where

m mass [kg]
K mass transfer coefficient [m/s]
M molecular weight of gas [kg/mole]
A interface area [$m^2$]
$C_S$ gas solubility [$mole/m^3$]
$C_0$ concentration of dissolved gas [$mole/m^3$]

The equation above is summarizing the stepwise process of dissolution and characterizes it with the parameters interface area, concentration difference and mass transfer coefficient. The concentration difference is defined as the difference between maximum possible solute concentration and current concentration. Calculation of concentration difference is straight forward, based on the solubility model and updated concentration values. The available interface area for dissolution is more difficult to determine. In case of perfectly round gas

bubbles the interface area is clearly defined and can be easily be calculated. The situation becomes more difficult with local deformations of the interface or irregular shapes that are not being resolved in the computation of the phase interface. In such a case a first order estimate for the interface area is used and additional local shape effects need to be included by alteration of the mass transfer coefficient. The mass transfer coefficient is the most complex parameter. When looking at the above equation it is clear that the mass transfer coefficient needs to incorporate effects of flow regime, diffusion, fluid composition etc. To account for variations in mass transfer rate due to chemical reactions an enhancement factor E can be introduced in the above equation, leading to:

$$\frac{dm}{dt} = EKMA(C_S - C_0)$$

Mass transfer coefficients can be estimated based on theoretical equations, empirical correlations, and analogies that are functions of fluid properties, system properties, and hydrodynamics of the flow. Mass transfer coefficients depend on the shape and size of the phase interface, gas diffusivity in liquids, the average fluid velocity and turbulent intensity. Several theoretical mass transfer models are available to define the mass transfer coefficient. Among these are the film theory, the boundary layer theory, the penetration and the surface renewal theory. It is not scope of this work to explain these theories, but instead to point out an appropriate definition for a mass transfer coefficient applicable to the current modeling subject.

Mass transfer coefficients are rarely reported as individual values. More commonly the mass transfer coefficient is described using a Sherwood correlation for a certain flow configuration, i.e. a situation with a known contribution of convection and diffusion. The Sherwood number (also called the mass transfer Nusselt number in analogy to heat transfer) is basically a dimensionless number used to characterize mass transfer operations. It is defined as the ratio of convective to diffusive mass transport.

$$Sh = \frac{KL}{D} = \frac{convective\ mass\ transfer}{diffusive\ mass\ tranfer}$$

where

K mass transfer coefficient
L characteristic length
D mass diffusivity

In other terms the Sherwood number is a function of the Reynolds number (Re) and the Schmidt number (Sh), with the Schmidt number representing the diffusion portion and the Reynolds number the convective contribution to the mass transfer process.

$$Sh = f(Re, Sc)$$

The function f needs to be determined from experimental data or by analysis or a combination of both. The functional relationship is commonly assumed in the following form:

$$Sh = a\, Re^{b} Sc^{c}$$

The constants a,b and c depend on the type of flow, laminar or turbulent, and the shape of the phase interface. The contribution due to diffusion is determined by the fluid properties but the convective mass transport is a matter of flow conditions. The fluid in the vicinity of the gas-liquid interface is governing the mass transfer process. If the fluid motion next to the phase interface is laminar the molecular diffusion will dominate the mass transfer process. If the fluid moves at a high velocity and the flow next to the interface becomes turbulent then convective transport becomes the main mechanism of mass transfer. The complexity of the flow field and phase interface makes the formulation of a universal mass transfer correlation impossible. Several modeling efforts and correlations exist and a short overview will be given in the next section.

Under convective conditions and for dilute systems an analogy between heat transfer and mass transfer is expected. In this case the mass transfer correlation is found by replacing the Prandtl number with the Schmidt number and the Nusselt number with the Sherwood number. In literature numerous Sherwood correlations depending on the operational conditions can be found, see some examples in Table 4. These correlations for different flow regimes are usually determined through experiments and are therefore usually valid for an overall process. As a result the accuracy of these correlations is typically of the order of thirty percent, according to Cussler (2009).

**Table 4: Typical Sherwood Correlations, taken from literature**

| Correlation | Geometry | Condition |
|---|---|---|
| $Sh = 0.332 Re^{1/2} Sc^{1/3}$ | Flat plate laminar flow | Re < 5e5<br>Sc ≥ 0.6 |
| $Sh = 0.0296 Re^{0.8} Sc^{1/3}$ | Flat plate turbulent flow | 5e5 < Re < 1e8 |
| $Sh = (0.037 Re^{0.8} - A) Sc^{1/3}$ | Mixed flow over a plate | 0.6 < Sc < 60<br>5e5 < Re < 1e8 |
| $Sh = 2 + 0.6 Re^{1/2} Sc^{1/3}$ | Rising bubbles in a stagnant fluid | |
| $Sh = 0.023 Re^{0.83} Sc^{1/3}$ | Cylinder in cross flow, evaporation of liquid wall film to gas core | 0.4e4 < Re < 7e4<br>0.6 < Sc < 3e3 |

| | | |
|---|---|---|
| | (Chilton-Colburn) | |
| $Sh = 0.3 + \left[0.62 Re^{\frac{1}{2}} Sc^{\frac{1}{3}} \left[1 + \left(\frac{0.4}{Sc}\right)^{\frac{2}{3}}\right]^{-\frac{1}{4}}\right]\left[1 + \left(\frac{Re}{282000}\right)^{\frac{5}{8}}\right]^{\frac{4}{5}}$ | Cylinder in cross flow<br>(Churchill-Bernstein equation) | ScRe ≥0.2 |

Mass transfer is assumed to be strongly affected by turbulent eddies around the phase interface. Introducing the concept of turbulence instead of using empirical parameters in the definition of the mass transfer coefficient is subject of the penetration theory and the surface renewal theory.

The penetration theory was proposed by Higbie in 1935. He regarded the gas-liquid interface to be made up of a variety of small liquid elements, which are continuously brought up to the surface from the bulk of the liquid by the motion of the liquid phase itself. Mass transfer takes place by diffusion in the various elements at the interface. Therefore the mass transfer coefficient in the liquid phase is only dependent on the diffusion coefficient and the residence time of liquid element at the phase interphase and is defined by

$$K = 2\sqrt{\frac{D}{\pi\tau}}$$

τ residence time of a liquid element at the phase interface

This model represents a first step towards the development of a turbulence hypothesis in mass transfer. However his assumption that the residence time is the same for all liquid elements is not realistic.

An improvement of the penetration theory is achieved by using a surface renewal mechanism or eddy cell model. The underlying assumption states that a surface is intermittently replaced by well-mixed fluid from adjacent layers due to the viscous and inertial motion of eddies. This approach provides a link between the observed mass transfer behavior and the state of the turbulent field and was first suggested by Danckwert in 1951. The mass transfer coefficient resulting from this model is proportional to the square root of the diffusion coefficient and the rate of surface renewal as follows

$$K = \sqrt{\mathrm{Ds}}$$

s rate of surface renewal

Based on the surface renewal theory of Danckwert several formulas have been postulated in literature. Among them is the relationship derived by Lamont and Scott (1970) who assumed that every eddy in the inertial sub-range of turbulence contributes to the surface renewal. The mass transfer coefficient in terms of rate of energy dissipation is given by:

$$K \propto \left(\frac{\mu_l}{\rho_l D}\right)^{1/2} \left(\frac{\varepsilon \mu_l}{\rho_l}\right)^{1/4}$$

ε rate of energy dissipation

At this point I want to conclude the description of mass transfer models in full agreement with the words of Aiman Eid Al-Rawajfeh (2004):

*"In many circumstances the difference between predictions made on the basis of the different models will be less than the uncertainties about the values of the physical quantities used in the calculation. The models can thus be regarded as interchangeable for many purposes, and it is then merely a question of convenience which of them is used."*

# 5. Modeling Approach

Modeling the transient behavior of a gas-kick with the aid of Computational Fluid Dynamics confronts the researcher with several challenges. An extreme geometric configuration: with a well depth of more than 1000 m and an annular clearance of only a few centimeters, the uncertainty about the inflowing gas: regarding composition, pressure, and location of inflow, and the need of a high spatial resolution. Nevertheless modeling of multiphase flow is a computational challenge itself.

So based on these facts a thorough understanding of the flow problem is essential to allow physically meaningful simplifications to be made. Assumptions about the inflow scenario and gas composition need to be made. The dominant forces need to be identified to allow decisions on what physical models are needed and what effects can be neglected. Otherwise a full mapping of the flow problem via simulation is not technically feasible.

The goal of this work is to better understand the gas-kick behavior through CFD simulation and to evaluate possible simulation strategies.

The modeling approach of a gas-kick involves simulation of the following mechanisms and tasks:

- Mud circulation (non-Newtonian mud)
- Drill pipe rotation
- The influx of gas into the wellbore
- The mixing between the gas and the mud phase
- Dissolution of gas / modeling of mass transfer
- Analysis and quantification of relevant flow variables
- Summarizing influences and drawing conclusions

Assumptions made to simplify the model are:

- Two-phase flow (only gas and liquid)
- No cuttings effect
- Constant annular geometry
- Concentric annulus
- Constant mud pump rate
- Constant formation pore pressure

# Simulation Tool

In the current work the commercially available CFD solver ANSYS, Fluent is used as simulation tool. In FLUENT the finite volume method is used to discretise the transport equations. This CFD software offers a broad range of mathematical models for transport phenomena and provides great flexibility to enhance the model abilities via the use of user defined functions (UDF). In the current model this option is used to compute gas solubility and mass transfer coefficients.

# Model Setup and Boundary Conditions

## Model Geometry

To determine the multiphase flow field during a gas-kick, including gas dissolution the solution of the Navier-Stokes equations for a transient multi-phase turbulent non-Newtonian fluid flow is required. Ideally, a fully three dimensional representation of the wellbore would be required. There is no analytical solution to this flow problem, and a numerical full size simulation is computationally prohibitive. Consequently, to enable a reasonable investigation of this problem simplifying assumptions are made.

It was decided that the simulation should focus on the transient onset of the gas-kick at wellbore bottom where a kick is assumed to occur most likely. Therefore an axisymmetric representation of the near wellbore-bottom region is chosen, with axial symmetry about the centerline of the drill pipe. The length of the geometry is 3 m to ensure sufficient grid resolution and reasonable CPU time. The domain length corresponds to 118 times the annular clearance of 2.54 cm, which should be sufficient to cover not only the kick entry zone but also allow full development of the flow. The open-hole section is assumed even without any washouts. The drill pipe and formation are aligned fully concentric. The diameter of the open hole section is 8.5 inch (21.59 cm) and the outer diameter of the drill pipe is selected to be 6.5 inch (16.51 cm), resulting in an annulus diameter ratio of:

$$K = \frac{outer\ diameter\ of\ the\ drill\ pipe}{open\ hole\ diameter} = \frac{21.59\ cm}{16.51\ cm} = 1.31$$

Fluid flow down the drill pipe is not modeled. The modeled domain encompasses the bottom-hole section (where the drill bit is located) and the formation drill pipe annulus. There is no flow exchange between the annulus and the adjacent formation except for dedicated locations to model the gas-kick entry. The outer boundary of the wellbore is assumed to be hydrodynamically smooth and is modeled as a no slip boundary meaning fluid velocity drops to zero at the wall. A no-slip condition is also active at the drill pipe boundary, causing the fluid to stick to the wall and move at the same velocity when the pipe is rotated. Figure 31 shows a sketch of the modeled domain rotated counterclockwise by 90 degrees. The drilling process itself is not modeled, i.e. the geometry in the wellbore remains constant throughout the simulation.

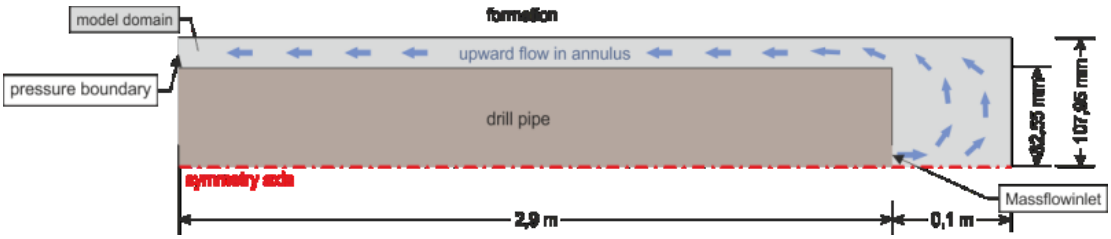


**Figure 31: Model Setup**

## Multiphase Flow Model

When carrying out a two-phase flow simulation with FLUENT one has to select the appropriate multiphase model according to the expected flow pattern, as discussed earlier. There are different two-phase flow models available according to the size of the phase volume fraction as well as whether the flow is dispersed or segregated. For instance for a dispersed flow simulation it is necessary to have knowledge about the bubble or droplet size distribution a priori. In the present study of a gas-kick such information is not available. As mentioned earlier it is actually not fully clear what type of flow patterns are evolving.

Therefore the two-phase flow modeling approach adopted for this work is an Euler DNS based on the volume of fluid method (VOF). Many other modeling approaches need assumptions that actually constrain the nature of the solution, whereas with the volume of fluid method no such a priori foundations are needed. The major requirement for a valid solution is an appropriate selection of the grid resolution to ensure that the fluid interface is captured properly. Whether the grid resolution fulfills this requirement or not can be validated by analyzing a histogram of the phase volume fraction. Uniform distribution of phase volume fractions indicates a smeared phase interface which is a consequence of coarse grid resolution. Whereas sharp peaks at phase volume fractions close to zero or one indicate good grid resolution and hence good modeling quality, as can be seen in Figure 32 and Figure 33.

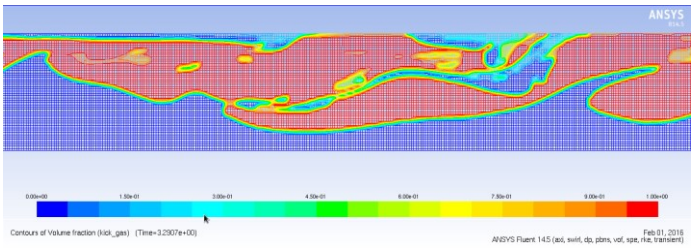

**Figure 32: Contour Plot of Gas Volume Fraction**

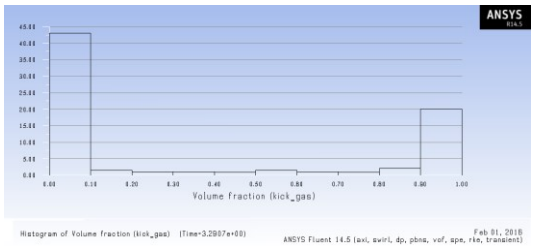


**Figure 33: Histogram of Gas Volume Fraction**

With the selection of the volume of fluid method and an appropriate mesh resolution not only segregated flow can be modeled but also dispersed flow at an arbitrary phase volume fraction, as long as the mesh size is much smaller than the dispersed interfacial structures. This approach is well suited to gain information on the arising flow pattern and phase interface location.

Within the volume of fluid method there are several options for the reconstruction of the phase interface. During the course of this work two of these algorithms, namely the

- Geometric reconstruction scheme, and the
- CICSAM scheme

have been tested for their applicability. The first, the geometric reconstruction scheme is based on a piecewise linear interface calculation (PLIC) method that was introduced by Youngs (1982). It is reported to be of high accuracy and well suited for unstructured grids.

CICSAM is a higher order differencing scheme to compute interface geometry and orientation. This algorithm is computationally less expensive compared to the geometric reconstruction scheme. It provides interface sharpness at the same level as the geometric reconstruction scheme and is particularly suited for fluid flows with high viscosity ratios.

Both schemes are implemented in FLUENT and after an evaluation of both it was decided to favor the CICSAM scheme due to its robustness, high interface sharpness and computational advantage. Actually the phase interface reconstructed with the geometric approach often showed very edged interface steps that appeared unnatural, whereas the CICAM scheme provided a generally smoother interface and seems to lack the ability to reproduce small gas bubbles. The phase contour plots shown in Figure 34 and Figure 35 depict the phase distribution in a subsection of the annular channel; the gas phase is illustrated in white and the liquid phase in black. Both approaches provide very sharp interfaces. The images are taken from different simulation cases but still show the mentioned peculiarities of the two schemes quite clear.

**Figure 34: Geometric Interface Reconstruction**

**Figure 35: Interface Reconstruction using CICSAM**

Surface tension effects at the interface are included by the continuum surface force (CSF) model proposed by Brackbill et al. (1992) which is available in FLUENT.

## Turbulence Modeling & Grid Considerations

Selection of the mesh has a significant impact on the rate of convergence, solution accuracy and computational time required. Mesh quality ensuring good numerical accuracy and a minimum of numerical diffusion is achieved by appropriate grid resolution, low cell skewness, small size ratio of adjacent cells, an appropriate boundary layer mesh, and local mesh refinement where needed. In the first modeling step, a grid resolution study has been conducted. Grid independence of the solution is achieved when an increase in cell number is not affecting the results. This goal was ultimately met by using quadrilateral cells with a size of 0,5 mm and certain mesh refinement at gas inlet zones.

Based on the Reynolds number calculated for mere mud circulation, the single phase flow would be classified as laminar. However due to the entrance of the kick gas turbulences will arise. Unless a direct numerical simulation with respect to time is planned, an appropriate turbulence model needs to be selected for the simulation. The realizable k-epsilon model has proven to be most applicable for this purpose. Fluid flows are significantly affected by the presence of walls, since this is the location where turbulence is effectively generated. When using a turbulence model for simulation of the bulk flow special treatment is needed for the flow in the near-wall region. The near-wall region can be subdivided into three zones with different characteristics as shown in Figure 36. The parameter y+ is a non-dimensional distance from the wall, critical in the assessment of mesh quality. It is defined as the shear velocity times the normal distance from the wall divided by the kinematic viscosity.

$$y^+ = \frac{U_T y}{\nu}, \quad U_T = \sqrt{\frac{\tau_w}{\rho}}$$

$U_T$ shear velocity
y normal distance from the wall

The innermost layer of the boundary layer profile is the viscous sublayer next to the wall which is characterized by laminar flow. In this layer molecular viscosity plays a dominant role. Then there is the outer fully turbulent layer, where the flow is no more affected by the presence of the wall. Between these two regimes a buffer layer or blending region is located, where viscosity and turbulence are equally important.

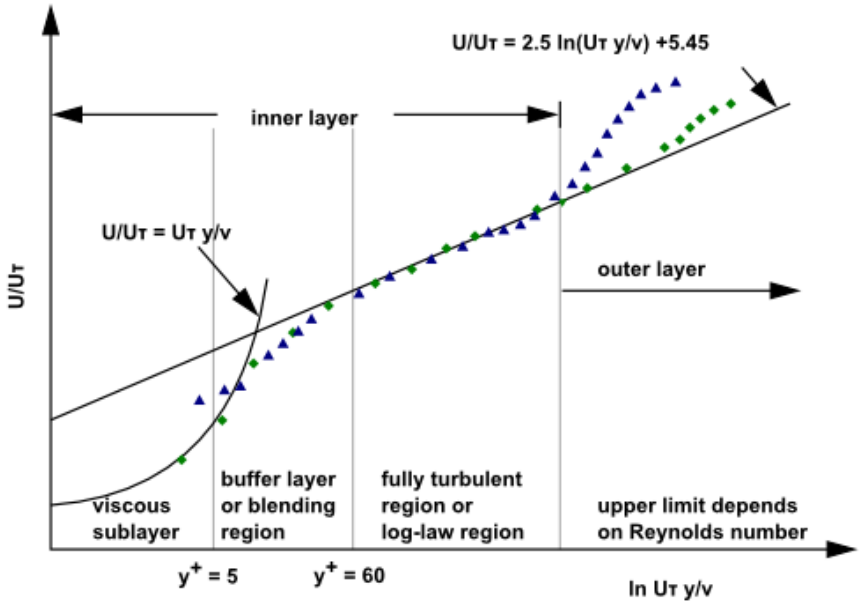


**Figure 36: Subdivisions of the Near-Wall Region (FLUENT manual)**

To properly capture the boundary layer profile it is necessary to refine the computational grid accordingly. A considerable amount of additional cells may be required for this task and the size of these cells imposes a restriction on the size of the time step. Since for an explicit calculation (transient simulation) the magnitude of the step is governed by the smallest length scale. So in case of very small computational cells this can lead to extremely small time steps and increased CPU requirements.

An alternative practice in turbulence modeling is to apply appropriate near wall models to bridge the low Reynolds flow in the vicinity of the wall with the high Reynolds flow in the bulk fluid. In this case no local mesh refinement is need. The concept of these two approaches is shown in Figure 37.

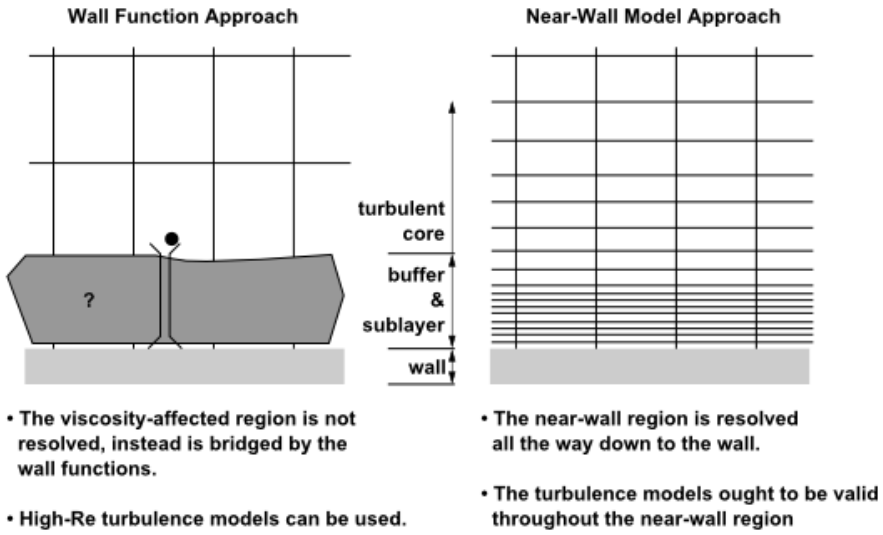


**Figure 37: Near-Wall Treatments (FLUENT manual)**

Regarding the application of wall functions there is a restriction in acceptable y+ values for the validity of these semi-empirical models. The general criteria requests mesh resolution fulfilling y+ values of > 15, otherwise the numerical results deteriorate and the accuracy of the solutions cannot be maintained. This shortcoming was met by the introduction of scalable wall functions which allow the application of the wall function approach to fine grids with y+ values below 15. This improvement is essential for the current simulation task, since the small annular clearance of the flow domain and the request to capture the phase interface demands for a high grid resolution. This high resolution grid would have counter indicated the application of wall functions due to the small y+ values present. On one hand, to fulfill the y+ criteria of standard wall functions the grid would have needed to be so coarse that the flow could not be properly captured and on the other hand a further grid refinement required for a direct numerical simulation was undesirable due to the tremendous CPU requirements. With the application of scalable wall functions consistent results are produced for grids of arbitrary refinement. Apart from y+ considerations it is necessary to resolve the boundary layer with at least 10 cells in the wall normal direction. Therefore the boundary layer mesh needs to be examined critically and updated if necessary to meet this criterion.

However caution needs to be taken when applying such single-phase wall functions in multiphase flow. The use of wall functions may be inadequate when several phases exist near the wall. For instance a high concentration of dispersed phase is present in a continuous phase layer at the wall. The dispersed phase bubbles could give rise to an additional source of turbulence which will not be covered by the wall function approach. Due to the lack of appropriate two-phase wall functions in FLUENT this effect could not be addressed in the current simulations.

Eventually quadrilateral elements of uniform size were selected to mesh the annulus and triangle elements are used to model the wellbore bottom including the drill bit section. The fluid flow in the annulus is mostly aligned with the grid except for the very beginning of the annulus next to the wellbore bottom, where the flow strongly deviates from the axial coordinate due to entry effects. The quadrilateral elements have a side length of 0.5 mm. The overall model contains 400,000 cells.

The realizable k-ε model combined with the scalable wall functions approach is the turbulence model used throughout this work. For all calculations the variable time step option is selected to ensure a Courrant number smaller or equal to 0.25.

## Representation of Drill Bit

At the beginning of this work careful consideration regarding the modeling of the drill bit and its influence on the flow field was taken. The direct representation of the drill bit geometry in the CFD model would demand enormous meshing effort to account for the details in design and nozzle arrangement. Instead a generalized representation of the flow field near the drill bit appeared more appropriate. For this representation one central drilling mud inlet at the centerline of model is used. The mass flow of the mud is kept constant and pointing downward directly towards the formation. The volume usually occupied by the drill bit, 10 cm in height and confined by the outer model radius, is constantly rotated at 100 rpm. This configuration induces two big Taylor vortices at the bottom of the wellbore which mimic the rotating parts of the drill bit. Figure 38 and Figure 39 show contour plots of the velocity magnitude and total pressure respectively. Both images are rotated counterclockwise. When the mud stream eventually enters the annular gap it is still deflected from the bottom-hole vortex and needs a certain distance until it aligns with the vertical axis.

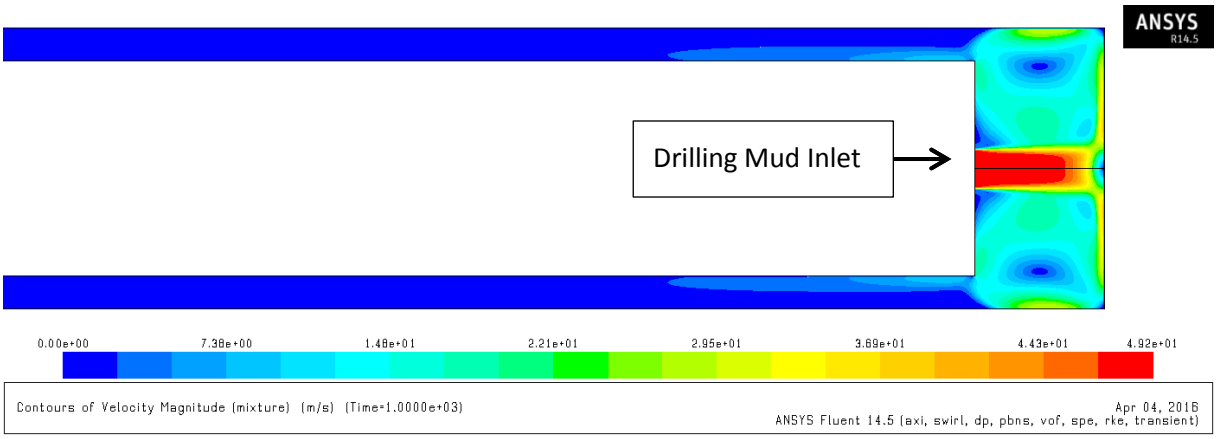


**Figure 38: Velocity Magnitude during Mud Circulation**

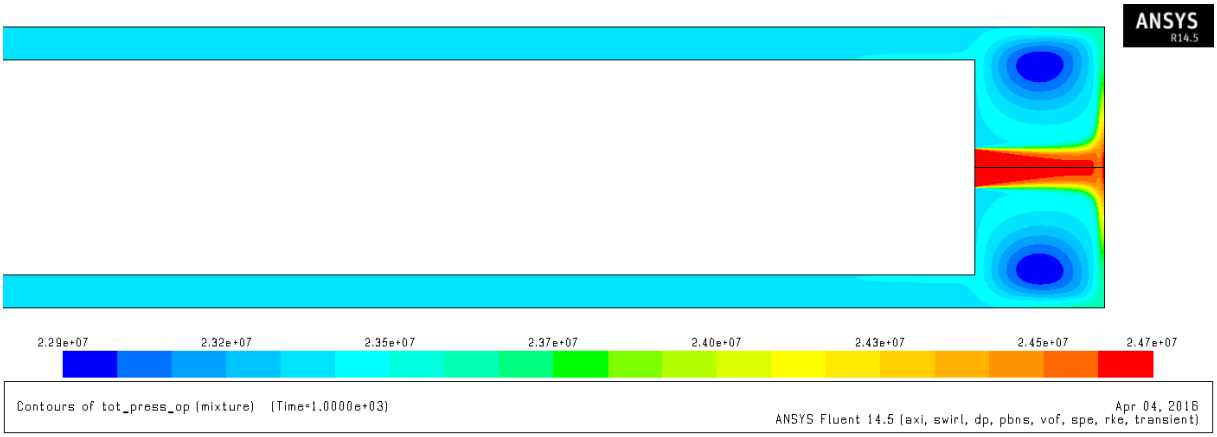


**Figure 39: Total Pressure during Mud Circulation**

## Drilling Mud Circulation

To properly model the non-Newtonian behavior of the drilling mud a rheological model is required that accurately describes the relation between shear rate and shear stress. The Herschel Bulkley model describes the majority of drilling fluids quite well, so this model was selected with parameters according to Table 5.

**Table 5: Drilling Mud Properties**

| | | |
|---|---|---|
| Density | 1190 | [kg/m³] |
| Consistency Index k | 0.5438 | [Pa·s$^n$] |
| Power Law Index n | 0.5403 | |
| Yield Stress Threshold | 0.9576 | [Pa] |
| Plastic Viscosity | 0.015 | [Pa·s] |
| Critical Shear Rate | 63.84 | [s$^{-1}$] |

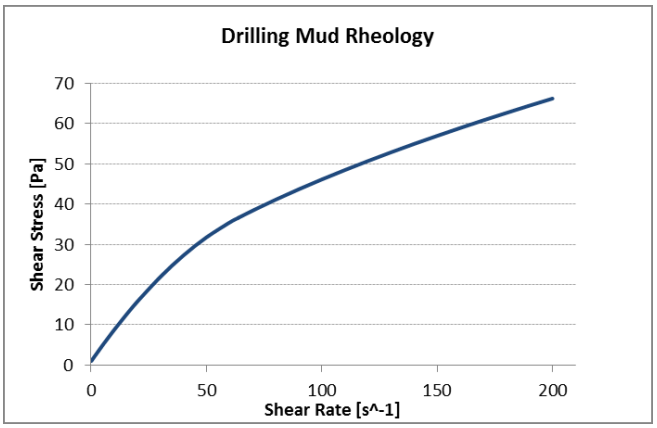


**Figure 40: Drilling Mud Rheology**

Single-phase flow of the drilling mud exists inside the drill string, this flow domain is not included in the model. Drilling mud is entering the model domain through a single nozzle with a diameter of 3 cm located at the center line. The inflow of drilling mud is modeled with a mass-flow boundary. The mass flow is kept constant at 39.67 kg/s. This is equivalent to a pump rate of 2000 l/min, resulting in a Reynolds number of about 4600 for the mere liquid flow in the annulus. Single-phase mud flow exists in part of the annulus, i.e. above the two-phase mixture of the evolving kick, and is accelerated due to the displacement by the entering gas. When a kick occurs the formation fluid displaces the heavier mud in the wellbore causing the pressure in the well to drop. Therefore the pressure differential between the formation and the wellbore increases and the kick will accelerate and grow. To account for this effect, the pressure outlet boundary at the upper end of the model is equipped with a user defined function to automatically adjust the pressure boundary according to the gas flowrate at the outlet. The calculation of hydrostatic pressure drop due to mud displacement is based on the local gas density. An additional mud displacement due to gas expansion while the gas is travelling to the surface is not taken into account in this model.

## Influence of Rotation

Drill pipe rotation is modeled by a moving boundary condition at the inner cylinder and a rotating fluid zone at the drill bit location. The configuration of an annular flow domain with a rotating inner cylinder and a stationary outer cylinder quickly reminds one of the well-known Taylor vortex flow instability. The tendency whether this flow instability is likely to occur in the current setup, can be assessed by calculating the Taylor number. The Taylor number characterizes the importance of centrifugal forces due to rotation, relative to viscous forces. The Taylor number Ta is defined by

$$Ta = \frac{R_1 \Omega_1^2 d^3}{\nu^2}$$

where,

| | |
|---|---|
| $R_1$ | radius of the inner cylinder |
| $\Omega_1$ | angular velocity of the inner cylinder |
| d | annular gap between cylinders |
| v | kinematic viscosity |

The current setup with a drill-pipe rotation of 100 rpm, an annular gap of 2.5 cm, a radius of the inner cylinder of 8.26 cm, and a dynamic mud viscosity of ~0.5 Pa·s results in a Taylor number of ~800. This is far below the critical Taylor number 3400, which indicates the onset of the flow instability. This means that even without mud circulation and hence no axial flow component Taylor-Couette flow vortices are very unlikely to occur inside the annulus. The vertical flow component will additionally suppress the evolution of radial vortices.

The ratio between the centrifugal force responsible for the Taylor instability and the inertia force of the axial flow component can be quantified by the Rossby number, defined by

$$Ro = \frac{R_1 \Omega_1}{j_L} = \frac{R\omega}{Re}$$

where,

| | |
|---|---|
| $j_l$ | axial fluid velocity |
| Rω | rotational Reynolds number |
| Re | Reynolds number |

A Rossby number greater than unity indicates a dominant centrifugal force and consequently the onset of a Couette flow instability. The Rossby number for the current model setup lies below 0.4. This means that the axial flow component is much stronger than the radial flow caused by rotation. The high pumping rate, the small annular gap size, the low rotation rate, and the high mud viscosity are counteracting the evolution of radial flow. In case a radial flow component is desired for instance to increase mixing of the phases, these parameters need to be altered correspondingly.

However in the bottom-hole zone below the drill pipe the critical Taylor number is exceeded and the formation of Taylor vortices is noticed. As mentioned earlier these vortices are

utilized to represent the drill bit geometry. The effect of rotation is basically stabilizing the flow field as can be seen in the images below. Figure 42 and Figure 44 show the flow field in case of drill bit rotation whereas Figure 41 and Figure 43 show the flow field evolving without rotation. In case of rotation the mud stream is more pronounced due to the confinement caused by the Taylor cells. The mud branching off the vortex and entering the annulus initiates a counter-vortex in the annulus. However in case of no rotation the mud entering the zone is quickly diverted and eventually enters the annulus quite uniformly.

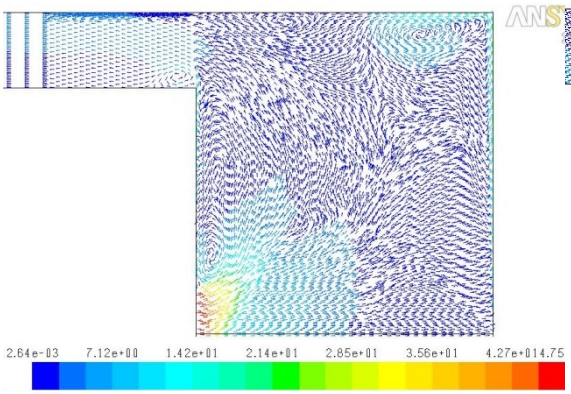


Figure 41: Velocity Vectors, no Rotation

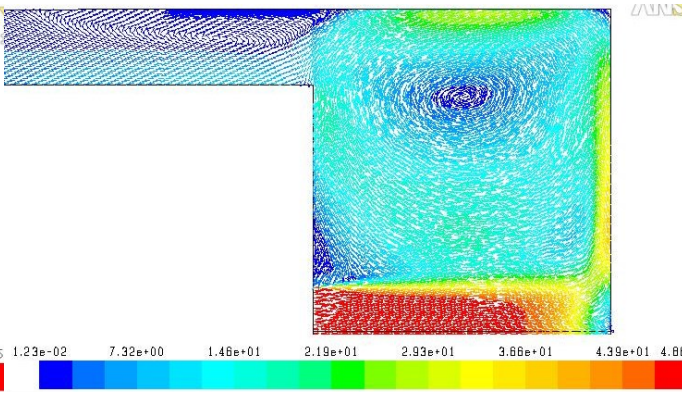


Figure 42: Velocity Vectors, Drill Bit Rotation 100 rpm

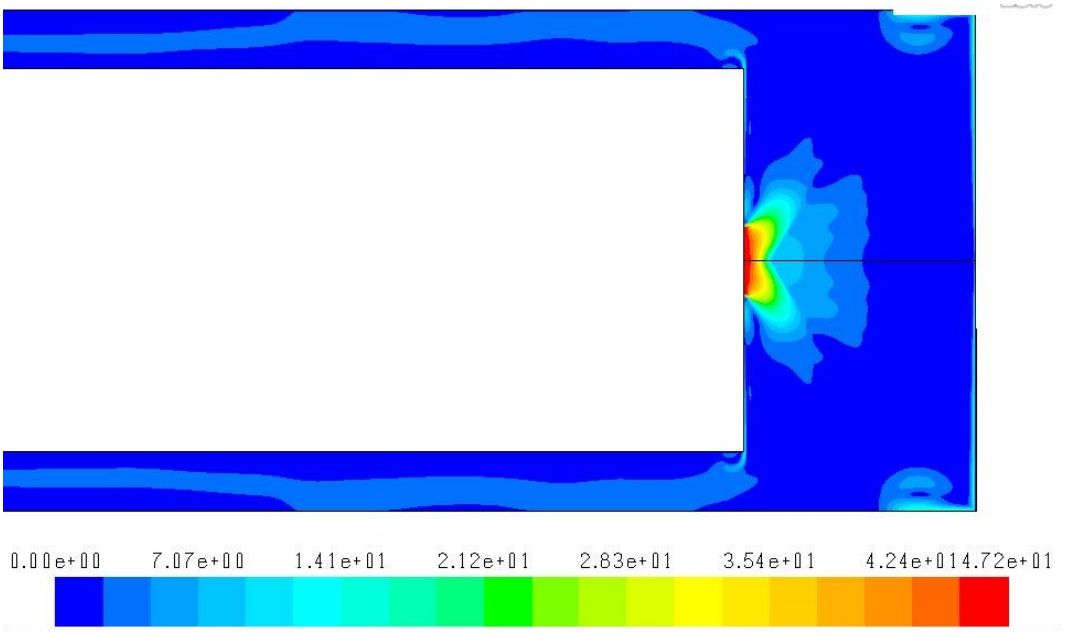


Figure 43: Contours of Velocity Magnitude, no Drill Bit Rotation

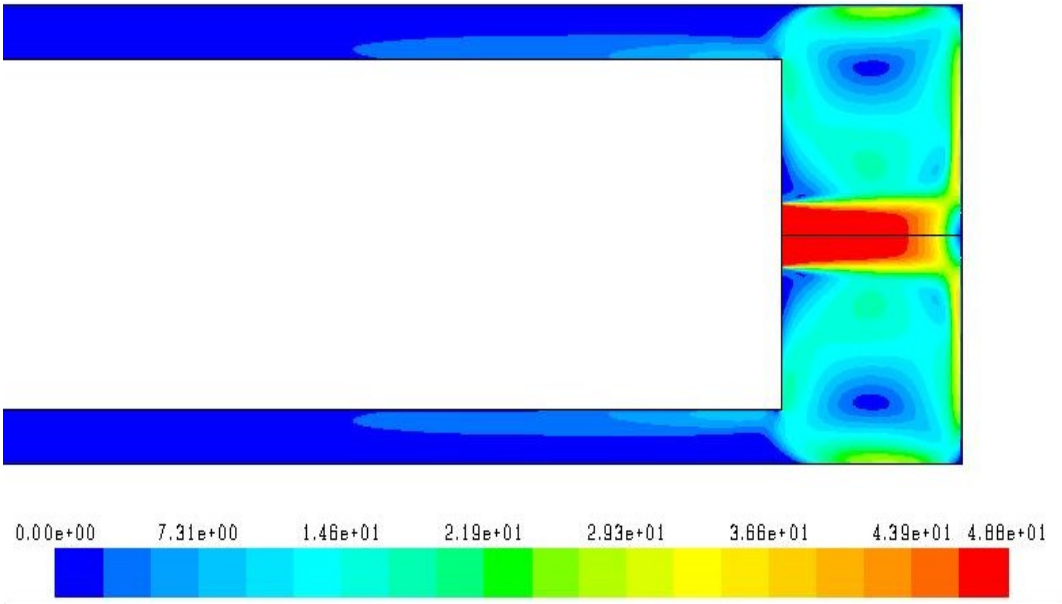


**Figure 44: Contours of Velocity Magnitude, with Drill Bit Rotation 100 rpm**

## Pressure Situation

The primary cause for a kick to occur is a lower mud pressure than formation pore pressure especially due to pressure transients. The pressure situation in a wellbore during drilling is illustrated in Figure 45. The dotted green line shows the static pressure applied by the pumps at point b, the increase in pressure from b to c is made up by the hydrostatic head of the mud column minus the frictional pressure losses in the drill string. At the wellbore bottom the drill bit causes a drop in pressure from point c to d. The pressure drop in the annulus is more pronounced compared to the pressure drop in the drill string due to the increased frictional pressure losses in the open-hole section and the flow resistance of the casing shoes. The formation pore pressure is shown in red and the fracture pressure in blue. During conventional overbalanced drilling operations the wellbore pressure in the annulus has to be kept inside the narrow pressure window between the blue and the red line. This circulating mud pressure or equivalent circulating density (ECD) needed is defined as

$$ECD = hydrostatic\ head + friction\ pressure + surface\ back\ pressure$$

The circulating mud pressure in the annulus needs to be larger than the formation pore pressure to avoid formation fluid influx and lower than the fracture pressure to avoid fracturing the formation.

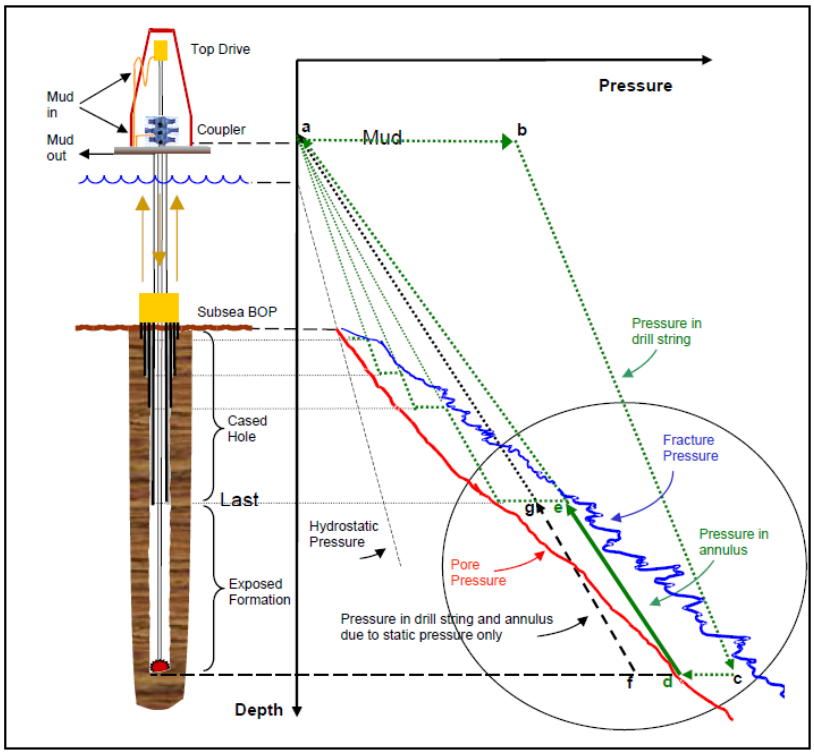


**Figure 45: Wellbore Pressure Situation (taken from http://maris-eu.com)**

Formation fluid influx occurs whenever the pressure of a gas-bearing formation exceeds the pressure in the wellbore. Such pressure differentia can be caused by an unexpected rise in formation pressure or a decrease in wellbore pressure, possible causes are listed in Table 6.

**Table 6: Pressure Situations Causing a Kick**

| **Kick Causes** | |
|---|---|
| **Reduction in wellbore pressure:**<br>• making a connection & stopping circulation<br>• during tripping<br>• swabbing<br>• lost circulation<br>• low density drilling fluid<br>• gas/oil/water cut | **Increase in formation pressure:**<br>• unexpected high pressure regions |

A rise in formation pressure can be due to geological processes that have occurred in the region being drilled. Wells are drilled in regions where oil and gas are trapped, and the same processes that create the hydrocarbons can also produce large pressures. Therefore, it is not uncommon to come across regions of abnormally high formation pressure while drilling.

The mud pressure during circulation is the sum of hydrostatic head of the mud, dynamic head due to pumping and surface backpressure. Therefore a reduction in wellbore pressure happens if at least one of these components drops without compensation by another. The hydrostatic head in the wellbore can drop due to improper well operations. For instance during tripping when the drill string is pulled from the hole continuous pumping of mud is needed to replace the volume of the removed pipe with mud. Swabbing can also produce wellbore pressure drops when done too quickly, especially with high viscosity muds and with small annular clearance. Low drilling mud density or lost circulation can also cause a reduction in hydrostatic head. The drilling fluid density may be reduced by the influx of formation fluids and/or the settling of weighting material. The drilling mud is the well's primary well barrier, when the fluid volume is lost to the formation or its pressure is too low the result will be inflow of formation fluids.

Fraser et al. (2014) have analyzed kick detection data from drilling operations in the Gulf of Mexico. As a result they identified five main drilling related operations that are estimated to account for 95% of all kick events in this area, shown in Figure 46. According to their study about 70% of the kicks occurred when making a connection. When making a connection the pumps are turned off and the mud pressure level in the wellbore reduces to the hydrostatic head of the mud column. After a connection is established, circulation is restarted and the mud pressure in the bore hole rises again rapidly. This transient pressure drop and rise can be very dramatic and overshooting the balance before stabilizing. The negative pressure surge may induce flow from the formation if it falls below formation pore pressure. With each connection the exposed formation is repeatedly depressurized before and supercharged after the connection is established. According to Fraser et al.'s study such pressure fluctuations in the wellbore are the main causes for a kick, i.e. tripping out and making a connection sum up to 85% of the kicks analyzed. With continuous circulation techniques during connection operations these transient pressure fluctuations can be avoided and the flow is kept steady.

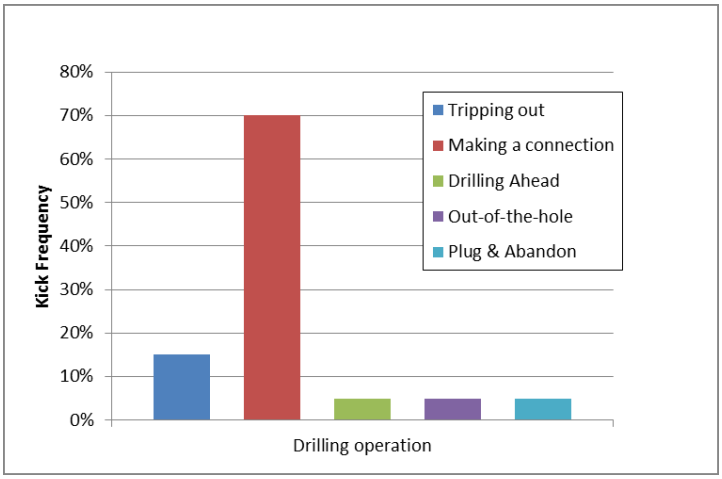


**Figure 46: Kick Frequency in Drilling Operations, according to Fraser et al. (2014)**

## Kick-Gas Inlet Condition

When investigating possible scenarios for a gas-kick, with the aim to identify the most probable location for the kick to enter, one has to analyze the fluid pressure situation in the wellbore. Usually a gas-kick will occur when drilling into formations with pressures higher than anticipated and a bottom-hole pressure too small to counteract formation pressure. As mentioned earlier the hydraulic pressure is making up the major portion of the wellbore pressure. As the pressure in the wellbore is not uniform, the kick is likely to occur at the "weakest point" along the wellbore/formation interface.

In general the well is kept under control by using a drilling mud with a density sufficient to keep the hydrostatic pressure well above formation pore pressure. However when considering the pressure impact of the moving fluid, it is possible that the flow situation in the wellbore may cause local zones with a lower pressure than assumed. This is especially true at narrow flow passages or strong deflections in the flow path. As the passage becomes narrower the velocity of the mud passing trough will increase and the static fluid pressure will drop, just similar to the working principle of a Venturi pipe. This drop in static pressure is commonly used to aerate flows, as shown in Figure 47. The narrow passage of the pipe is used to draw air into the water stream, basically a kind of "desired gas-kick" situation. Similarly in case the static wellbore pressure becomes considerably lower than the formation pore pressure, fluid will be pulled into the wellbore. Such spots of low static pressure can cause a continuous inflow of small amounts of gas. This inflow may not threat overall well control but can have a considerable impact on the drilling string in terms of corrosion.

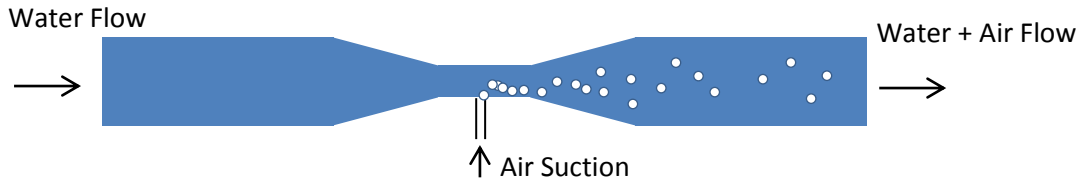


**Figure 47: Venturi Aerator**

Figure 48 shows the total pressure, i.e. sum of static and dynamic pressure, in the wellbore model during mud circulation. The pressure range is clipped; the gradual hydrostatic pressure increase can clearly be seen as well as the high dynamic pressure regions due to the flow in the drill bit area.

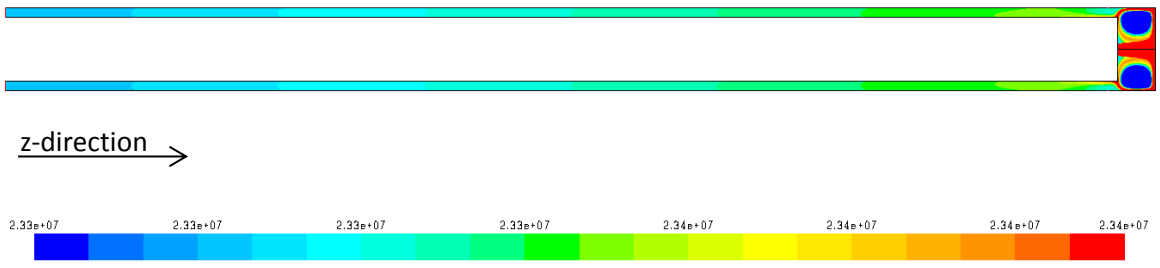


**Figure 48: Total Pressure [Pa] during Mud Circulation**

The mere wellbore pressure without the dynamic fluid pressure is shown in Figure 49. This contour plot of static pressure shows high pressure spots at the wellbore bottom center and corners. These locations are basically stagnation points and the associated pressure is referred as stagnation pressure, caused by the impact of the mud jet at the wellbore bottom. Based on the impact angle of the fluid, the fluid velocity drops and its kinetic energy is converted into pressure energy. Consequently the energy conversion is largest were the fluid is hitting the boundary perpendicularly and not existent where the fluid is moving tangentially. On the other hand an increase in fluid velocity is balanced by a drop in static fluid pressure. Naturally the location of the extreme pressure spots are a consequence of the current model setup and will be different for real bit geometries. Nevertheless the model represents the extreme bottom-hole pressure conditions that will also be encountered under real conditions.

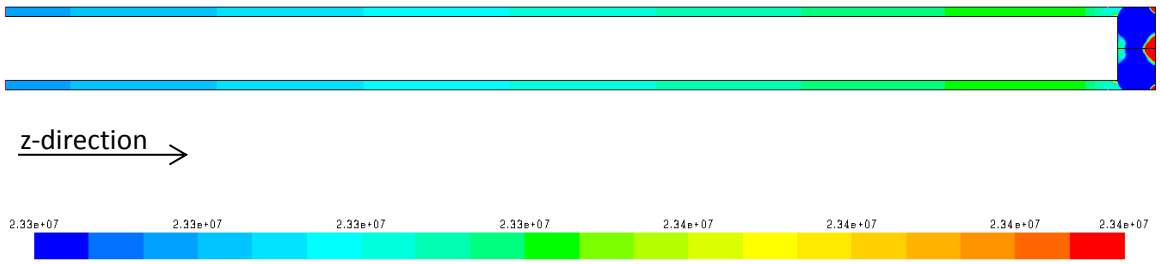


**Figure 49: Static Pressure [Pa] during Mud Circulation**

The static pressure shown in Figure 49 is relevant for the occurrence of a kick. Since this is the pressure available to balance formation pore pressure along the open hole boundary between mud and formation. Any imbalance accounts for flow either into the formation or into the wellbore. Therefore it is necessary to have a closer look at the static pressure profile along the wellbore-formation boundary, as shown in Figure 50. The hydrostatic fluid column accounts for the major part of the pressure in the wellbore, but there is also pressure needed to move the drilling fluid up the annulus and overcome the frictional resistance. The annular friction pressure losses depend on the resistance in the annulus and the velocity of the fluid. The losses are usually small in large diameter holes and higher in annuli with small annular clearance. The difference between the hydrostatic and the static pressure is very small in the annular section of the model, since the boundary is assumed hydrodynamically smooth. Close to the wellbore bottom first a slight drop in pressure followed by a pronounced pressure fluctuation can be seen. The drop in static pressure is caused by the high velocity mud stream released from the dill bit. Thus the static pressure at the wellbore-formation boundary during circulation is actually lower than the hydrostatic pressure present if the mud would be at rest. In the current model configuration the highest drop in static pressure at the lateral boundary amounts ~3.5 bars. Locations of high pressure seen in the plot are due to fluid stagnation. Figure 51 shows the static pressure profile at the wellbore-bottom to formation boundary. The highest pressure is found at the bottom center were the fluid jet impinges the formation. With radial distance the static pressure declines until it reaches a second stagnation point in the corners of the wellbore bottom. Based on these static pressure profiles it becomes clear that any narrow flow passage for the mud in the wellbore in conjunction with an open formation boundary provides a potential for formation fluid entrance. A reduction in flow cross section

can be a matter of wellbore design but also be due to clogging. Shutting in a well helps to reestablish a known pressure situation i.e. hydrostatic pressure.

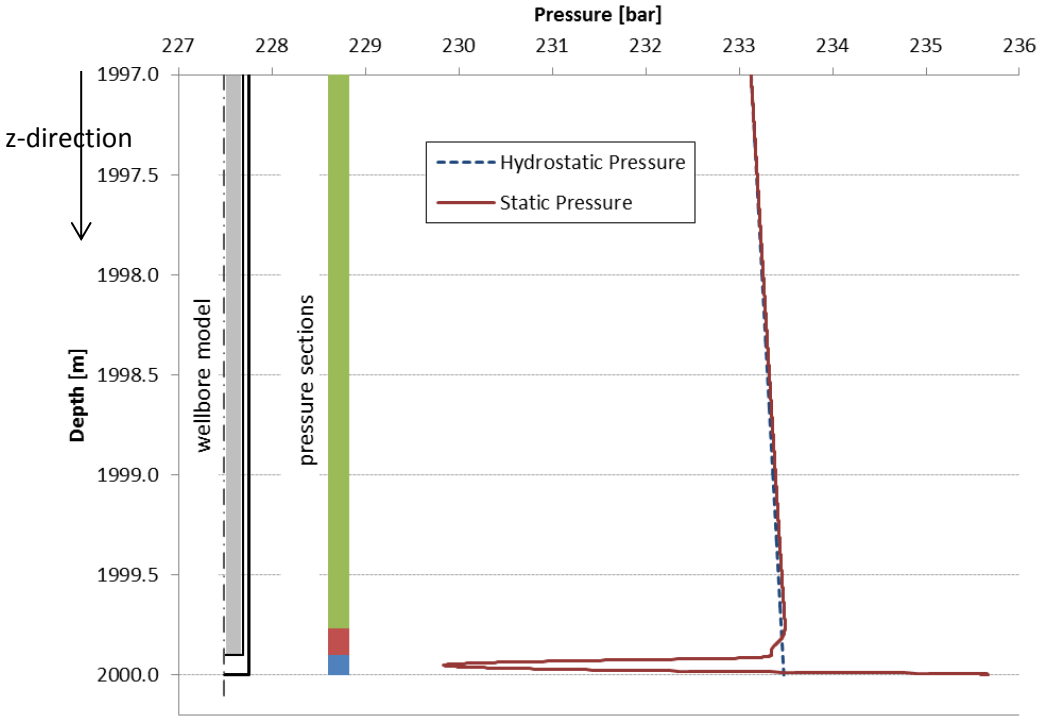


**Figure 50: Static Pressure Profile along Lateral Boundary, during Mud Circulation**

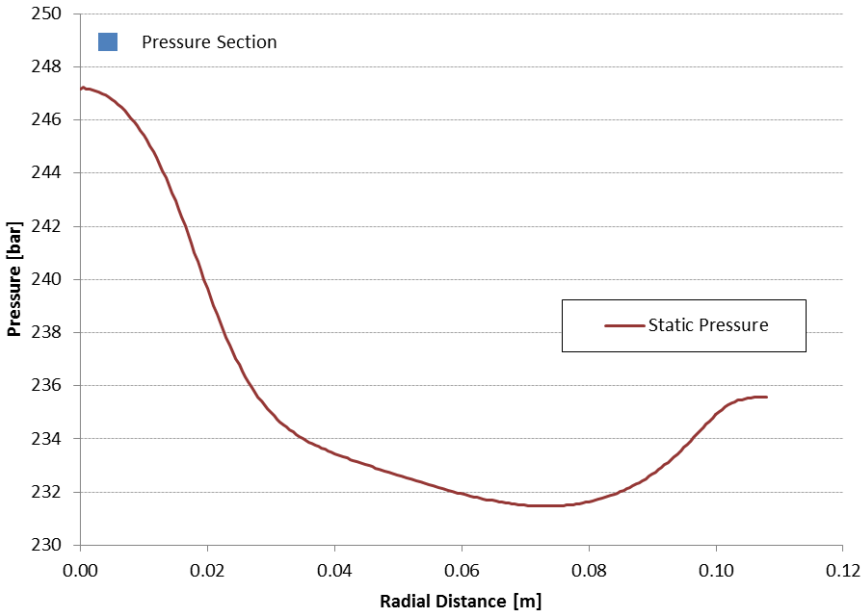


**Figure 51: Static Pressure Profile along Bottom-Hole Boundary, during Mud Circulation**

When looking at the pressure situation during mud circulation, we can classify three distinct pressure sections along the wellbore model boundary. These sections are illustrated in Figure 50 in green, red and blue and are described below.

The ***wellbore bottom*** or drill bit area (indicated in blue), defined as the volume below the annular channel. In this section the drill bit itself is located. Although the drill bit is not explicitly modeled in the model it is clear that the high velocity of the drilling mud leaving the drill bit nozzles and the limited space left between drill bit and formation is resulting in a highly fluctuating static pressure profile along the boundary. Depending on the angle of flow impact and velocity there are high pressure stagnation points and sections of low static pressure.

The ***transition zone,*** characterized by strong entry effects (indicated in red). This section is located at the beginning of the annular channel right above the drill bit. At this entry point of the drilling mud into the wellbore annulus we can see strong entry effects due to the change in geometry. The fluid path lines are strongly deflected and a pressure drop can be seen at the formation-wellbore boundary.

The ***annular channel*** above the transition zone, indicated in green. In this section a stable and continuous flow field over the whole annular cross section has established. No effects from the fluid entry point can be seen. The static pressure at the wellbore boundary shows a gradual profile dominated by the hydrostatic pressure. The pressure situation in this section corresponds to what is commonly expected in wellbore analysis. The flow has become unidirectional and can be computed based on the Hagen-Poiseuille equation.

To better illustrate the conditions at wellbore bottom, Figure 52 to Figure 54 show a zoomed in view of the static pressure distribution and velocity field. In the first image the motion of the fluid is illustrated with pathlines to better illustrate the evolving fluid vortices. The pressure scale is clipped to a range of 233 to 234 bars. A recirculation zone can be identified right at the beginning of the annulus. This vortex is a consequence of the deflected entry of the mud stream into the annulus caused by drill bit rotation. As the velocity vectors are indicating fluid is actually flowing backwards along the outer boundary. This vortex can be of special interest regarding phase mixing. Another stagnation point can be seen where the mud stream hits the drill pipe. Of course the shown flow field is a consequence of model configuration. But whatever drill bit configuration is used there will always be strong entry effects until the mud adopts a velocity profile aligned with the annulus.

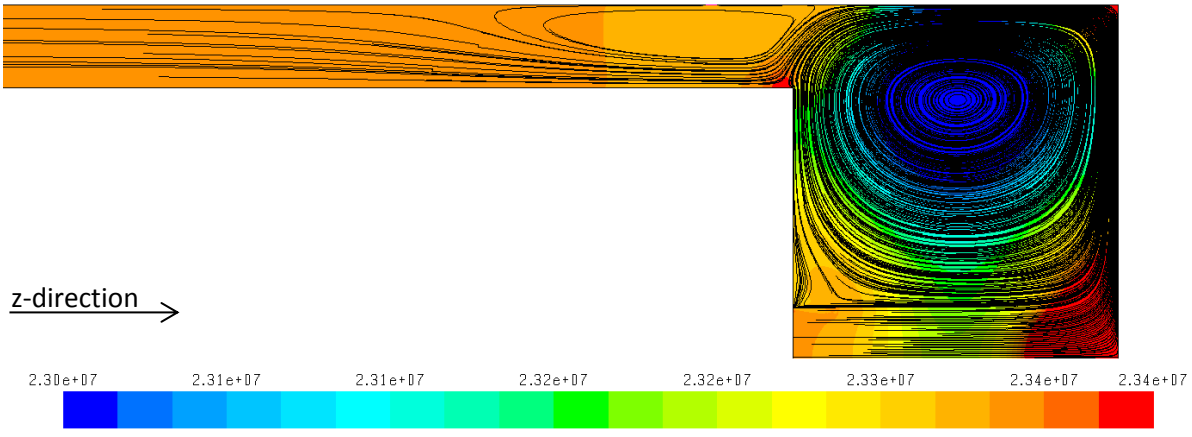


**Figure 52: Static Pressure [Pa] and Flow Pathlines**

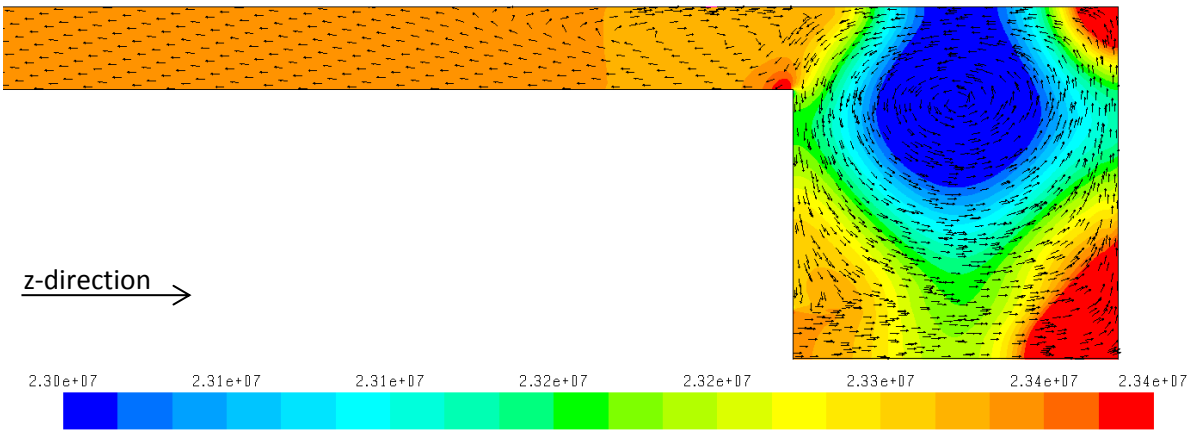


**Figure 53: Static Pressure [Pa] and Velocity Vectors**

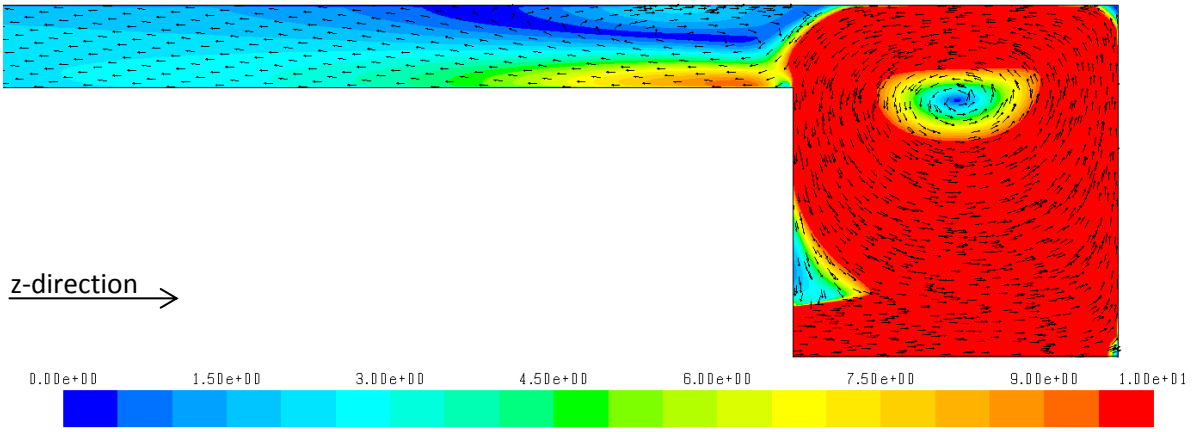


**Figure 54: Velocity Magnitude [m/s]**

The bottom-hole and transition zone represent the locations with the lowest static pressure counteracting the formation pore pressure. In case the pressure situation becomes underbalanced, the pressure gradient between formation and wellbore will be largest at these zones making them the most probable spots for formation fluid inflow, according to the current configuration.

For the simulation of the gas-kick the flow in the wellbore model is first calculated based on mere mud circulation to approach steady state conditions. This solution provides the initial condition before the kick gas is introduced. Several geometric scenarios for the gas-kick entry are investigated and illustrated in the result section of this thesis. For most simulation cases the boundary condition for the gas inlet is a constant pressure boundary. This boundary condition is realistic on the short time, since the pressure in the reservoir will not be affected by the gas escaping into the wellbore. There are also a few simulation cases where the gas is assumed to enter at a constant mass flow rate. The mass flow boundary condition basically skips the transient onset of gas inflow and reflects an uncontrolled kick situation.

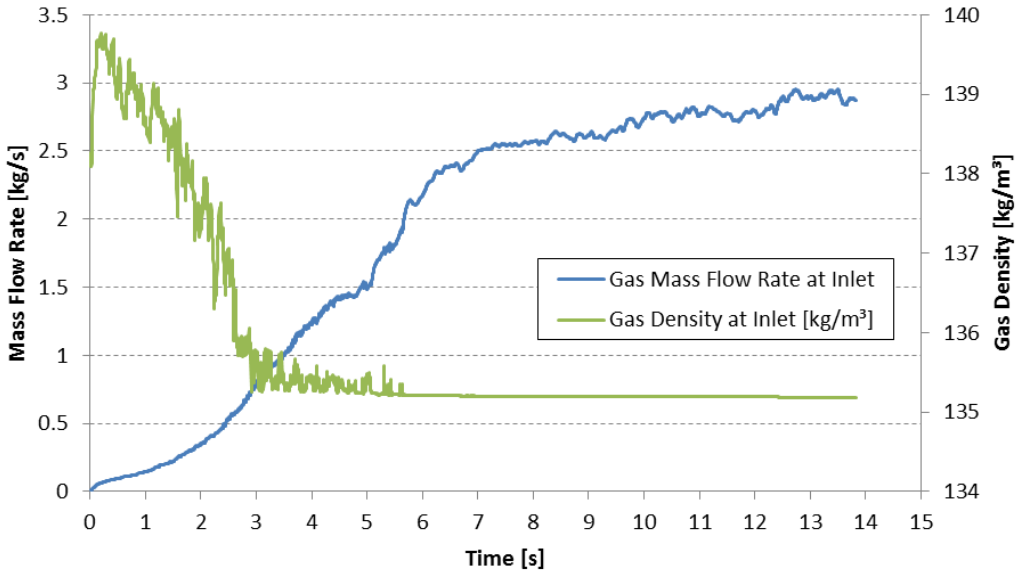


**Figure 55: Gas Inflow at Inlet Boundary**

The pressure boundary at the gas inlet replicates the real conditions better. It is characterized by a slow onset and subsequent increase in gas inflow until the pressure situation stabilizes and the gas flow rate becomes constant. Figure 55 shows the evolution of the gas inflow at a pressure boundary. Pressure situations where mud loss occurs can be well modeled with this boundary condition. A constant mass flow at the gas inlet boundary does not correspond to real conditions but helps to "speed up" simulation and focus on phase mixing with steady components; effects like mud loss of course cannot be covered.

The location of the gas entry point has a large influence on the flow situation, as can be deduced from the pressure profile shown in Figure 50. Basically the gas can enter through vugs, fractures, or pores in the open hole section, either laterally or at the bottom of the hole. Different gas entry scenarios are investigated and presented in the results section of this thesis. All gas-kick scenarios have in common that they occur immediately when the drill bit is advancing the suspected formation. The modeled gas inlets are therefore located in the direct vicinity of the drill bit.

The kick gas is modelled as a fictitious ideal gas with the basic material properties taken from Methane. As can be seen from Table 7, the material properties between Methane and Hydrogen Sulfide divert most regarding their specific weight. Hydrogen sulfide is about twice as heavy as Methane. Basically a sour gas influx will be a mixture of some hydrocarbon gas and a certain percentage of hydrogen sulphide. Due to the unknown composition of the gas it was decided to use a single phase gas instead of a gas mixture and the properties of Methane seemed most likely to replicate the gas behaviour.

**Table 7: Gas Properties**

| | **Methane, $CH_4$** | **Hydrogen Sulfide, $H_2S$** | |
|---|---|---|---|
| Thermal Conductivity | 0.0332 | 0.0134 | W/mK |
| Standard State Enthalpy | -7.49e+7 | -2.05e7 | J/kgmol |

| | | | |
|---|---|---|---|
| Molecular Weight | 16.04 | 34.08 | kg/kgmol |
| Specific Heat, cp | 2222 | 2222 | J/kgK |
| Viscosity | 1.087e-5 | 1.2e-5 | kg/ms |
| Reference Temperature | 298 | | K |

## Modeling of Gas Dissolution

In view of the fact that gas dissolution in drilling mud systems is an essential sub-process initiating corrosion, developing an understanding on the conditions enhancing or retarding mass transfer for this process is critical. In order to apply the concept of mass transfer rate calculation to the situation of gas influx in a wellbore, the mass transfer coefficient is a crucial parameter that needs to be chosen appropriately to reflect the unsteady flow situation of a kick event. The flow situation during a kick in the near drill bit section is dominated by the sudden inflow of formation fluid and expected to cause rapid mixing of the drilling mud and kick gas thereby enhancing the gas-liquid mass transfer.

Within the computational model the process of gas dissolution and release is modeled as mass transfer interaction between the gas and the liquid phase. Modeling mass transfer with the CFD solver FLUENT requires the input of a mass transfer rate per unit volume as interaction parameter between two phases. This can be done by either specifying a constant value, or selecting one of the built in models for mass transfer, or by defining a user defined function (UDF) for the computation of the mass transfer rate. In this work the latter approach has been chosen. With the means of a user defined function the volumetric mass transfer rate for each computational cell is calculated and updated at every time step. Based on the computed mass transfer rate FLUENT then adds contributions to the mass, species, and energy equations.

As mentioned earlier in this work the mass transfer rate can be defined as

$$\frac{dm}{dt} = kMA(C_S - C_0)$$

where

| | |
|---|---|
| m | mass [kg] |
| k | mass transfer coefficient [m/s] |
| M | molecular weight of gas [kg/mole] |
| A | interface area [m²] |
| $C_S$ | gas solubility [mole/m³] |
| $C_0$ | concentration of dissolved gas [mole/m³] |

Precise knowledge of the gas-liquid interface area is needed for calculation of the mass transfer rate. The size of the interface area has probably a stronger influence on the computed mass transfer rate than the selection of the mass transfer coefficient, especially in dispersed flow. The problem with the interface area is that it can neither be properly measured experimentally nor can it be exactly determined within a CFD simulation.

Dividing the above definition with the cell volume provides the requested mass transfer rate $\dot{m}$ input for the simulation.

$$\dot{m}_{gl} = kM\frac{A}{V}(C_S - C_0)$$

$\dot{m}_{gl}$ mass transfer rate, from gas to liquid phase [kg/m³s]

Based on this equation the cell based phase interface area per volume is needed. For this task a user defined function was set up and the computed interface area was stored in a user defined memory. Figure 56 shows a typical contour plot of phase distribution in the lower third of the wellbore model, the mud is indicated in black and the gas in white. The calculated interface area per volume is shown in Figure 57.

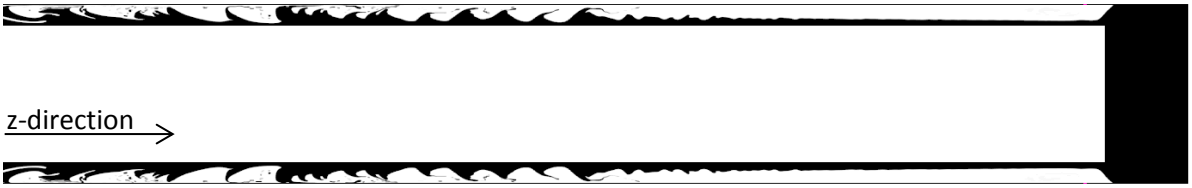


**Figure 56: Phase Distribution**

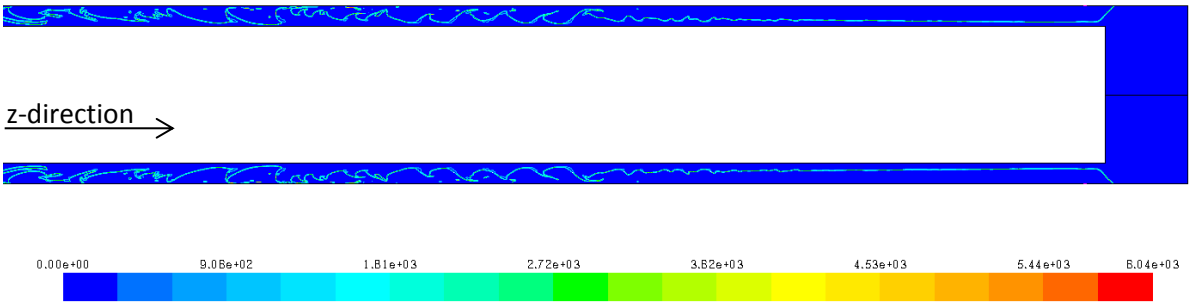


**Figure 57: Computed Interface Area per Volume [m²/m³]**

However difficulties arose when trying to update the computed interface area per cell with each time step. Unfortunately no straightforward solution was found to continuously update this value due to peculiarities of the simulation tool. An alternative approach was found by replacing the specific interface area $\frac{A}{V}$ with a term containing the gradient of the phase indicator function. This term basically represents the interface area density and is defined for the asymmetrical case as

$$\frac{A}{V} \propto VOF_{grad} = \sqrt{\left(\frac{df}{dx}\right)^2 + \left(\frac{df}{dy}\right)^2}$$

$VOF_{grad}$ volume fraction gradient
f phase indicator function

This term can easily be calculated and continuously updated with means of a user defined function. Figure 58 shows a contour plot of volume fraction gradient term that is consequently used to compute the mass transfer rate. It can be seen that the interface is captured quite well and that there is a good correlation with the specific interface area plot.

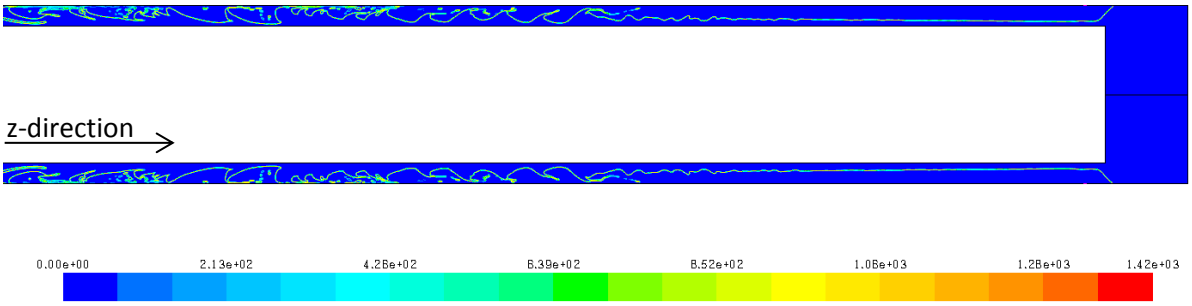


**Figure 58: Contours of Volume Fraction Gradient [$m^{-1}$]**

The computed volume fraction gradient is generally lower than the computed specific interface area shown in Figure 57. The values differ by a factor ~2.5, probably originating from cell geometry. To fit the volume fraction gradient term to the specific interface area proportionality constant is introduced.

$$\frac{A}{V} = 2.5\, VOF_{grad}$$

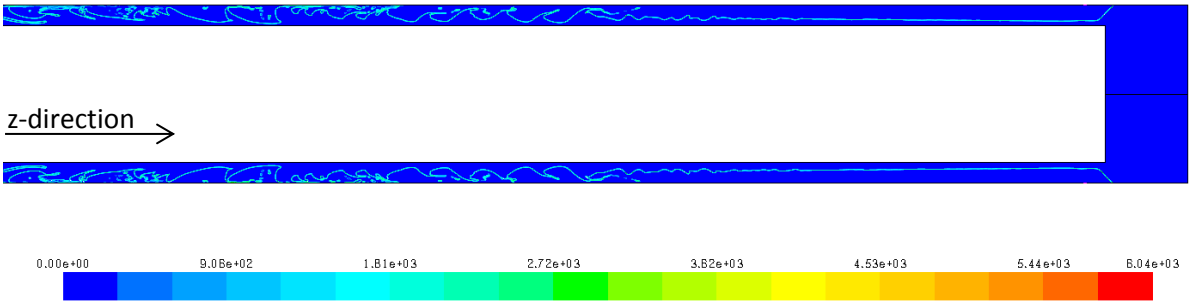


**Figure 59: Contours of Volume Fraction Gradient Times Proportionality Constant [$m^{-1}$]**

The mass transfer coefficient k needed for the computation of the volumetric mass transfer rate is calculated using a Sherwood correlation. As mentioned earlier Sherwood correlations, used to define mass transfer coefficients, are describing the mass transfer process of an overall process. Nevertheless calculation of mass transfer coefficients for use in a numerical model can be done with the help of a Sherwood correlation, if the correlation is based on local parameters utilizing the detailed information on the flow field provided by the CFD simulation. This approach leads to local mass transfer coefficients feeding the computation of a local mass transfer rates. Multiplication of local mass transfer coefficient times the local interfacial area and integration throughout the model domain will give the overall volumetric mass transfer coefficient of the system. The mass transfer coefficient used in a CFD simulation is influenced by the degree of the model's grid resolution, and consequently to what extent the mass transfer coefficient has to incorporate missing information on the interface area. A high grid resolution provides more detailed information on the phase interface and its morphology whereas a coarse grid resolution underestimates the phase interface area and its shape effect on the mass transfer process. This difficulty is often addressed by combining mass transfer coefficient and interface area to a volumetric mass transfer coefficient, which is also easier to compare with experimentally obtained data.

The following Sherwood correlation, taken from an experimental correlation for free bubble rise (Brennen, 2005), seemed appropriate for the simulation task at hand:

$$Sh = \frac{kd}{D} = 0.31\left(\frac{d^3 g\Delta\rho/\rho}{\nu^2}\right)^{\frac{1}{3}}\left(\frac{\nu}{D}\right)^{\frac{1}{3}}$$

$$k = 0.31\left(\frac{D^2 g\Delta\rho}{\mu}\right)^{\frac{1}{3}}$$

| | |
|---|---|
| D | diffusion coefficient |
| Δρ | gas liquid density ratio |
| ν | kinematic viscosity of liquid |
| μ | dynamic viscosity of liquid |
| ρ | liquid density |

This Sherwood correlation is implemented within a user defined function for computation and continuous update of cell based mass transfer coefficients. The viscosity variable in the equation is not constant due to the non-Newtonian fluid rheology. A contour plot of dynamic mud viscosity is shown in Figure 60. In case of Newtonian mud rheology the resulting mass transfer coefficient would be nearly constant except for variations in gas density, as shown in Figure 61.

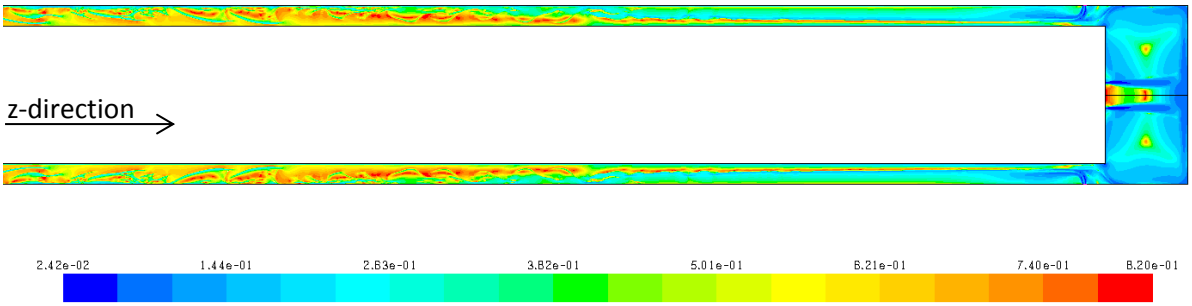


**Figure 60: Dynamic Mud Viscosity [Pa·s]**

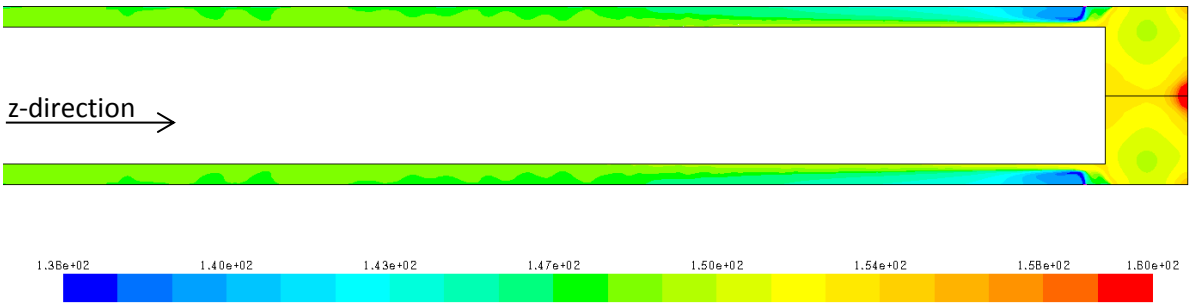


**Figure 61: Gas Density [kg/m³]**

Due to the rheological behavior of the fluid the viscosity is smallest in areas of large strain, which are present at the walls and the phase interface. According to the Sherwood correlation, a decrease in viscosity results in an increase in mass transfer. The following sequence of detailed images illustrates this relationship.

**Figure 62: Phase Distribution, Mud [black], Gas [white]**

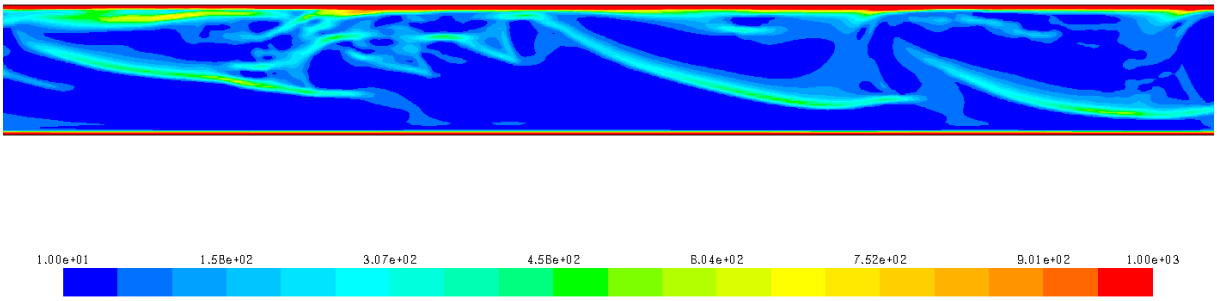


**Figure 63: Strain Rate [$s^{-1}$]**

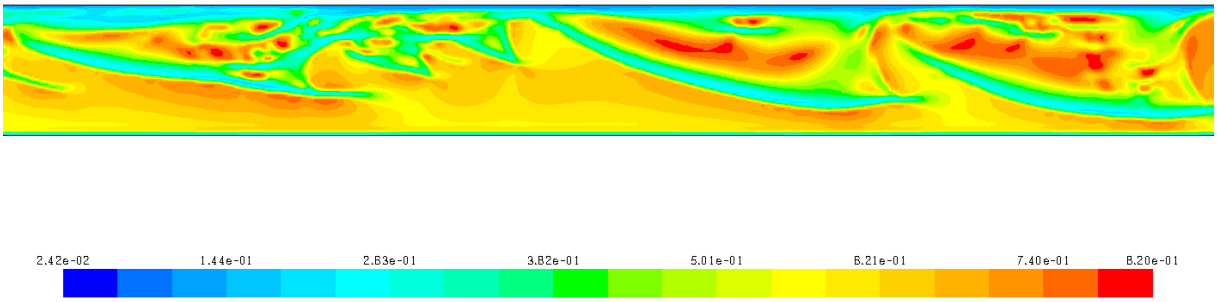


**Figure 64: Mud Viscosity [Pa·s]**

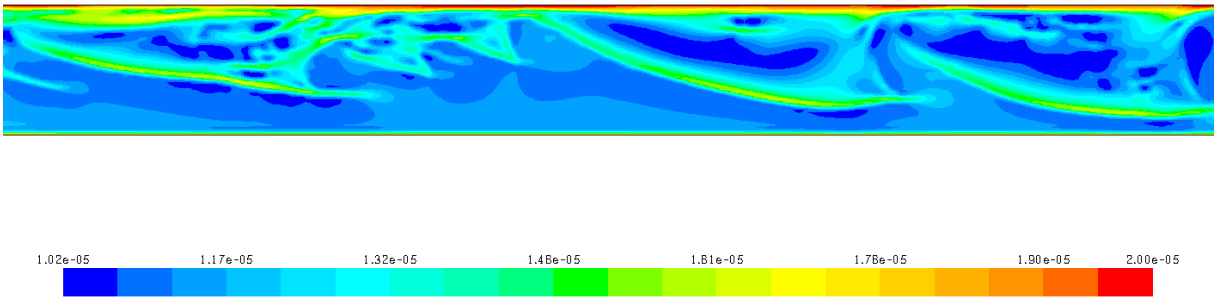


**Figure 65: Mass Transfer Coefficient [m/s]**

The diffusion coefficient basically depends on temperature, liquid viscosity, and molecule radius. Since diffusion is not playing a dominant role in the event of a gas-kick, a constant diffusion coefficient of 1.7e-9 m²/s is applied in the current model.

The computed mass transfer coefficients based on the above Sherwood correlation are shown in Figure 66. As already mentioned the spatial variation of mass transfer coefficient is mainly a function of the molecular viscosity used for the computation. The highest values can be found at the gas jet entry, along the phase interface, and in the drill bit area, see also the phase distribution shown in Figure 56.

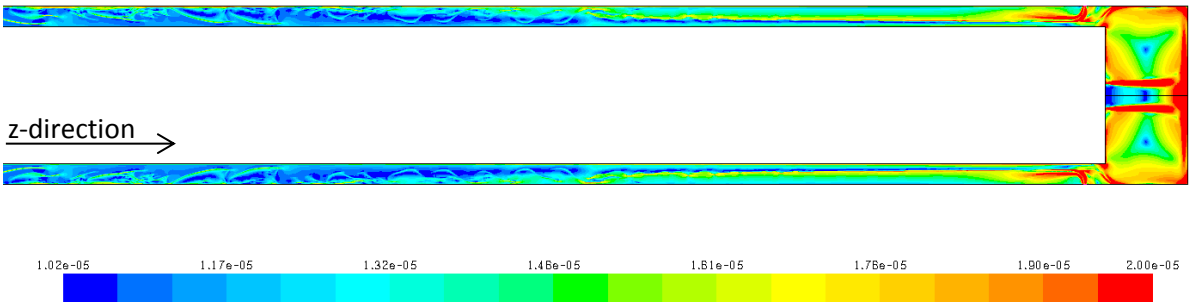


**Figure 66: Mass Transfer Coefficient [m/s], based on Sherwood Correlation**

For comparison reasons the mass transfer coefficient based on the surface renewal model of Kataoka and Miyauchi (1969), taking into account the turbulent dissipation rate ε, is shown in Figure 67. The underlying equation is defined as

$$k = 0.5\left(\frac{\varepsilon}{\nu}\right)^{\frac{1}{4}} D^{\frac{1}{2}}$$

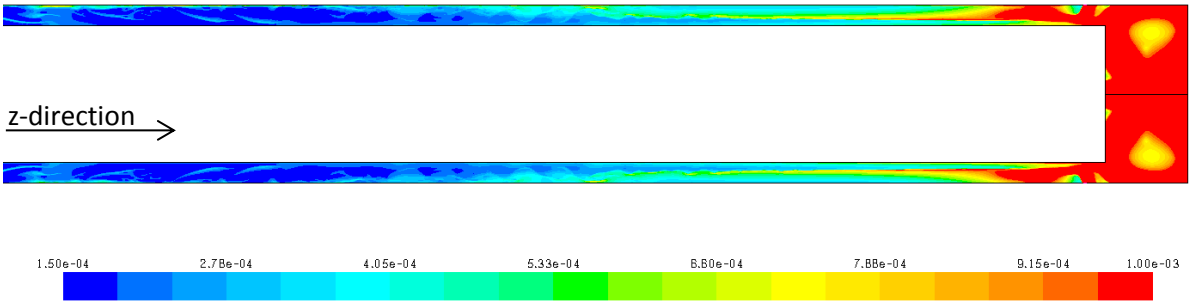


**Figure 67: Mass Transfer Coefficient [m/s], based on Kataoka and Miyauchi (1969)**

The mass transfer coefficients computed based on the Kataoka and Miyauchi (1969) model are 10 to 20 times higher and show a much wider range compared to the Sherwood correlation based values. The turbulence based model shows generally high values in the drill bit area and values are dropping quickly along the annulus, where the values show a similar spatial distribution like the Sherwood based values. The Sherwood correlation based values are locally prominent at the phase interface. The shear thinning behavior of the mud is basically favoring mass transfer. In the Kataoka and Miyauchi model this effect due to viscosity is overlapped with the contribution of ε wherever high turbulent dissipation occurs.

After having discussed the definition of the interface area term and the mass transfer coefficient, specification of molecular weight and gas solubility are left to complete the computation of mass transfer rate. The molecular weight of hydrogen sulfide amounts 34.08 g/mol. Gas solubility is calculated based on a fit approximating the results of the thermodynamic model for $H_2S$ solubility in pure water of Duan et al. (2007). The fit is intentionally overestimating the model results, since it is assumed that $H_2S$ will be more soluble in water based mud compared to pure water. This approximation seems to be a reasonable approach in view of the fact that no experimental data or model for $H_2S$ solubility

in water based mud could be found. The calculation of gas solubility is implemented via a user defined function and computed values are illustrated in Figure 68.

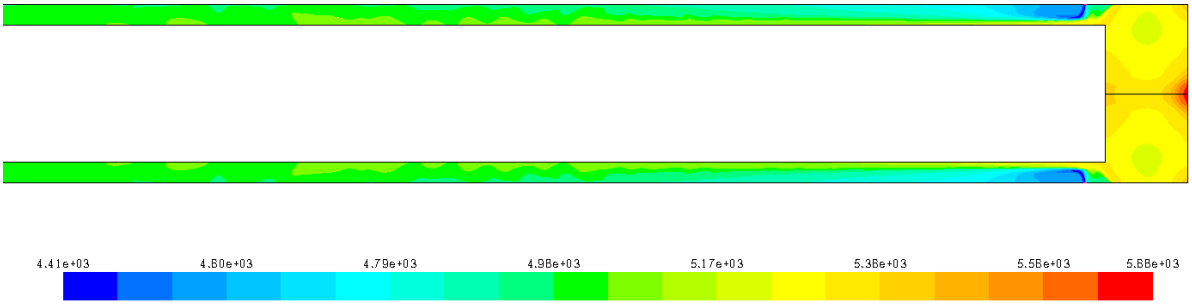


**Figure 68: Gas Solubility [mol/m³]**

The gas dissolved in the mud is assumed to remain molecular; no dissociation stages of hydrogen sulfide in the aqueous mud are covered. This assumption is valid for pH values below 6. At higher pH values $H_2S$ tends to reversibly dissociate in two stages depending on pH. To account for a change in mud properties due to dissolved gas, the mud is modeled as a mixture and the properties are updated based on a mixing law. In the current simulation cases the amount of dissolved gas is so small that the change in mud properties is negligible.

The difference between gas solubility and dissolved gas provides the last term needed for the computation of mass transfer rate. A typical contour plot of mass transfer rate is shown in Figure 69.

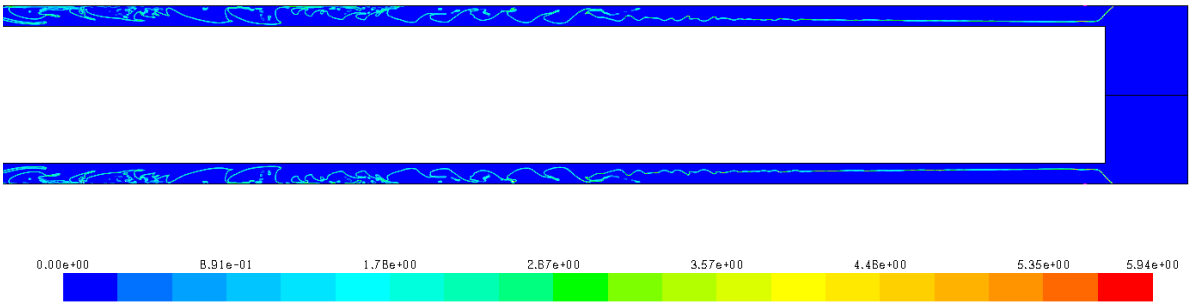


**Figure 69: Mass Transfer Rate [kg/m³s]**

Apart from calculation of volumetric mass transfer rates for gas dissolution, the user defined function constantly evaluates the conditions whether gas may come out of solution. Based on the local solubility gas is allowed to escape from solution when the local dissolved gas concentration exceeds this value. The release rate is computed similarly like the dissolution rate, using the reciprocal of the characteristic cell length l instead of the interface area density.

$$\dot{m}_{lg} = -KM\frac{1}{l}(C_0 - C_S)$$

$\dot{m}_{lg}$ mass transfer rate, from liquid to gas phase [kg/m³s]

# 6. Results and Discussion

This section of the thesis is structured into two parts. The first part discusses methods of data analysis and interpretation of two phase flow. In the second part results of different kick scenarios are presented.

## *Quantification of Two Phase Flow*

When setting up a simulation case for a multiphase flow problem, apart from considerations regarding the model setup along with boundary and initial conditions, one has to decide on how results can be evaluated, what quantities are characteristic and where and how they should be observed. Especially for a transient simulation a clear understanding of the flow problem in advance is needed in order to specify the proper quantities for monitoring during the course of computation.

Historically the most common parameters used in the 1-dimensional analysis of two-phase flow are:

- ***Void fraction or liquid holdup***
  Prediction of the void fraction is indispensable for the analysis of two-phase flow. It is the dominant parameter for processes involving mass transfer and chemical reactions.

- ***Superficial phase velocity***
  It is defined as the volume flux divided by the total cross-sectional area of the tube and often used as parameter in flow pattern maps.

- ***Slip ratio $U_g/U_l$***
  Originating from the drift flux modeling approach the velocity ratio between the gas and liquid phase is often used to characterize two-phase flow.

With the extensive data available from a transient CFD simulation the list of characteristic flow parameters may be extended by parameters reflecting the flow variations in time and space. Similar to common evaluation practice of unsteady flow experiments it appears equally adequate for unsteady flow simulations to measure the fluctuating flow quantities at representative locations of the modeled domain. These variations are best illustrated by the means of histograms or distributions and corresponding statistical parameters. Some parameters like for instance the phase interface area cannot be measured directly but instead only interpreted based on volume fraction information of the flow field. Additionally, integral parameters obtained on representative surfaces, cross sections, and volumes complete the list of result parameters. Using such techniques helps to summarize the amount of data available from a CFD simulation. This is necessary since a mere visual inspection is very difficult due to the elongated model geometry. The overall goal is to compress and extract key information that helps to ease the comparison between simulation cases.

## Velocity Data

In a CFD simulation using the volume of fluid method to model two phase flow the resulting velocity field is shared by both phases. However with the help of a high grid resolution it is possible to dedicate mixture velocity to a single phase in cells fully occupied with one fluid. Another useful method to characterize the flow based on velocity data is to look at the spatial variations of mixture velocity within the flow channel. Therefore histograms of axial and radial velocity components are used. Using time averaged mean velocity values the histogram can be seen as an estimate of the probability distribution of axial velocity. Time averaging can be done after the flow has become stable, indicated by the mass balance at the model boundaries.

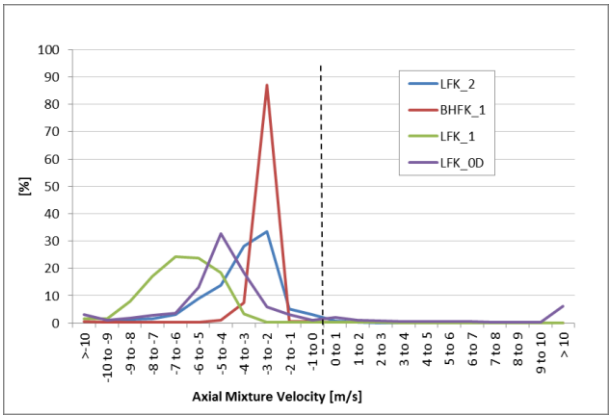


**Figure 70: Histogram of Axial Mixture Velocity in the Annular Channel**

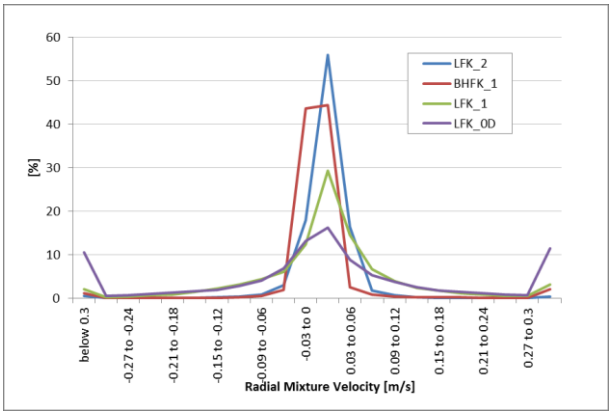


**Figure 71: Histogram of Radial Mixture Velocity in the Annular Channel**

Figure 70 shows the histogram of axial velocity of four simulated kick scenarios. Negative velocity accounts for upward flow, any positive values indicate reverse flow in the annular channel. The series denoted LFK_1 shows the broadest range of axial velocities and BHFK_1 has the narrowest axial velocity distribution. The magnitude of radial fluid movement can be judged by the radial velocity distribution shown in Figure 71.

The broad axial velocity distribution of LFK_1 is a result of the following flow situation: Right after the location of gas inflow there is a clear phase separation and phase velocities differ by a factor of two. After a distance of 30 times the annular clearance the velocities of both phases have equalized and phases are still clearly separated. From there on the phase interface starts to deteriorate more and more and the gas phase accelerates. The phase interface changes from small ripples, to large waves that eventually break up and produce numerous fluid ligaments and droplets. With increasing distance from the gas inlet the velocity of the gas phase increases and the velocity of the mud phase decreases. No notable flow recirculation can be found in this case.

The narrowest axial velocity distribution belongs to the simulation case BHFK_1. In this case gas and mud show hardly any difference in axial velocity. The flow morphology has characteristics of both bubble flow and churn flow. Elongated fluid ligaments can be found

near the annular walls and larger bubbles travelling in the core of the annulus. The fluid ligaments are actually a wake of small gas bubbles smeared of from the periodic generation of Taylor bubbles at the entrance to the annular channel. The bubbles traveling in the core have a size of approximately a third of the annular clearance and show the typical tail-dented shape of Taylor bubbles. Due to the limited variation in axial velocity, the shape of the fluid structures stays nearly constant after a distance of 30 times the annular clearance. The rotational component in the flow is clearly indicated by the broader distribution of radial mixture velocities shown in Figure 71.

Simulation case LFK_2 shows similar behavior like LFK_1. Velocities are lower since the differential pressure applied at the gas inlet is about seven times smaller. The shape of the axial velocity distributions is comparable. However in LFK_2 not only the inner cylinder is rotated but also the whole annular channel is rotated. This setup was chosen to mimic the influence of near drill bit assembly like stabilizers that impose additional rotational drag compared to a smooth pipe. The annular rotation causes a narrow radial velocity distribution as can be seen in Figure 71, as the exchange between fluid layers is limited. As a consequence the shape of the phase interface is very smooth.

The other extreme of radial velocity distribution belongs to simulation case LFK_0D. Here strong radial momentum exchange between the phases occurs, resulting in a very complex phase distribution and increased phase interface area. The bubble flow regime of BHFK_1 shows limited radial fluid movement. It is the breakup of annular flow and its transformation into wispy annular, and slug/churn flow regime types that show the broadest radial velocity distribution. This may also explain why flow regimes like churn and slug show the highest fluid mechanical damage on pipe walls observed in experiments.

To summarize, the histograms of radial and axial velocities in the annular channel help to identify the existence of flow recirculation cells. The profiles show typical shapes according to flow regime. Thereby it is possible to identify flow patterns based on measureable parameters instead of visual inspection. The data has to be collected when the flow in the simulated channel section has stabilized. Consequently the illustrations provide no information on the temporal evolution of the flow.

The flow morphology i.e. phase distribution of the simulation cases discussed is illustrated in Figure 73 to Figure 76. Figure 72 shows the length of 30 times the annular clearance measured upwards from the annular entrance.

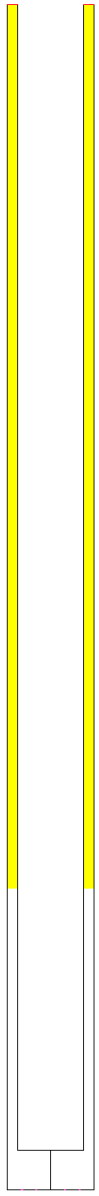

Figure 72

Figure 73: BHFK_1

Figure 74: LFK_0D

Figure 75: LFK_1

Figure 76: LFK_2

## Void fraction

Void fraction is often used as an indicator for the transition from bubbly flow to slug flow. For instance Taitel et al. (1980) suggest that for bubbles of uniform size in flowing in a pipe, the transition occurs when the gas void fraction reaches 0.25. Caetano et al. (1992) observed this transition at an average void fraction of 0.2 in a concentric annulus. They observed an even earlier transition at a void fraction of 0.15 for flow through a fully eccentric annulus. Apparently the gap size has a strong influence on the change from a bubbly to a slug flow pattern. It is the influence of the channel walls on the velocity profile of the flow that increases the collision rate of the gas bubbles leading to the formation of slugs.

An increase in gas flow rate destructs the initial slug flow resulting in a churning and oscillatory flow situation. Eventually at very high gas flow rates, the flow becomes annular with a liquid film on the walls and a gas continuum in the annular core. These changes will be illustrated via averaged void fraction profiles along the annulus in the next section of this work.

Another characteristic that is useful in classifying flow patterns is the level of intermittency in the volume fraction. Examples of strong intermittent flow patterns are slug flows and the occurrence of interfacial waves in separated flow. With the analysis of time series of dedicated flow quantities in the frequency domain information about flow fluctuations can be provided. For instance slug frequency can be obtained from the time series of void fraction. Furthermore geometric information on flow structures can be obtained with this technique. An example will be shown in the next section of this thesis.

Finally a histogram of void fraction is very helpful to evaluate whether the model's grid resolution is adequate to capture the two-phase flow morphology of the current setting. It serves as a measure of quality for the applied modeling approach. Figure 77 shows histograms of gas void fraction of selected simulation cases. Basically all simulation cases show a good phase separation and low smearing, indicating that the grid resolution is adequate to resolve the occurring flow structures. For case BHFK_1 the grid resolution is becoming critical to capture the small bubbles occurring in this simulation, but the overall coverage of the flow is still good.

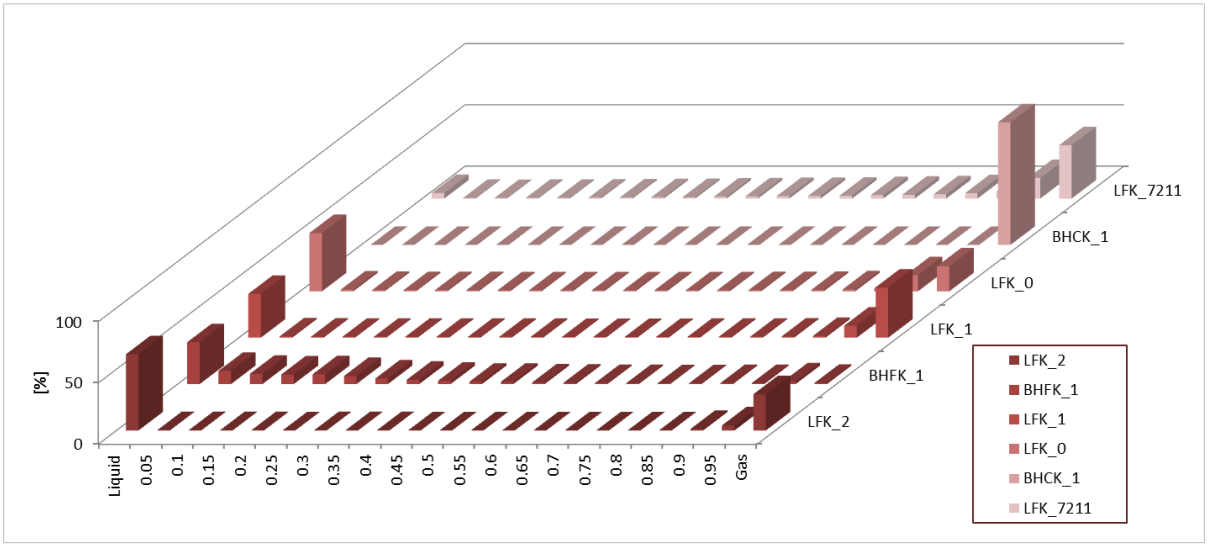


**Figure 77: Histograms of Gas Volume Fraction**

# *Simulated Kick Scenarios*

In this section selected simulation cases are presented and discussed.

The manifestation of a kick basically depends on the following parameters:

- Overall depth (pressure, temperature)
- Annular geometry (annular clearance)
- Drilling mud properties (density, rheology, mud type)
- Operational conditions (circulation, shut in)
- Location and configuration of kick entrance
- Differential pressure between the wellbore and the formation

With respect to this parameter list the first four parameters are kept constant in the presented simulation cases. The latter two parameters are varied and their influence will be shown. The boundary conditions for the simulation cases are chosen to reproduce steady-state flow regimes ranging from bubble flow to annular flow, classified as:

- Dispersed flow (bubble flow)
- Intermittent flow (churn flow)
- Separated flow (annular flow)

The positioning of the presented simulation cases is illustrated in the flow regime map of Caetano (1992) for concentric vertical annuli in Figure 78. Due to the constant mud flow rate applied to all simulation cases the values are aligned along one line.

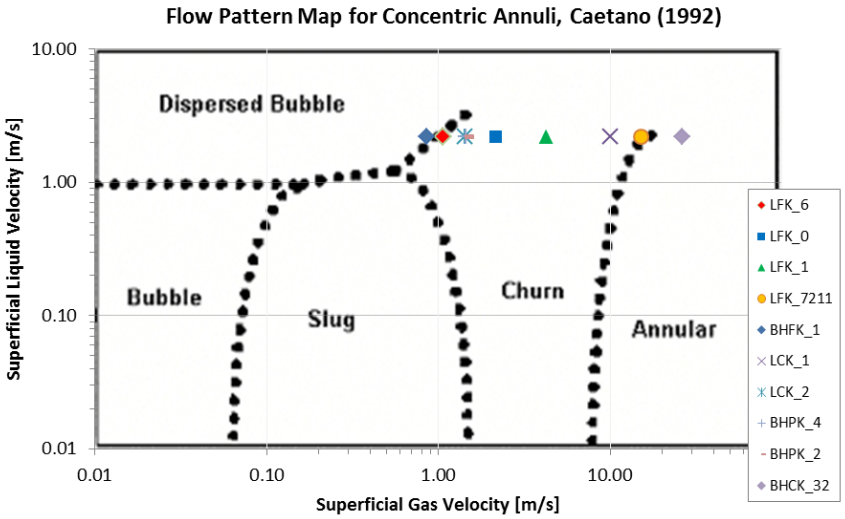


**Figure 78: Flow Regime Map Illustrating the Range of Simulation Cases**

The first group of simulation cases presented in this chapter is focusing on the location of kick entrance. The major parameters for each kick scenario are listed and a sketch is illustrating the inlet configuration of the kick gas. A detailed analysis of the occurring flow phenomena is given including the assessment of specific phase interface area and gas dissolution parameters. The second group of discussed simulation cases is investigating kick scenarios leading to a loss of mud circulation.

## Location of Kick Entrance

The location and size of the entry point where the gas is flowing into the wellbore was found to have a significant effect on the phase mixing and distribution. Therefore the results of four different kick scenarios will be discussed in this section. The scenarios differ in opening size and location, the gas inlet is either small to simulate a single fracture or large to mimic a cavern.

### *Lateral Kick Scenario – Single Fracture*

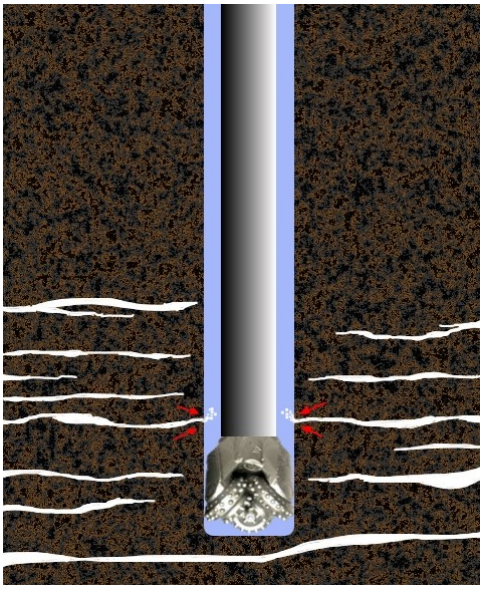

In this kick scenario a single fracture is considered with an opening size of 3 mm located 2.5 cm above the drill bit (the drill bit has a height of 10 cm), as illustrated in Figure 79. Four selected simulation cases are discussed. The main simulation parameters are listed in Table 8. In all setups the inner pipe and the drill bit section are rotated at a rate of 100 rpm. The positioning of the simulation cases with respect to flow regime classification according to Caetano (1992) is given in Figure 80. A detailed interpretation of flow regime changes during a gas-kick will be given at the end of this section.

**Figure 79: Kick Scenario with Single Lateral Fracture**

**Table 8: Lateral Fracture Kick Scenarios**

| Case | Gas Inlet Condition | Static Wellbore Pressure at Inlet | Δp at kick onset | Sup. Gas Velocity | Sup. Mud Velocity | Liquid Holdup |
|---|---|---|---|---|---|---|
| LFK_6 | 233.33 bar | 233.3 bar | 0.03 bar | 1.07 m/s | 2.19 m/s | 0.69 |
| LFK_0 | 233.6 bar | 233.3 bar | 0.3 bar | 2.17 m/s | 2.19 m/s | 0.48 |
| LFK_1 | 235.6 bar | 233.3 bar | 2.3 bar | 4.28 m/s | 2.19 m/s | 0.4 |
| LFK_7211 | 243.3 bar | 233.3 bar | 10 bar | 15.26 m/s | 2.19 m/s | 0.15 |

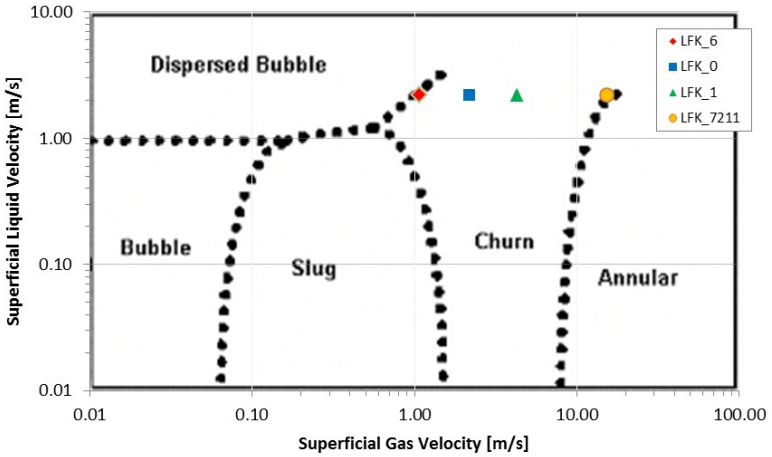


**Figure 80: Flow Pattern Map for Concentric Annuli, Caetano (1992)**

For all simulation cases the gas inflow is comparable to a jet impinging perpendicularly on the continuous mud flow in the annulus. The available cross sectional area for the mud passage is reduced dramatically causing an increase in mud velocity. This results in a configuration of a mud jet pointing upwards and laterally impinged by the gas jet.

Which one of two fluids is forming the dominant jet depends on the ratio of the driving pressure differential per fluid. The driving pressure differential for the gas is defined by formation pressure and wellbore pressure at the entry point, for the liquid it is the pressure gradient in the wellbore produced by the pump. In the CFD simulations the inflow of the drilling mud is specified as a constant mass flow rate at all times and the formation pressure is modeled by a constant inflow pressure boundary for the gas. Naturally the pressure in the wellbore will change due to the inflow of the gas and continuously alter the flow situation until both fluids are in balance.

A close-up view of the channel including the gas inlet is shown in Figure 81 to Figure 84. The images belong to simulation case LFK_1. The pressure situation before and during the gas-kick is illustrated, as well as the velocity field, kinetic energy and phase distribution. The intruding gas is forcing the mud to move as a thin film along the inner cylinder at increased speed. Immediately above and below the gas jet a zone of lower pressure is forming were gas is recirculating as indicated in Figure 102. The high inlet velocity of the gas jet is quickly dissipating and the mud jet is becoming the faster jet. After a certain distance the gas and mud velocities equalize and the phase interface is becoming smoother, after that the gas accelerates due to buoyancy and becomes the dominant jet. The phase distribution where the dominance of the jets is changing can be seen in Figure 85 and the corresponding velocity field is shown in Figure 86.

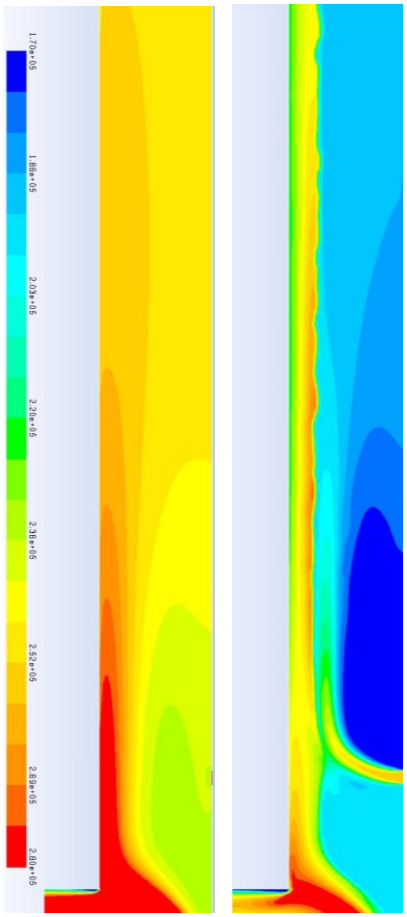

**Figure 81: Total Pressure, Mud Circulation (left), Gas-Kick (right)**

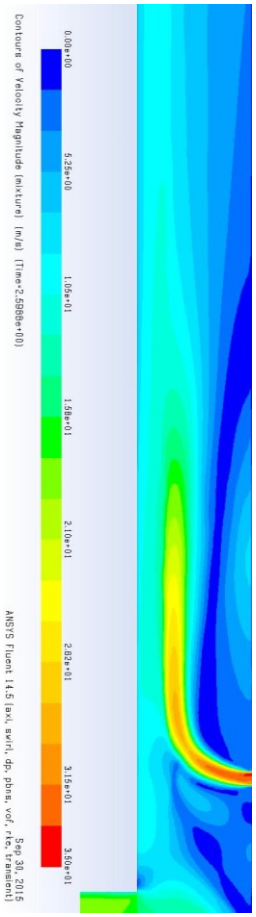

**Figure 82: Contours of Velocity Magnitude**

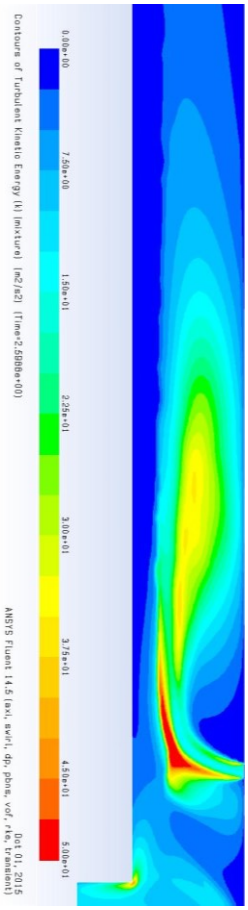

**Figure 83: Turbulent Kinetic Energy**

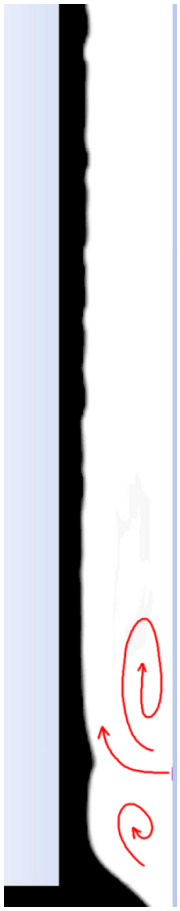

**Figure 84: Contours of Gas Volume Fraction**


**Figure 85: Phase Distribution, LFK_1**

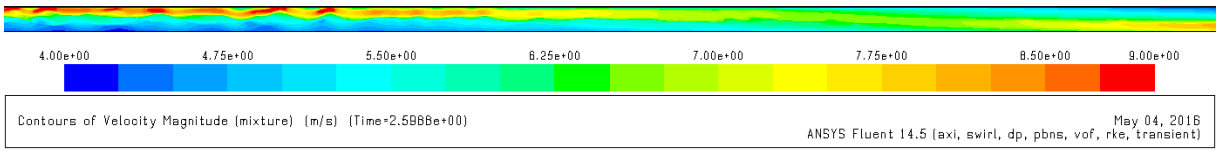


**Figure 86: Contours of Velocity Magnitude, LFK_1**

The evolution of the phase interface between the gas and the mud can be investigated in a similar manner like the breakup of a jet. Comparable mechanisms are taking place, however with restriction in space due to the confinement given by the channel geometry. For instance different breakup scenarios of a free liquid jet are characterized by Reynolds and Ohnesorge

number. In the present simulation cases gas with a certain momentum and buoyancy exists from a narrow fracture and intrudes into a mud stream with different characteristics. The breakup of the gas jet depends on several parameters, i.e. size of the fracture opening, density ratio of the fluids, ratio of surface tension force, viscous shear between the phases. The occurring phase instabilities can be well categorized with the help of the Weber number, Richardson number, and gas Reynolds number.

Therefore the list of dimensionless numbers in Table 9 was extended by the Richardson number. This number, defined as the ratio of potential to kinetic energy, helps to better characterize the shear induced instability. A high Richardson number indicates that the effect of buoyancy on interphase distortion is more pronounced than the effect due to phase inertia. The turbulences in the gas stream reflected by the gas Reynolds number are responsible for the onset of disturbances at the gas mud interface. A high Weber number indicates that viscous forces play a dominant role. For instance all three simulation cases show a highly distorted interface area but the driving mechanism for phase distortion is different.

For simulation case LFK_0 the superficial gas and mud velocity are almost equal. This case shows a highly transient flow situation and can be definitely classified as churn flow. The gas and mud phase seem to compete about the available annular space. The Weber number is a minimum and Richardson number is highest, superficial velocities are almost equal, so the generation of interface area is dominated by the difference in phase density. This is a typical example for a so-called Rayleigh-Taylor instability, where the lighter fluid is pushing the heavier fluid. Typical are the mushroom-like structures formed by the lighter phase.

In case LFK_1 the buoyancy force is still the dominant force but inertial forces are gaining increased influence, this can be seen by the occurrence of shear instabilities at the phase interface where velocity differences are large. This effect becomes even more pronounced in case LFK_7211. Which one of the jets is forming the dominant jet can be evaluated based on the shape of the interface distortion wave crests. The shear instability of coaxial jets, also called Kelvin-Helmholtz instability, begins with a wavy structure caused by the friction between the phases. The disturbance increases and waves become higher until they turn over the slower fluid, see Figure 87. The direction of the vortex structure indicates which one of the jets dominates the flow. During the course of simulations conducted it was frequently noted how a change in the direction of rotation of the vortices occurred. For instance the mud jet was dominant near the narrow passage where the gas jet is introduced, then a section followed with a rather flat phase interface indicating equal phase velocities until the gas jet eventually became dominant introducing a vortex structure at the phase interface.

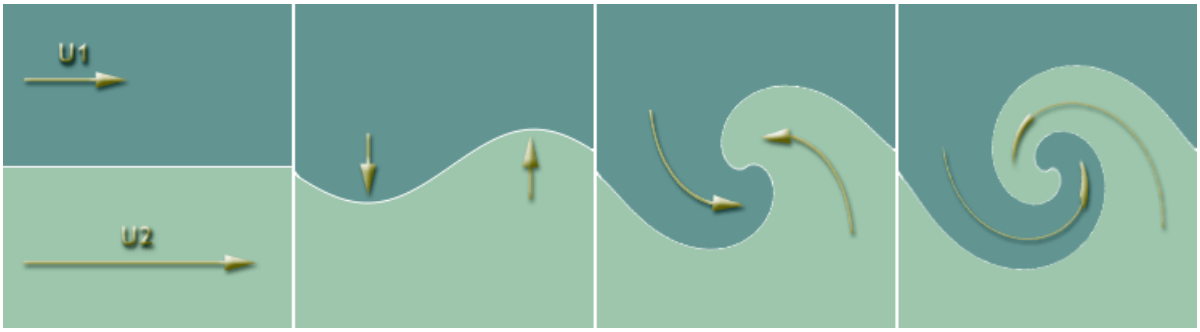


**Figure 87: Kelvin-Helmholtz Instability**

**Table 9: Dimensionless Numbers**

| | LFK_6 | LFK_0 | LFK_1 | LFK_7211 |
|---|---|---|---|---|
| $\dot{E}_{kin,g}$ | **70** | **582** | **4500** | **206720** |
| $\dot{E}_{kin,l}$ | 44,116 | 44,116 | 44,116 | 44,116 |
| $\dot{E}_{kin}$ ratio | 0.997 | 0.97 | 0.81 | 0.65 |
| $U_{S,mix}$ | **3.26** | **4.36** | **6.48** | **17.46** |
| $Re_{L,in}$ | 3,124 | 3,124 | 3,124 | 3,124 |
| $Re_{G,in}$ | **7,968,185** | **16,117,466** | **31,748,898** | **115,176,495** |
| $We$ | **763** | **0.47** | **2,641** | **103,266** |
| $Mo$ | 3.65 | 3.65 | 3.65 | 3.65 |
| $Eo$ | 134 | 134 | 134 | 133 |
| $Fr_{gas}$ | **6.9** | **9.3** | **13.8** | **37.2** |
| $Ri$ | **8,199** | **13,431,012** | **2,369** | **60** |

In the following a detailed analysis about the phase interface breakup for simulation case LFK_7211 is shown. The intention is to find means on how to quantify the phase interface distortion. The volumetric phase distribution along the well-bore model after the flow regime has stabilized is shown in Figure 88. It can be seen that the gas phase is more or less constantly occupying ~85 % of the available space. The slight variations of the data series provide hardly any information on the extent of interface distortion. To gain information about the interface between the phases, a closer look on individual segments of the flow geometry is suggested. Therefore several representative 10 cm long segments of the annular channel cm are presented in Table 10.

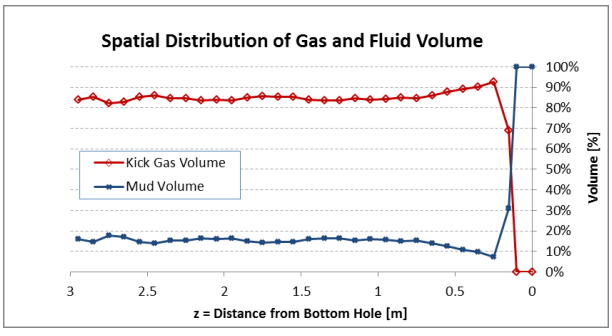


**Figure 88: Volumetric Phase Distribution, LFK_7211**

The table below depicts the phase distributions by contour plots on the left hand side and their volume distribution on the right hand side for each individual segment. The segment position is given in the first column of the table, with z measured positively upward from the wellbore bottom. In the contour plots the gas phase is indicated by a red color and the mud phase is indicated in blue, the phase interface is indicated by volume fractions colored according to the color bar in the legend. In order to quantify the contour plots shown on the left the volumes occupied by the individual phases are shown on the right. The horizontal axis shows the volume fractions, whereby a value of 1 represents mere gas and a volume fraction of 0 represents mere mud. The phase interface is made up by volume fractions between 0 and 1. The vertical axis lists the volume occupied by the respective volume fraction. Additionally the relative gas and mud volume as well as the relative single phase volume (grey box) and interface volume (white box) are given.

**Table 10: Analysis of Phase Volume Fractions at Representative Segments**

| | | |
|---|---|---|
| **zone 6.3**<br>Segment position: z = 0.2 – 0.3 m | 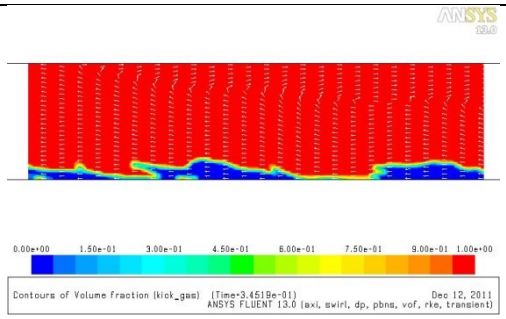 | 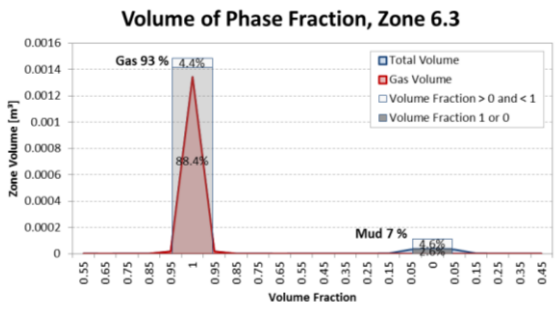 |
| **zone 6.0**<br>Segment position: z = 0.5 – 0.6 m | 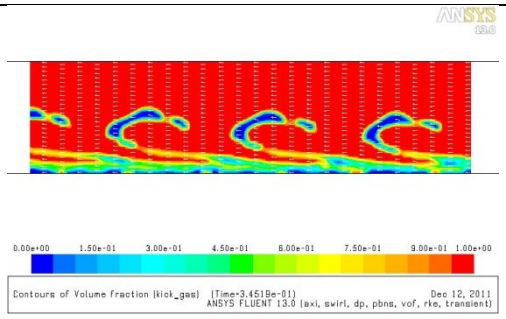 | 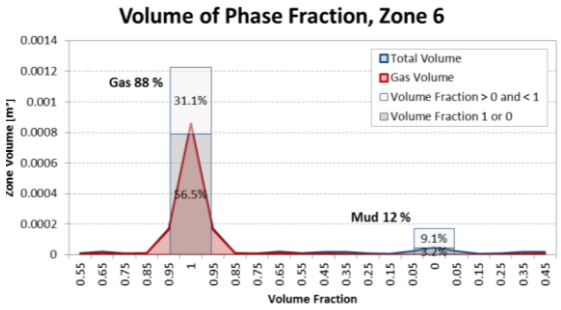 |
| **zone 5.5**<br>Segment position: z = 1 – 1.1 m | 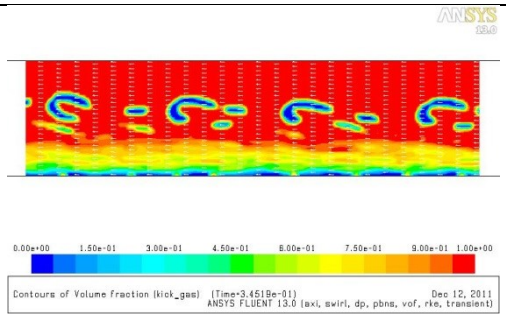 | 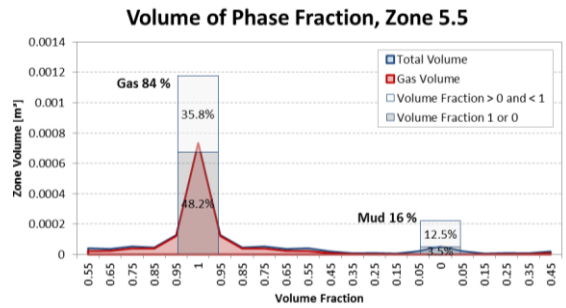 |

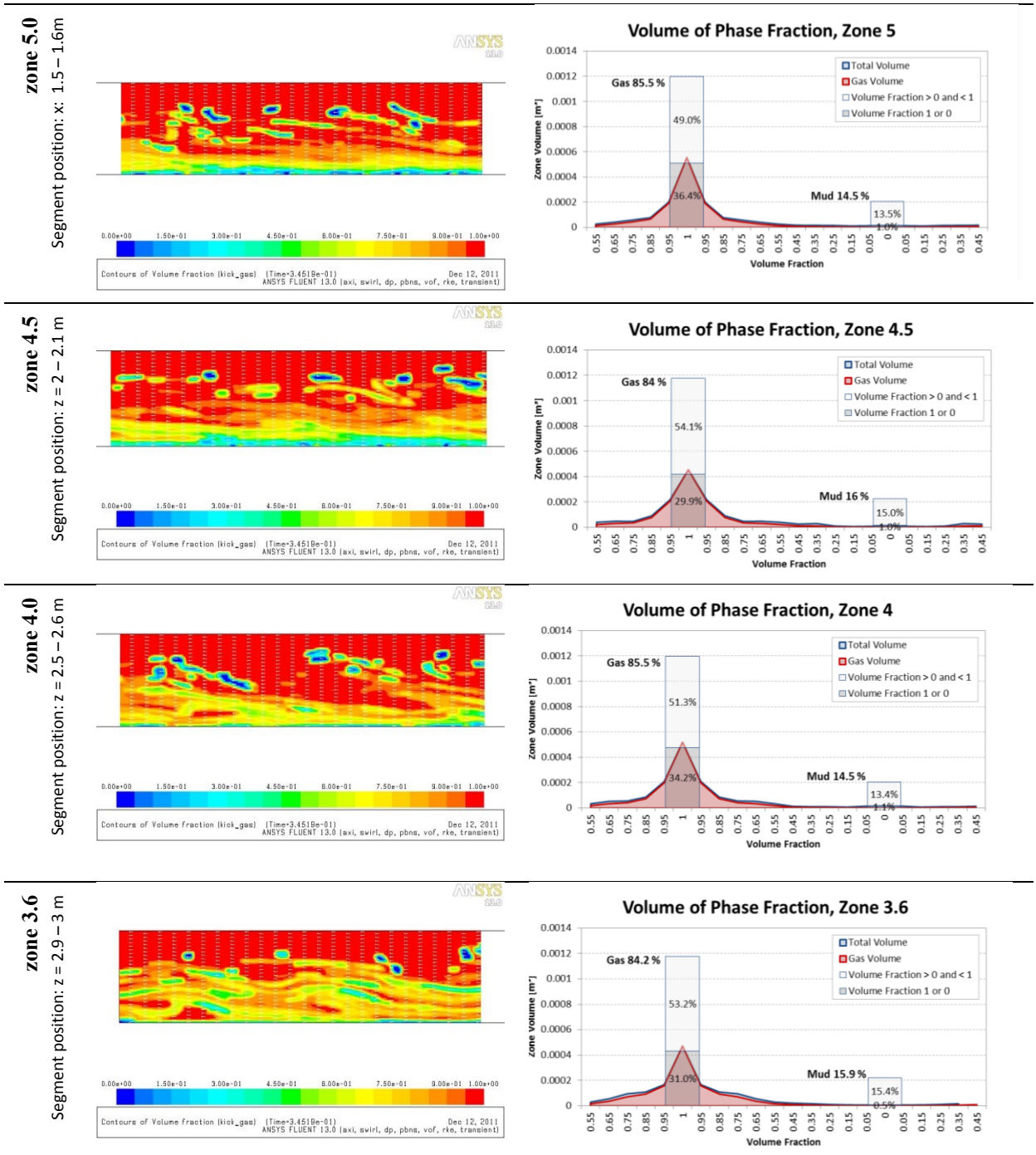


The gas is entering the annulus at z = 0.12 m thereby reducing the available cross sectional area for the mud passage and forcing it to travel upwards as a thin film along the inner pipe. The displaced mud accelerates from initially 5 m/s to a maximum speed of about 65 m/s, see Figure 89. The axial mixture velocity profiles shown are located at a radius of 0.084 m and 0.1016 m from the wellbore axis. The location of the profiles was picked to ensure the profiles are lying within either the gas or the mud phase. Thus the red line shows the fluid velocity where the presence of gas and the blue line shows the velocity profile where the presence of mud is predominant. The negative velocity peak of the red series represents the occurrence of a recirculation swirl just above the gas-kick inlet. High frequency fluctuations

in the profile are due to phase changes at these positions, so for instance the fluctuations in the mud velocity profile directly after the gas-kick inlet are caused by the wave geometry of the mud film travelling up the drill pipe. Disturbances start forming at the phase interface. The initially wavy structure deforms more and more, as a consequence of shear between the phases. Wave heights are increasing and begin to break up at the crests into smaller fluid ligaments. The direction of rotation of the fluid ligaments indicates the faster phase. Breakup of the liquid film is emphasized near the wall where axial shear is largest. Fluid ligaments and droplets near the core are less sheared and therefore larger in size. The width of the strong breakup and phase mixing zone near the drill pipe increases with distance from the wellbore bottom. The phase mixing zone induces turbulences and approaches further into the annular gap until a chaotic regime is eventually reached.

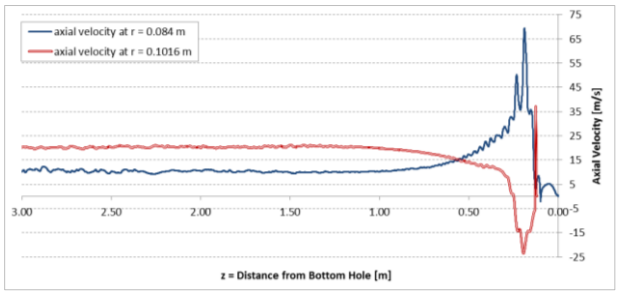


**Figure 89: Axial Velocity Profile, LFK_7211**

To illustrate the sharpness of the phase interface, standard deviations of the single phase volume fractions are computed. Therefore a volume fraction of 0.5 was chosen to distinguish between mud and gas phase. The basis for this calculation is a mean of 1 for the gas phase and a mean of 0 for the mud phase. Assuming the gas and mud phase fractions to be normally distributed the interval ±σ of the mean would contain 68.27% of the values.

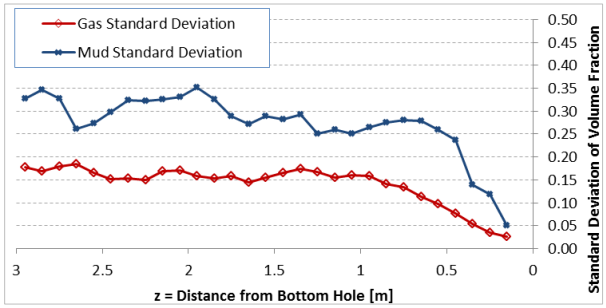


**Figure 90: Volume Fraction Standard Deviation**

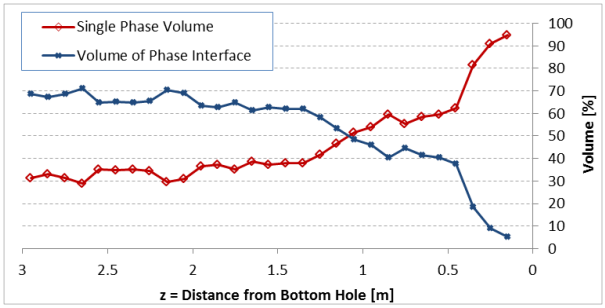


**Figure 91: Single Phase and Interface Volume**

Figure 90 illustrates the standard deviations of the gas and mud phase volume fractions along the wellbore. The standard deviations are computed for each 10 cm zone segment. Low values near the gas-kick entry at the wellbore bottom indicate a sharp phase interface and clear phase separation; whereas high values further upwards the annulus illustrate the phase breakup into very small droplets and bubbles. The computational grid resolution of 0.5 mm is not able to resolve these very small flow structures and hence the volume occupied by the phase interface increases. It should be noted that effects like numerical diffusion may also start to play a role

in these “smeared phase conditions”. Figure 91 provides information on how much volume is occupied by a distinct single phase, i.e. volume fractions of 1 or 0, and how much volume is occupied by the phase interface.

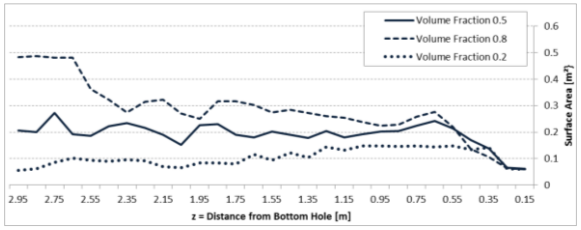


**Figure 92: Phase Interface Area**

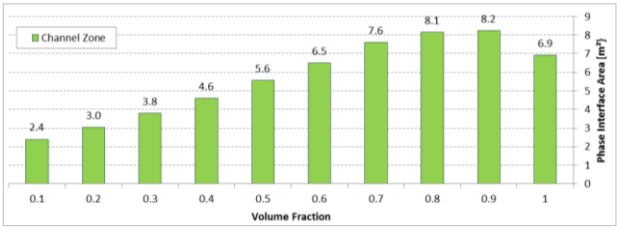


**Figure 93: Phase Interface Area based on VOF**

The interface surface area can be calculated based on a certain volume fraction that defines the border between the phases. This approach is appropriate when the interface is very sharp. However the more the phase interface gets smeared the more difficult it is to define a single volume fraction as the divider between the phases. Figure 92 shows the effect of increasing phase interface volume on computed surface area for three selected volume fractions. In flow domains where the interface is distinct the computed surface area should be independent on volume fraction. As the volume occupied by the phase interface increases the computed surface areas differ more widely. It can be seen that the interface area computed based on a volume fraction of 0.5 is remaining almost constant although further breakup is occurring. Especially cells containing small fluid droplets, i.e. cells with a volume fraction of 0.8, will cause an increase in computed surface area along the annulus. Cells that are predominantly filled with mud are decreasing further up the annulus and contribute less to the computed interface area. Figure 93 shows the computed phase interface area of the whole model domain based on different volume fractions.

The calculated standard deviation of phase volume fractions can be used as a measure for the sharpness of the phase interface. It provides a means to assess whether the flow is clearly separated or if it becomes dispersed and grid resolution needs to be refined. It may also be used to estimate the phase interface area in zones where the flow structures are not fully resolved. Based on the standard deviation one selects the volume fraction bounds for the bulk gas and mud phase. The volume between these bounds is assumed to contain many small droplets or bubbles that could not be resolved with the current grid. Based on the current mesh resolution fluid entities down to a size of 4 mm can be resolved. Droplets or bubbles with a smaller diameter can contribute substantially to the available interface area for mass transfer between the phases. The phase interface area computed based on a volume fraction of 0.5 would then be just a rough estimate. The surface introduced by small droplets need to be added to obtain the overall available interface area. A measure for the volume occupied by these droplets is given by the mud volume fraction contained in the phase interface volume. However assumptions would need to be made regarding the droplet size and size distribution.

Figure 94 shows an example on how the phase interface area would differ when taking into account the interface area due to droplets and bubbles that are currently not being resolved.

The graph illustrates the stacked interface area per channel segment. The smallest portion is due to the interface area calculated based on a volume fraction of 0.5, the largest portion is made up by gas bubbles (d~0.1 mm) and second largest portion is made up by mud droplets (d~1 mm). The calculation is based on a critical Weber number, predicting a stable bubble or droplet size based on equality of kinetic energy and surface energy. For the calculation the local phase velocity differences need to be evaluated. This analysis is very cumbersome and based on too many assumptions and therefore not further pursued. It is just illustrated here to give an impression on how big probably the influence of unresolved fluid structures could be and the limitation of interface area computation. The definition of critical droplet or bubble diameter is given below.

$$We^* = \frac{E_{kin}}{E_{surf}}, \qquad E_{kin} = \frac{\pi \rho d^2 U_r^2}{12}, \qquad E_{surf} = \pi d^2 \sigma$$

$$d = \frac{12\sigma}{\rho U_r^2}$$

$U_r$ relative velocity
$\rho$ fluid density
$d$ stable droplet/bubble diameter
$\sigma$ surface tension

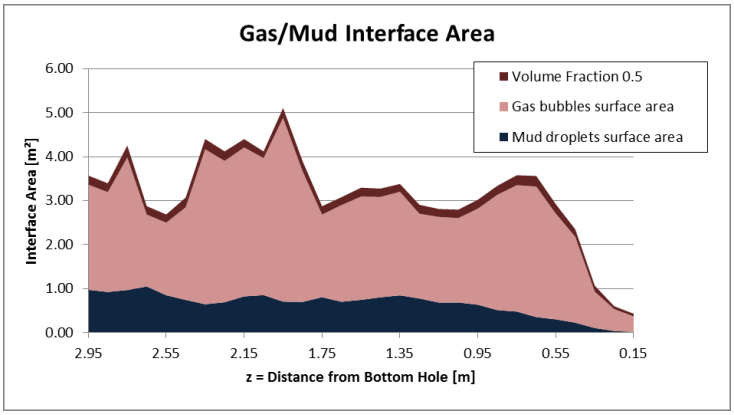


**Figure 94: Interface Area per Segment**

The following sequence of images (**Fehler! Verweisquelle konnte nicht gefunden werden.** to Figure 97) shows a snapshot of the transient flow simulation and the computed gas dissolution. Naturally there are local and timewise fluctuations in dissolved gas as a consequence of the mixing process. To ease the comparison of simulation results in the next section, values will be averaged over the annular cross section after the flow has fully developed.


**Figure 95: Detected Phase Interface**

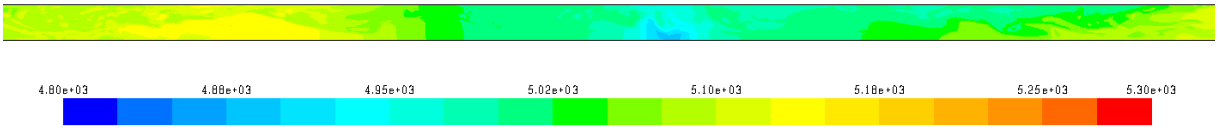


**Figure 96: Gas Solubility [mol/m³]**

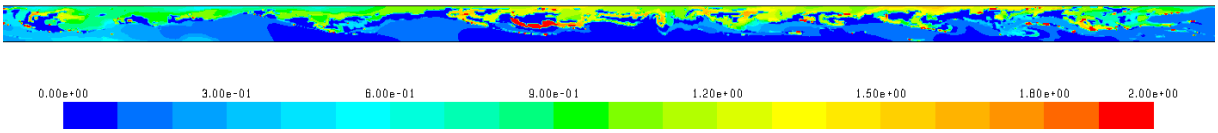


**Figure 97: Dissolved Gas [mol/m³]**

Next the selected lateral fracture kick simulation cases listed in Table 8 will be compared focusing on gas dissolution and associated parameters. Superficial mud velocity is the same for all cases since the mass flow boundary is equal. To determine the superficial gas velocity the mass flow rate and density at the gas inlet was measured. Based on superficial fluid velocities the expected flow regime of the simulation cases is illustrated in the flow pattern map for concentric vertical annuli provided by Caetano (1992), see Figure 98. According to the flow pattern map, simulation case LFK_6 is located right at the border between dispersed bubble flow and churn flow, the simulation cases LFK_0 and LFK_1 are both situated in the churn flow regime, and simulation case LFK_7211 is marked at the edge to annular flow. Looking at the snapshots of phase distribution provide in Figure 99 to Figure 102 the suggested classification appears quite realistic.

The differential pressure at kick onset is increased by a factor of ~10 between the simulation cases LFK_6, LFK_0, LFK_1 and by a factor of ~4 between the simulation cases LFK_1 and LFK_7211. The mean axial velocity along the annulus is shown in Figure 103. The computed specific interface area shows a similar trend for LFK_0 and LFK_1. Both are in the churn flow regime according to the flow pattern map. The clearly separated flow in the lower half of the annular channel causes a minimum phase interface area and is then followed by a strong interface area increase due to the evolving churn type flow. The smallest gas inflow in case LFK_6 is dispersing directly after the inlet, providing the highest phase interface area in this section, thereafter only slight breakup follows indicated by a moderate increase in specific interface area. The specific interface area belonging to the gas-kick scenario with the highest initial pressure difference, LFK_7211, shows an increase shortly after the separated flow at the gas inlet and is then slowly growing due to the breakup of liquid droplets in the gas stream. Since the gas will accelerate further on its way up the annulus due to expansion, the droplets will continue to breakup. Therefore the specific interface area plot may be extrapolated. The average gas volume fraction plot per simulation case depicted in Figure 104 indicates a correlation with flow regime.

Basically the flow regimes for all simulation cases will change towards annular flow with decreasing wellbore depth. The gas density decreases causing gas expansion shown by an increase in gas volume fraction. The entering mass flow of gas at the wellbore bottom stays the same or is even increasing due to a pressure drop in the wellbore. The decrease in gas density causes superficial gas velocities to increase on the way up to the surface whereas superficial mud velocities will stay the same as long as no mud is lost to the formation. As a consequence the kick scenario for an entire wellbore can be illustrated by a line in the flow pattern map, pointing from dispersed to annular flow. The starting point is defined by the pressure differential at kick onset and the bottom-hole pressure affecting gas density. The length of the segment is defined by the difference in bottom-hole and well head pressure. The lower the well head pressure the longer is the range in the flow regime map. However if gas dissolution occurs this line may be interrupted. For instance a kick scenario starts with a bubbly flow regime, gas dissolves and a single phase flow section follows, with decreasing solubility up the annulus gas comes out of solution, starting as dispersed flow but due to gas phase expansion a churn flow period follows until annular flow is reached. For gas dissolution the influence of flow regime on the interface area and on the mass transfer coefficient is crucial.

Figure 107 and Figure 108 show plots of the average mass transfer coefficient based on the two modeling approaches, i.e. Sherwood correlation based computation and the model of Kataoka and Miyauchi (1969) taking into account turbulent energy dissipation. Differences are mainly due to the entry effects, especially the high velocity simulation case LFK_7211 shows the highest mass transfer coefficient when taking into account turbulent energy dissipation. Further up the annulus mass transfer coefficients remain rather stable and can be grouped by flow regime, this is especially true for the Sherwood correlation based values. In general there is a large difference of a factor of ~50 between the two approaches. Consequently the same difference between the two models is found in the computed mass transfer rate, shown in Figure 107 and Figure 108. The fluctuations in mass transfer rate are due to the fluctuations in phase interface area.

Finally the concentration of dissolved gas along the annular model section is given in Figure 111 and Figure 112. Due to the continuous supply of fresh mud, the concentration of dissolved gas is lowest near the wellbore bottom and increases with elevation. The difference between the Sherwood correlation based computation and the turbulence based model by Kataoka is enormous. Extrapolating the dissolved gas profiles further up the annulus, Figure 113 and Figure 114, show the distance needed to reach full gas saturation of the mud.

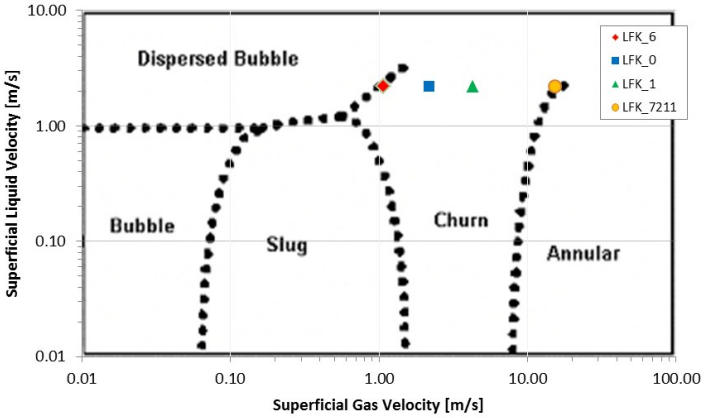


**Figure 98: Flow Pattern Map for Concentric Annuli, Caetano (1992)**

**Figure 99: LFK_6**

**Figure 100: LFK_0**

**Figure 101: LFK_1**

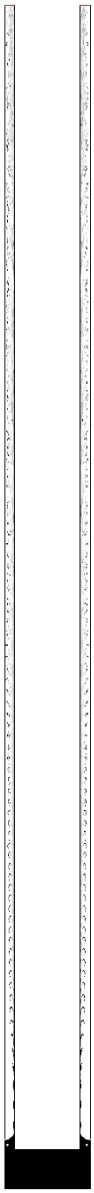

**Figure 102: LFK_7211**

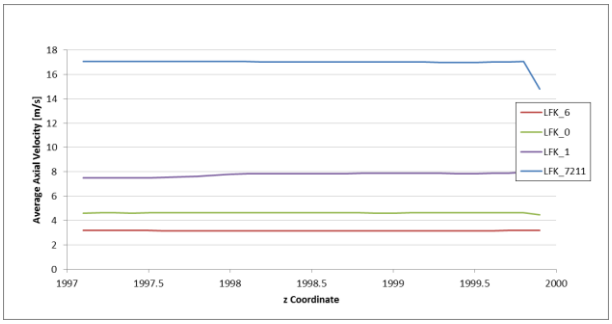


**Figure 103: Average Axial Mixture Velocity**

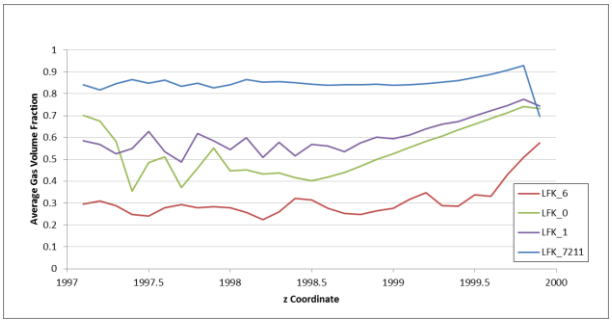


**Figure 104: Average Gas Volume Fraction**

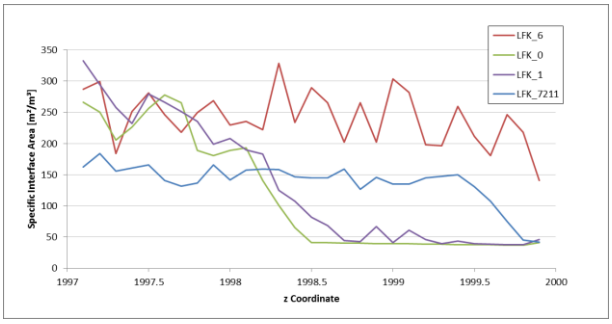


**Figure 105: Specific Interface Area**

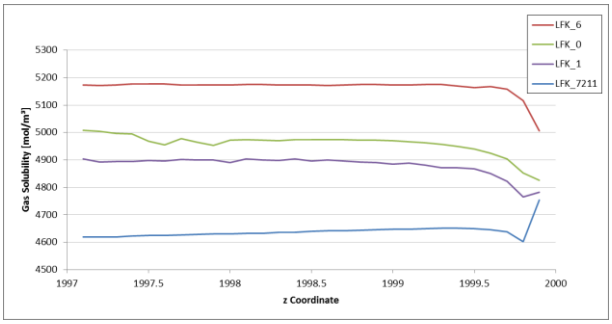


**Figure 106: Gas Solubility**

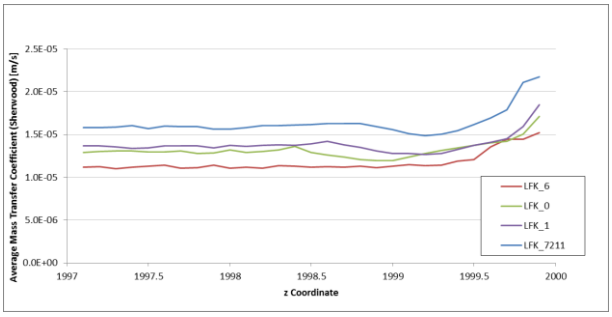


**Figure 107: Mass Transfer Coefficient (Sherwood Correlation)**

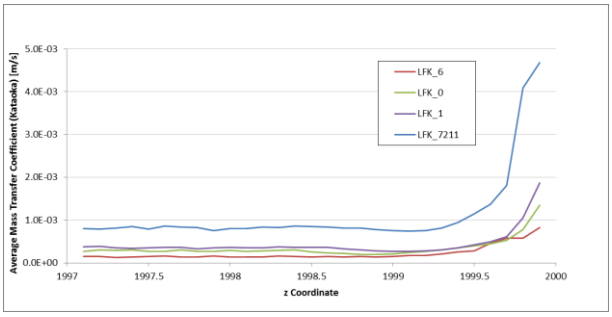


**Figure 108: Mass Transfer Coefficient (Kataoka Model)**

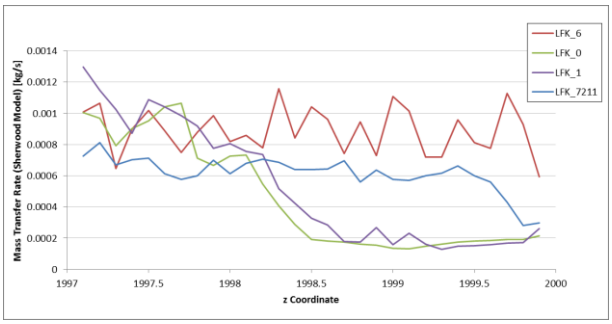


**Figure 109: Mass Transfer Rate (Sherwood Correlation)**

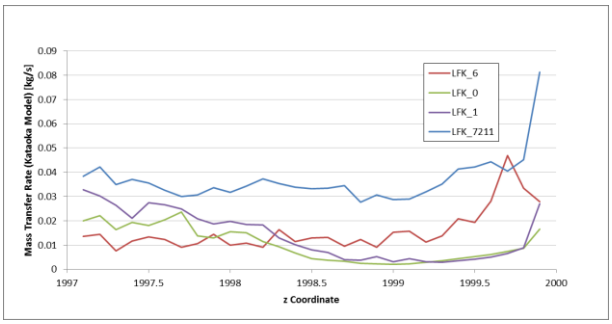


**Figure 110: Mass Transfer Rate (Kataoka Model)**

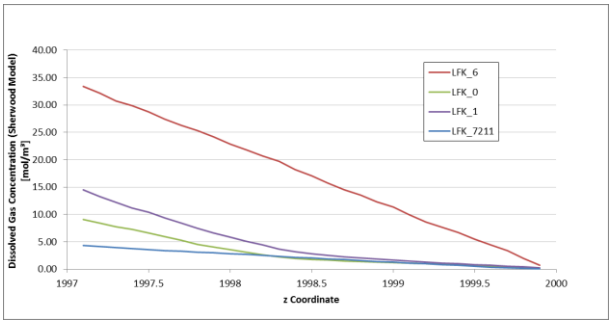


**Figure 111: Dissolved Gas Concentration (Sherwood Correlation)**

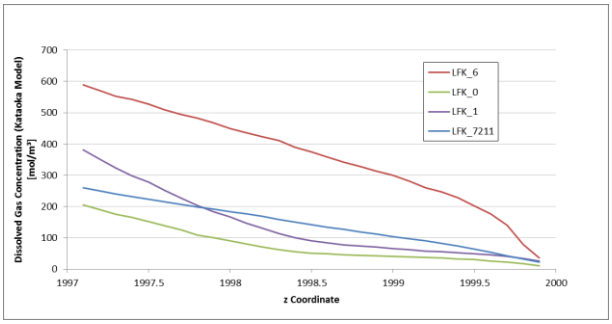


**Figure 112: Dissolved Gas Concentration (Kataoka Model)**

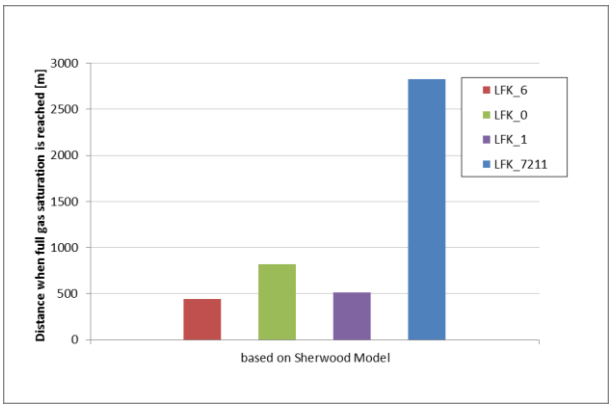


**Figure 113: Distance to Reach Full Mud Saturation (Sherwood Correlation)**

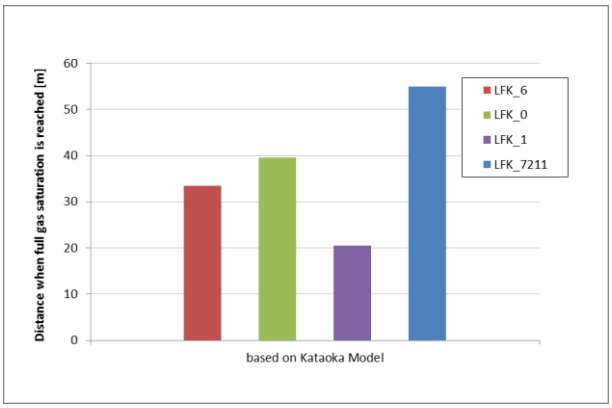


**Figure 114: Distance to Reach Full Mud Saturation (Kataoka Model)**

## *Bottom-Hole Kick Scenario – Multiple Fractures*

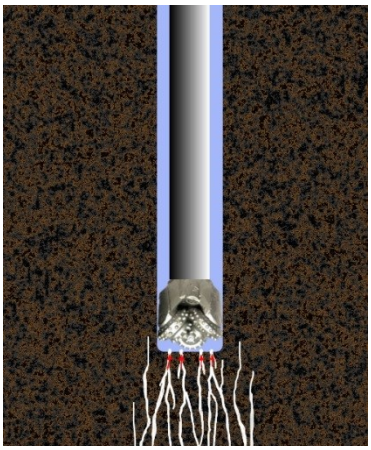

For this kick scenario, illustrated in Figure 115, multiple fractures at the wellbore bottom are modeled via two circumferential gaps with an opening size of 3 mm. The overall inflow area is the same as in the simulation cases with a single lateral fracture. Table 11 lists the parameters for the bottom-hole fracture kick scenario and in Table 12 lists comparable lateral fracture kick scenarios. In all three simulation cases the drill pipe and the bit section of the model are rotated at a rate of 100 rpm. The positioning of the simulation cases regarding flow regime according to Caetano (1992) is given in Figure 116.

**Figure 115: Wellbore Bottom Kick, Multiple Fractures**

**Table 11: Bottom-Hole Fracture Kick Scenario**

| Case | Gas Inlet Condition | Static Wellbore Pressure at Inlet | Δp at kick onset | Sup. Gas Velocity | Sup. Mud Velocity | Liquid Holdup |
|---|---|---|---|---|---|---|
| BHFK_1 | 233.6 bar | 232.5 bar | 1.1 bar | 0.84 m/s | 2.19 m/s | 0.78 |

**Table 12: Lateral Fracture Kick Scenarios**

| Case | Gas Inlet Condition | Static Wellbore Pressure at Inlet | Δp at kick onset | Sup. Gas Velocity | Sup. Mud Velocity | Liquid Holdup |
|---|---|---|---|---|---|---|
| LFK_6 | 233.33 bar | 233.3 bar | 0.03 bar | 1.07 m/s | 2.19 m/s | 0.69 |
| LFK_0 | 233.6 bar | 233.3 bar | 0.3 bar | 2.17 m/s | 2.19 m/s | 0.48 |

The static pressure integrated along the bottom-hole fracture openings before kick onset is 0.8 bars lower compared to the static pressure at the inlet of the lateral kick scenarios. Consequently the pressure differential at the kick onset is largest for the wellbore bottom kick scenario. However the final gas inflow is lowest for this case because the pressure situation is changing near the inflow boundary during the course of the kick. In case of the lateral kick scenarios the stagnation pressure at the gas inlet decreases as the mud is changing its flow path, resulting in an increase in gas influx. Case BHFK_1 and case LFK_6 share the same formation pore pressure, i.e. gas inlet pressure, but result in different kick morphology due to the difference in final gas inflow rate. Actually these two simulation cases would form a succession during drilling.

When the gas is introduced along the wellbore bottom fractures, lower flow rates occur compared to the lateral kick scenarios. This is due to the high pressure situation below the

drill-bit. The gas entering the wellbore trough the fractures gets sheared off by the rotating motion of the fluid representing the drill bit. Due to this process the kick gas is dispersed into bubbles and strong mixing of the phases occurs. These bubbles move upward through the drill-bit zone, where the injected drilling fluid is forming two large vortices representing the drill bit. While the gas bubbles pass through the vortices, some of them get caught by the swirling fluid, collide, coalesce and form larger bubbles caught in the vortices center.

The instantaneous phase distribution along the annulus after the flow has stabilized is shown in Figure 117 to Figure 120. In the lower model section rotating flow structures can be found as a consequence of the inlet configuration. The middle section shows axially sheared fluid ligaments, an indication for differences in axial gas and mud velocity. Eventually gas bubble shape becomes more distinct in the upper section of the model, which is basically a matter of low differential fluid velocity in the core of the channel and stronger shear near the walls causes smearing of the phases.

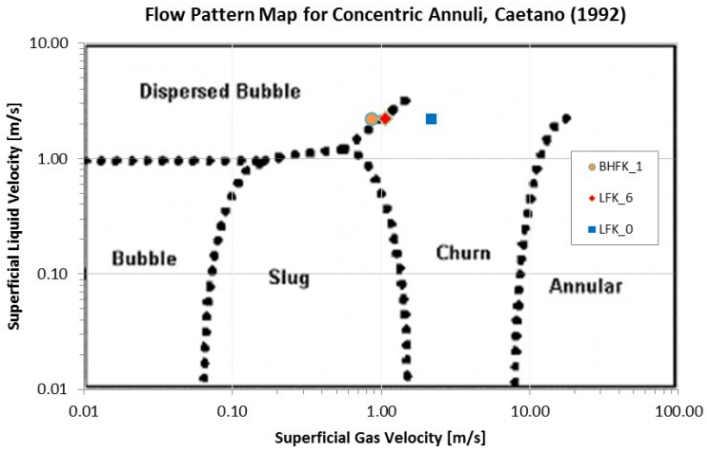


**Figure 116: Flow Pattern Map for Concentric Annuli, Caetano (1992)**


Figure 117: BHFK_1, Phase Distribution

Figure 118: Upper Section

Figure 119: Middle Section

Figure 120: Lower Section

A time history of gas contact at the inner pipe is illustrated in Figure 121. The inner pipe is split into 7 sections starting at the upper model end. Each series represents the average gas contact versus time of one segment. Impact of gas on the inner pipe is pronounced at the beginning of the channel and then gradually vanishes when travelling up the annulus. Due to

the vortices at the annulus the gas is first pushed to the inner pipe and then eventually accumulating in the channel core.

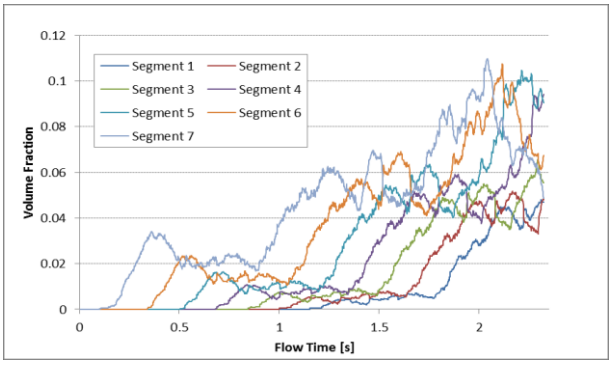


**Figure 121: Gas Contact at Inner Pipe, BHFK_1**

Monitoring the cross sectional distribution of the gas after the flow has become steady, it was found that the gas mud ratio near the channel walls remains rather stable while the largest fluctuations in volume fraction are found in the channel core; see Figure 123 and Figure 124. There are three peaks according to the travel paths of the gas fraction. The large gas bubbles denote the largest peak located the outer third of the annular gap, and the small gas bubbles form two pathways close to the walls. The asymmetry of the cross-sectional profiles is due to the annular conduit geometry; in a pipe the profiles would be symmetrical. Naturally the fluctuations in gas volume fraction occur since the gas is not flowing as a continuous stream of a bulk fluid. The three peaks showing up in the cross sectional gas volume distribution indicate that the flow regime is not a mere bubble flow but instead, especially due to the larger bubbles, close to a transition to slug flow. Experimental investigations of vertically upward flow in pipes conducted by Serizawa and Kataoka (1987) and illustrated in Figure 122 show similar profiles of void fraction distribution. They observed the transition from bubble to slug flow being accompanied by a change in void fraction profile from wall peaking to core peaking.

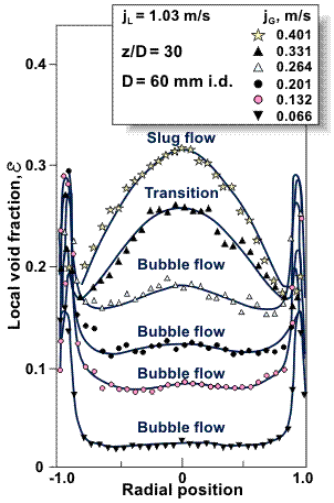


**Figure 122: Void Fraction Distribution of Vertically Upward Flow in Pipes, Serizawa and Kataoka (1987)**

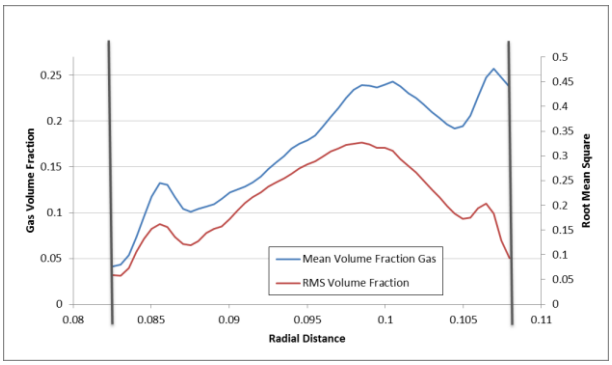


**Figure 123: Cross-sectional Gas Phase Distribution, z = 1997.4 m**

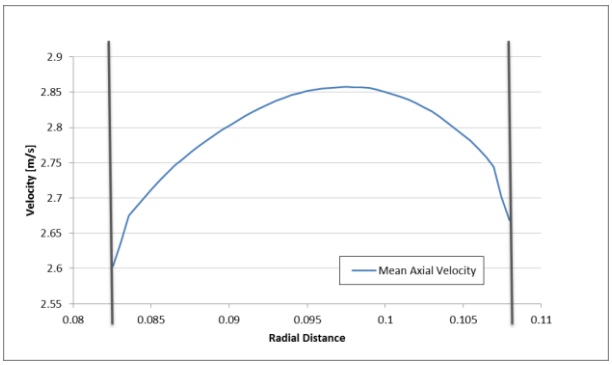


**Figure 125: Cross-sectional Profile of Mean Axial Velocity, z = 1997.4 m**

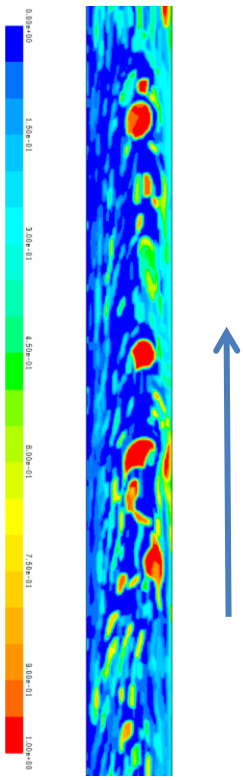

**Figure 124: Contour of Gas Volume Fraction**

Finally looking at the flow regime classification shown in Figure 116 the simulation case is confirmed to be at the transition between bubble and slug flow. The two lateral kick scenarios mentioned earlier are also indicated in this flow pattern map. Table 13 lists the dimensionless numbers for all three simulation cases. For case BHFK_1 and case LFK_6 the phase interface breakup is dominated by the velocity difference between the phases as indicated by the Weber number, whereas for LFK_0 the distortion of the phase interface is affected by turbulences of the initially separated phase streams.

**Table 13: Dimensionless Numbers**

| | BHFK_1 | LFK_6 | LFK_0 |
|---|---|---|---|
| $\dot{E}_{kin,g}$ | **34.28** | **70.24** | **582.17** |
| $\dot{E}_{kin,l}$ | 44,116 | 44,116 | 44,116 |
| $\dot{E}_{kin}$ ratio | 0.9984 | 0.9968 | 0.9740 |
| $U_{S,mix}$ | 3.03 | 3.26 | 4.36 |
| $Re_{L,in}$ | 3,124 | 3,124 | 3,124 |
| $Re_{G,in}$ | **6,914,386** | **7,968,185** | **16,117,466** |
| $We$ | **1,113** | **763** | **0.47** |
| $Mo$ | 3.65 | 3.65 | 3.65 |
| $Eo$ | 134 | 134 | 134 |
| $Fr_{gas}$ | **6.5** | **6.9** | **9.3** |

| | | | |
|---|---|---|---|
| ***Ri*** | **5,788** | **8,199** | **13,431,012** |

In context with flow patterns it is interesting to have a look at the frequencies of the occurring fluctuations in mud flow rate. For a sample analysis the mud flow rates at the model outlet were monitored for simulation case LFK_0 and BHFK_1, shown in Figure 126 and Figure 127 respectively. The mud rate log of LFK_0 clearly shows an initial plug displacement of the mud by the gas. Once the gas has reached the outlet of the model domain the mud flow rate starts to become volatile as a consequence of the 2-phase churn flow situation evolving. The time averaged mud flow rate approaches the pump rate indicating steady state. The shape of the mud flow rate history of case BHFK_1 sows quite a different behavior. In this case the low gas influx is not strong enough to cause a plug type displacement of the mud; instead the entering gas bubbles initiate a pulsatile mud flow.

The monitored flow rate at the upper exit of the model domain is equivalent to the mud return being observed at the well head, as long as no gas has left the domain. While gas travels up the annulus, the returning mud flow rate will be additionally increased due to expansion of the gas. Flow rate indicators are able to measure small increases in flow rate and can trigger warnings regarding kicks before pit level gains can be detected. Therefore, an observed increase in flow rate is usually one of the first indicators of a kick.

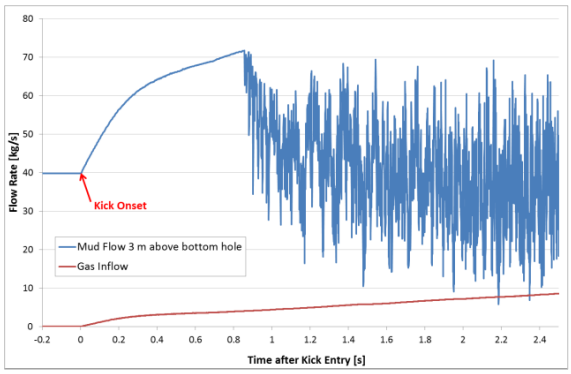


**Figure 126: Mass Flow Rates, LFK_0**

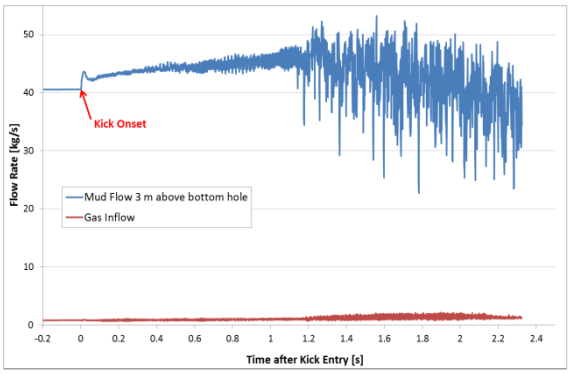


**Figure 127: Mass Flow Rates, BHFK_1**

Figure 128 and Figure 129 show the Fast Fourier Transform (FFT) of the mud flow rate for selected time periods, where the mud fluctuations and respective flow patterns appear to be more or less constant. For the lateral gas-kick three distinctive peaks where found in the spectral density plot i.e. at 13, 23 and 31 Hz. The results were visually compared with phase contour plots at the selected time period. All three frequencies correspond to a wispy annular flow regime, with a wavy mud film travelling up along the drill pipe and the outer cylinder being in contact with dry gas. Each frequency is indicating a characteristic flow entity size, for instance a fluid ligament or wave, as can be seen in the flow pattern plot in Figure 130Figure 130. In case of the gas-kick entering at wellbore bottom two time periods were analyzed. First a time period from 0.5 to 1 second; during this time no gas has reached the model outlet, but we can observe a pulsatile mud flow caused by the entering gas bubbles. During this time frame two 2 high frequency peaks at 113 and 157 Hz are observed. The explanation for these two peaks is that there must be at least two characteristic bubble or slug

sizes appearing repeatedly in a short time interval at the entry of the annulus. If bubbles would be generated arbitrarily with a uniform size distribution, such prominent peaks could not be observed. Instead the outcome of the FFT analysis would look like a random signal. At the second time frame (1.3 to 2.2 s) gas has reached the outlet and a stable flow pattern has established. A very distinctive peak at a frequency 132 Hz can be seen. Again this tells us that there must be a periodic appearance of similar sized flow entities. The phase contour plot in Figure 131 illustrates the origin of the two frequency peaks. The large gas pockets generated at the entry of the annulus with a length of approximately 1.8 cm and a separation distance of 4 cm, travelling at a velocity of 6 m/s are responsible for the frequency peak at 157 Hz. The longer fluid ligaments besides the gas slugs are rising at a lower velocity and show a frequency of roughly 113 Hz. Finally the flow pattern in Figure 157Figure 132 shows the repeating occurrence of larger gas bubbles in the core flow at the model outlet with a frequency of 132 Hz.

Regarding the selected simulation cases this type of analysis provides us with the understanding that larger flow structures will result in slower fluctuations whereas smaller flow structures like bubbles will result in higher fluctuation frequencies. Additionally the size of the flow structures is making a clear footprint in the frequency domain. It should also be noted that especially for gas-kicks with larger flow rates, the increasing amount of gas in the annulus will tend to dampen flow and pressure fluctuations resulting in smoother time histories and less pronounced peaks in the frequency domain. Summing up this analysis shows that the time history of mud pulsations contains valuable information in terms of 2-phase flow morphology.

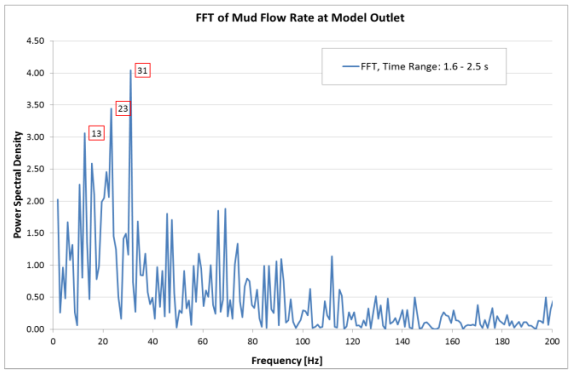


**Figure 128: FFT of Mud Flow Rate, LFK_0**

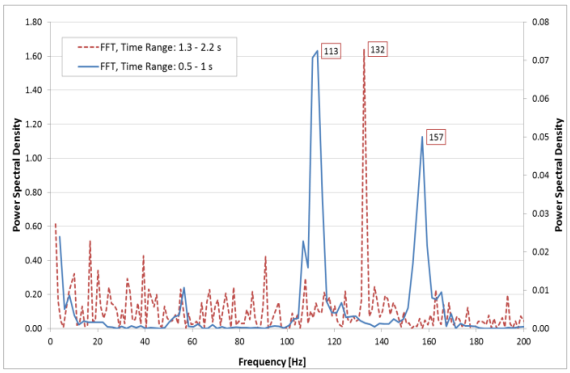


**Figure 129: FFT of Mud Flow Rate, BHFK_1**

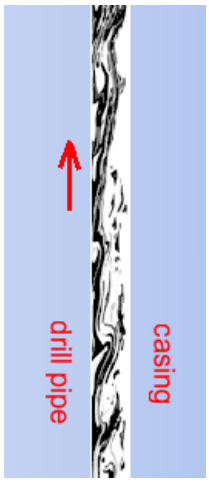


**Figure 130: Flow Pattern at Model Outlet, LFK_0, t = 2.45 s**

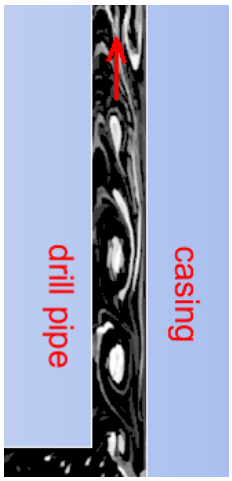


**Figure 131: Flow Pattern at Annular Entry, BHFK_1, t = 0.63 s**

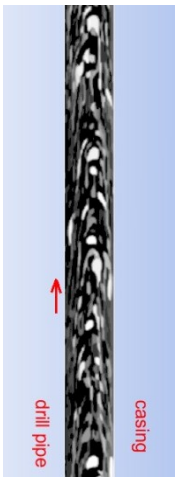


**Figure 132: Flow Pattern at Model Outlet, BHFK_1, t = 2.24 s**

Figure 133 illustrates the transient change of flow patterns for simulation case BHFK_1 and LFK_0. Calculation of superficial velocities is based on the flow rates and gas density monitored at the model outlet. Both cases begin with a dispersed bubble flow when the first gas enters the wellbore. The higher superficial mud velocity of case LFK_0 is due to the mud displacement caused by the gas, seen as pit gain at the surface. Basically case LFK_0 shows a broader range of values compared to case BHFK_1.

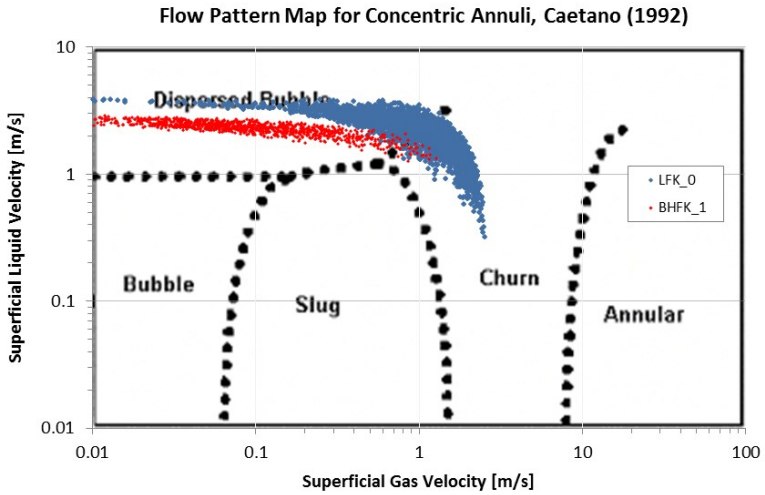


**Figure 133: Flow Pattern Map for Concentric Annuli, Caetano (1992)**

Finally the three simulation cases listed in Table 11 and Table 12 are compared with respect to gas dissolution and its major parameters. The details are illustrated in Figure 134 to Figure 145. Simulation cases LFK_6 and BHFK_1 both show dispersed flow characteristics. Both cases show similar gas flow rates as reflected by the average axial mixture velocities in Figure 134. Average gas volume fraction is largest for simulation case LFK_0. The highest gas volume fraction is found next to the gas inlet, it is then decreasing along a separated flow

section until the fluctuations indicate the onset of the churn flow regime. The volume fraction series of case LFK_0 similarly starts with a high gas volume fraction near the inlet; this appears to be characteristic for this inlet location. The smooth profile of simulation case BHFK_1 is due to the finely dispersed gas volume fraction. Specific interface area illustrated in Figure 136 shows lowest values for the separated flow section of case LFK_0. Further up the annulus the phase interface is strongly increasing due to the enhanced breakup in the churn flow regime. Specific interface area values of the two dispersed flow cases range within the same bounds. The computed mass transfer coefficients show a similar trend for both approaches. Mass transfer coefficients of case LFK_6 and BHFK_1 only differ near the lateral gas inlet. Mass transfer coefficients of case LFK_0 clearly show the influence of the velocity difference between gas and mud. The highest velocity difference occurs at the lateral gas inlet. Gas and mud velocity then gradually aligns, which is accompanied by a decrease in mass transfer coefficient reaching a minimum were gas and mud are flowing at equal speed. After that buoyancy is the mere factor causing relative fluid velocities resulting in random fluctuations of the mass transfer coefficient. In case of the Sherwood-based approach the shape of the computed mass transfer rate profiles reflects the profile of the specific phase inter face area. The higher mass transfer coefficients of the Kataoka model level out the lower specific interface area at the beginning of the annulus in case of LFK_0. The difference between the mass transfer computation approaches for simulation case BHFK_1 accounts for a factor of ~ 10. The two dispersed flow simulation cases show the highest concentration in dissolved gas. Finally extrapolating the dissolved gas profiles further up the annulus shows the distance needed to reach full gas saturation of the mud in Figure 144 and Figure 145.

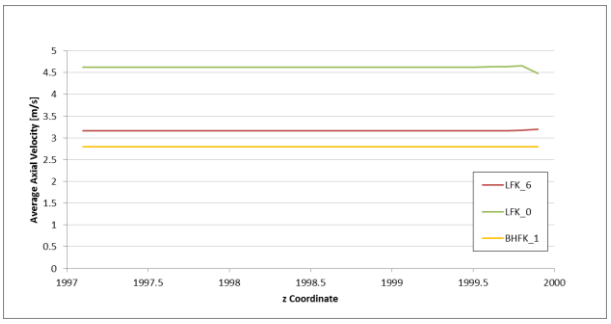


**Figure 134: Average Axial Mixture Velocity**

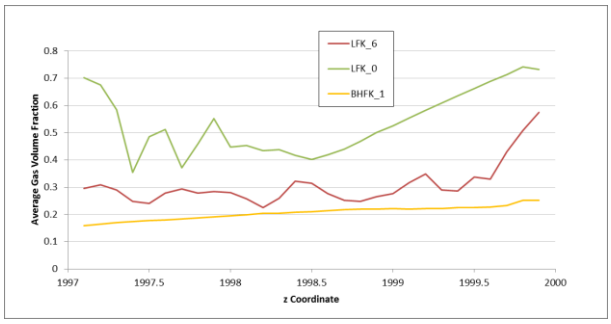


**Figure 135: Average Gas Volume Fraction**

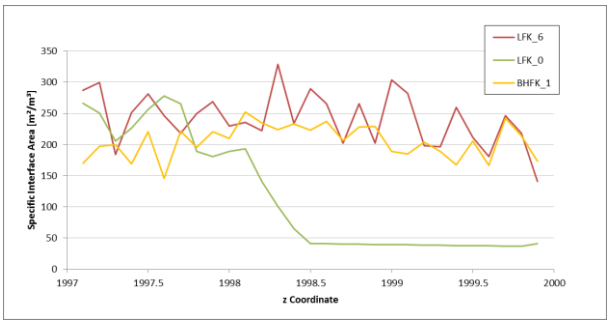


**Figure 136: Specific Interface Area**

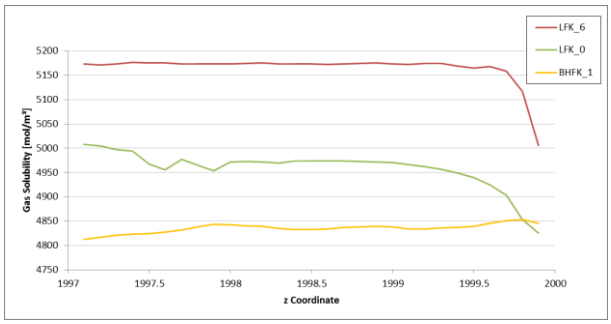


**Figure 137: Gas Solubility**

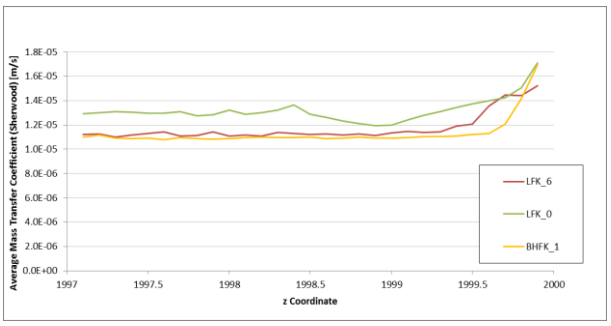


**Figure 138: Mass Transfer Coefficient (Sherwood Correlation)**

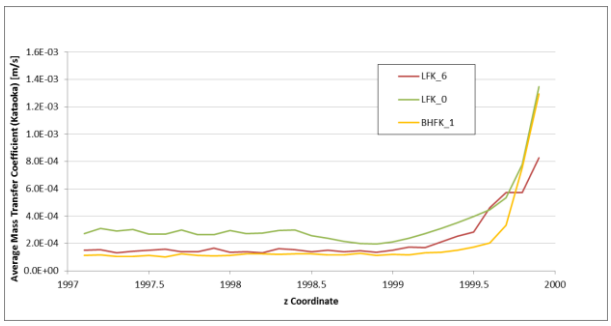


**Figure 139: Mass Transfer Coefficient (Kataoka Model)**

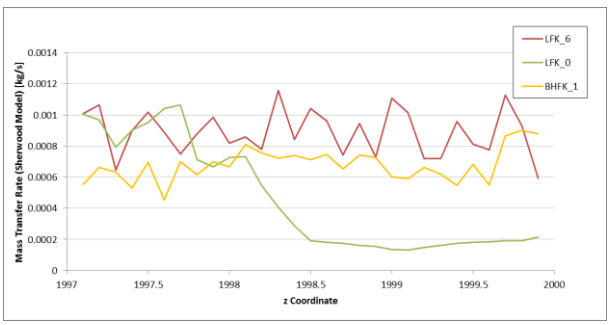


**Figure 140: Mass Transfer Rate (Sherwood Correlation)**

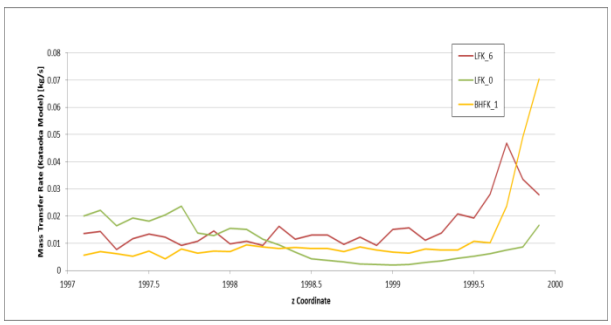


**Figure 141: Mass Transfer Rate (Kataoka Model)**

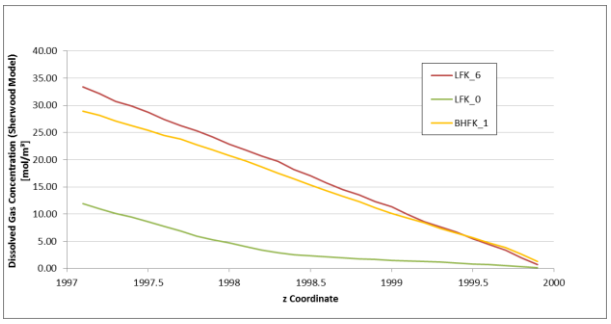


**Figure 142: Dissolved Gas Concentration (Sherwood correlation)**

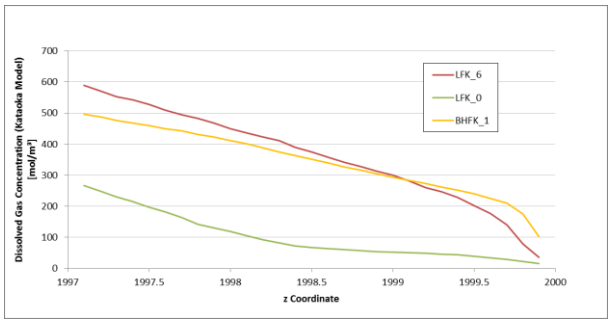


**Figure 143: Dissolved Gas Concentration (Kataoka model)**

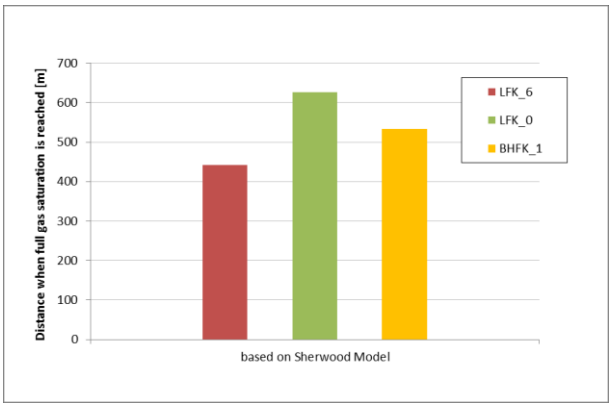


**Figure 144: Distance to Reach Full Mud Saturation (Sherwood Correlation)**

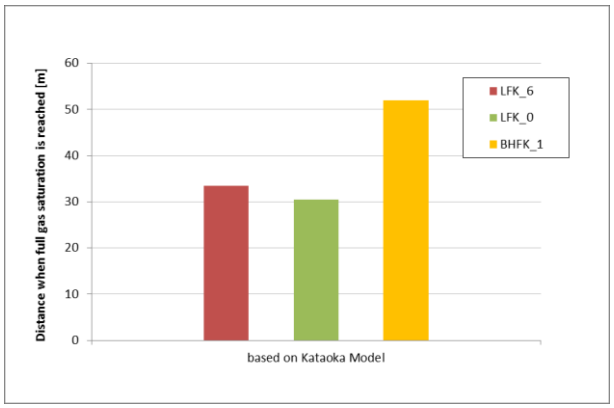


**Figure 145: Distance to Reach Full Mud Saturation (Kataoka Model)**

## Loss of Mud Circulation

When drilling into highly fractured formations, formations with high permeability or cavernous formations loss of drilling mud circulation can occur. Drilling mud will then flow into the surrounding formation causing no or reduced mud flow to the surface. The loss of fluid reduces the hydrostatic pressure in the wellbore and when it becomes lower than the formation pressure gas enters the wellbore and causes a kick. To investigate the possibility of lost circulation during a gas-kick event several model scenarios were simulated. These scenarios cover both constant pressure and constant mass flow inlet boundary conditions at dedicated kick locations. The pressure inlet boundary it is not restricted to the gas phase but also allows the passage of mud. The modeled scenarios range from a cavernous gas inlet area located either directly below the drilling bit or laterally next to the wellbore bottom.

### *Lateral Kick Scenario – Cavernous Opening*

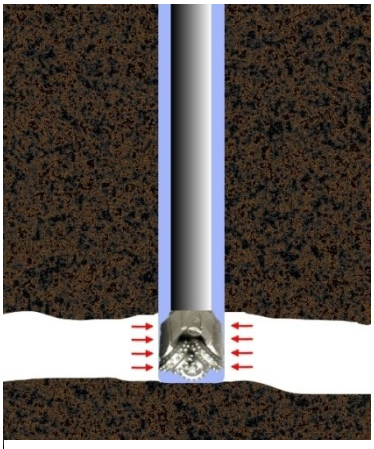

**Figure 146: Lateral Kick Scenario, Cavern**

This kick scenario represents a gas inflow from a cavernous opening located laterally of the drill bit. The large inlet area provokes a massive inflow of formation gas. Two simulations with different gas inlet conditions are compared. Table 14 lists the main differences between the simulation cases. In both setups the inner pipe, drill bit and annular channel are rotated at a rate of 100 rpm. In case LCK_1 a pressure boundary condition of 233.3 bars is applied at the gas inlet. This corresponds to a pressure differential of 1.8 bars at kick onset. Case LCK_2 is setup with a constant mass flow inlet of 3 kg/s for the kick gas. The mass flow inlet condition refuses mud to leave the wellbore. Consequently no loss of circulation can occur even if the initial pressure situation would dictate it.

**Table 14: Simulation Cases: Lateral Cavern Kick**

| Case | Gas Inlet Condition | Static Wellbore Pressure at Inlet | Sup. Gas Velocity | Sup. Mud Velocity | Liquid Holdup |
|---|---|---|---|---|---|
| LCK_1 | 233.3 bar | 231.5 bar | 10.04 m/s | 2.19 m/s | 0 |
| LCK_2 | 3 kg/s | | 1.43 m/s | 2.19 m/s | 0.56 |

The final (steady-state) phase distribution for both simulation cases is shown in Figure 147 and Figure 148 respectively. The peculiar shape of the phase interface near the wellbore bottom is due to entrainment of the mud stream.

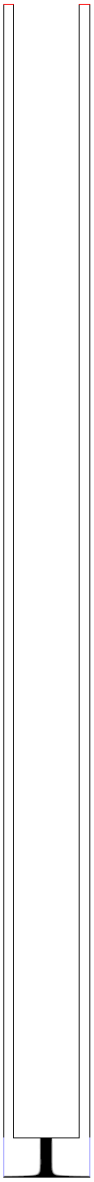

Figure 147: LCK_1

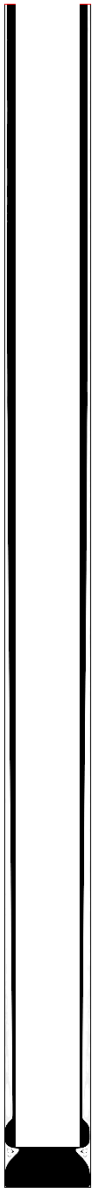

Figure 148: LCK_2

In LCK_1 all mud is lost to the formation and the gas-kick is fully occupying the annular channel resulting in high gas superficial velocity of ~ 10 m/s. The mass flow rate of the gas stabilizes at a value of 20.78 kg/s. The only resistance left for the gas on its way up the annulus is the remaining mud column, until this scenario results in a blow-out.

In case of the mass flow boundary condition applied in LCK_2, the mud is forced to flow up the annulus at its inflow rate since there is no alternative passage for the mud to escape into the formation. As a consequence mud and gas is flowing concurrently upwards, clearly separated by a smooth interface area. Eventually the mud is occupying 56 % of the annular volume. The evolution of total gas volume fraction in the annular channel of this simulation case is shown in Figure 149.

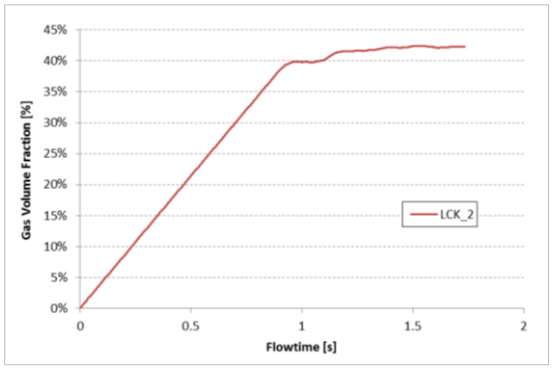


**Figure 149: Total Gas Volume Fraction in Annulus, LCK_2**

In LCK_2 gas entering the wellbore is changing the flow path for the mud. The space occupied by the gas in the annulus reduces the available passage space for the drilling mud and increases flow resistance. In the model the mud inflow is modeled by a constant mass flow boundary, in reality a higher pump pressure would be needed to keep the circulation rate at the same level. In general the selection of a constant mass flow boundary for the gas inlet, prohibiting the loss of mud, appears to better match a kick situation where gas is escaping from porous media instead of a cavern.

Regarding the simulation case LCK_1, a transient snapshot of the phase distribution at t=0.55 seconds after kick onset is shown in Figure 150. The mud phase shown in black is forming a thin film on the wellbore bottom that is flowing radially outward into the formation. The gas is pushing the remaining mud column in the annulus upwards. Some liquid is initially attached at the outer cylinder and a few liquid ligaments are trapped in the gas core, but the flow is basically separated.

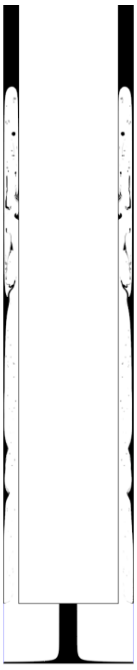

**Figure 150: LCK_1, t = 0.55 s**

The dimensionless numbers characterizing the simulation cases are listed in Table 15. Since the fluid properties and channel geometry are the same for both simulation cases, Morton and Eötvös number are basically the same. There are only small differences in gas density due to differences in pressure, but this is negligible. The dominant factor is the difference in gas inflow velocity, expressed by the kinetic energy of the gas stream, high gas Reynolds number and mixture velocity. A high Weber number represents the dominance of inertia forces compared to surface tension force. It is a measure for phase interface distortion and is proportional to the square of the phase slip velocity. The Weber number calculated for the annulus is about 5 times higher looking at the transient snapshot of LCK_1 compared with the smooth annular flow of LCK_2. The gas Froude number expresses the ratio of inertia to buoyancy force. When the flow has reached steady state in the model, the gas Froude number of the two simulation cases differs by a factor of ~3. However it is interesting to see that the gas Froude numbers are quite similar when comparing the transient snapshot of LCK_1 with the fully developed flow of LCK_2. This is because the gas inflow velocity is still increasing as a result of the pressure inlet condition. Consequently the kinetic energy brought into the system by the gas is still low. The superficial gas velocity at this stage amounts only 0.6 m/s, naturally the phase slip is largest resulting in the breakup of the phase interface.

**Table 15: Dimensionless Numbers, Lateral Cavern Kick**

| | LCK_1, t = 0.55 s | LCK_1 | LCK_2 |
|---|---|---|---|
| $\dot{E}_{kin,g}$ | **0.01** | **52.56** | **0.15** |
| $\dot{E}_{kin,l}$ | 44,116 | 44,116 | 44,116 |
| $\dot{E}_{kin}$ ratio | 1.00 | 0.9976 | 1.0000 |
| $U_{S,mix}$ | **2.81** | **12.23** | **3.62** |
| $Re_{L,in}$ | 3,124 | 3,124 | 3,124 |
| $Re_{G,in}$ | **4,599,816** | **75,263,131** | **10,865,707** |
| $We$ | **1,508** | **-** | **351** |
| $Mo$ | 3.65 | 3.65 | 3.64 |
| $Eo$ | 133 | 133 | 133 |
| $Fr_{gas}$ | **6.0** | **26.0** | **7.7** |
| **Ri** | **4,145** | **168** | **17,782** |

The positioning of the simulation cases regarding flow regime according to Caetano (1992) is given in Figure 151. According to this classification the simulation cases are located near the lower and upper end of the churn flow regime. Despite the blow out scenario of simulation case LCK_1, case LCK_2 does not confirm the churn flow prediction but instead shows annular flow morphology. The reason for this deviation in flow morphology arises from the applied rotation rate to drill pipe, drill bit zone, and annular channel. As discussed in Chapter 5: Influence of Rotation, a rotation rate of 100 rpm applied only to the inner cylinder will not initiate any flow instabilities. This is also confirmed by the lateral gas kick scenarios, which are well represented by the flow regime map of Caetano although the drill pipe is rotating. In simulation case LCK_2 the rotation is not only applied to the inner cylinder and drill bit section, but also to the annular fluid zone which results in a stronger influence on the flow field. The fluid rotation causes an initial smoothing of the gas-liquid phase interface; any

radial discontinuity gets averaged in circumferential direction, as one can observe when stirring in a coffee cup. The lateral gas inlet forces the mud stream to initially travel next to the inner cylinder, however centrifugal forces will begin pushing the heavier fluid radially outwards. To illustrate how the flow regime will be affected thereby, a longer model section needs to be modeled. Nevertheless the wellbore section were rotation plays a dominant role on flow morphology is limited to the near drill bit zone. Further up the annulus, were no rotation is applied the centrifugal momentum will quickly vanish and be overruled by buoyancy.

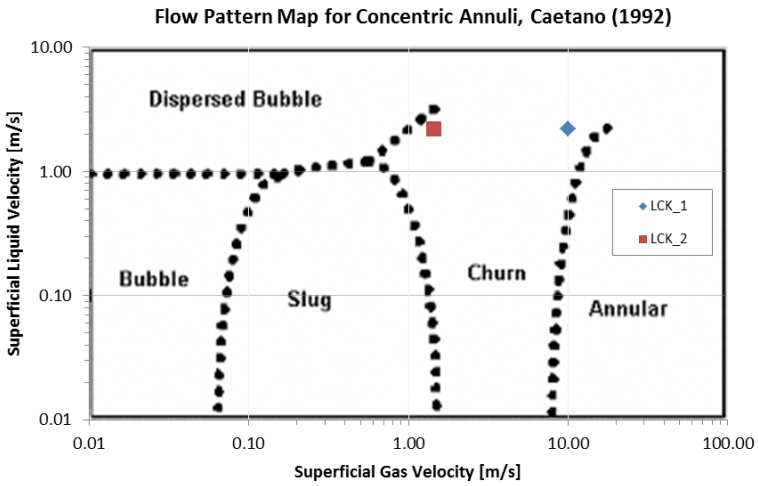


**Figure 151: Flow Pattern Map for Concentric Annuli, Caetano (1992)**

## *Bottom-Hole Kick Scenarios*

For this setup it is assumed that the kick occurs at the bottom of the well while drilling. Two possible configurations are sketched in Figure 152 and Figure 153. On the left the wellbore approaches a large cavernous opening and on the right the bottom-hole area is assumed a homogeneous porous layer.

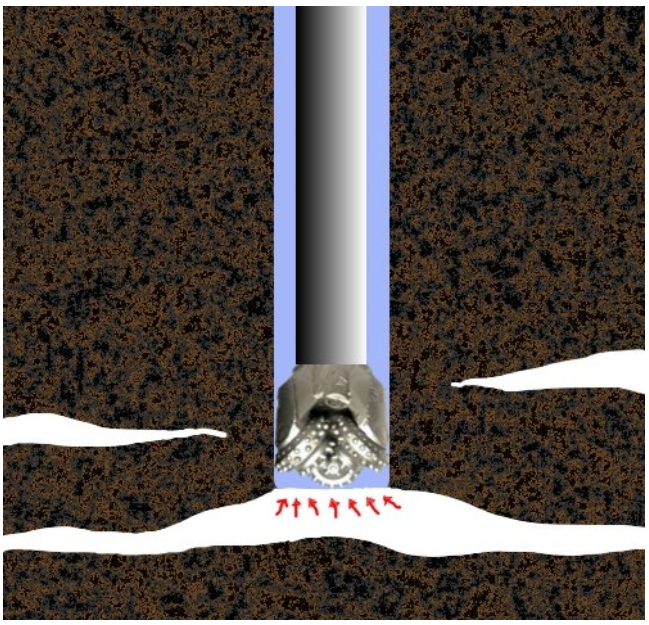

**Figure 152: Wellbore Bottom Kick Scenario, Large Opening = Cavern**

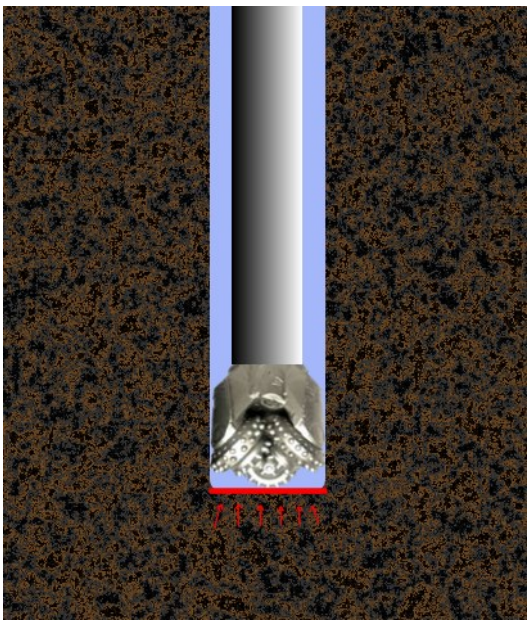

**Figure 153: Wellbore Bottom Kick Scenario, Porous Media Boundary**

**Table 16: Simulation Cases: Bottom-Hole Cavern Kick**

| Case | Gas Inlet Condition | Rotation | Sup. Gas Velocity | Sup. Mud Velocity | Liquid Holdup |
|---|---|---|---|---|---|
| BHPK_2 | 3 kg/s | 100 rpm, channel | 1.45 m/s | 2.19 m/s | 0.74 |
| BHPK_4 | 3 kg/s | 0 | 1.45 m/s | 2.19 m/s | 0.67 |
| BHCK_32 | 234 bar | 100 rpm, only bit | 26 m/s | 2.19 m/s | 0 |

Three simulation cases are discussed; the main simulation parameters are listed in Table 16. Case BHPK_2 and BHPK_4 apply a constant mass flow boundary for the kick gas and BHCK_32 applies a pressure inlet condition. Again the pressure inlet condition realistically reproduces any loss of circulation that may occur when drilling overbalanced into a cavern, whereas the mass flow inlet condition prohibits any mud loss. Actually the latter can be compared with a different geometric configuration, i.e. an adjacent porous media which is permeable to the gas phase but impermeable to the mud phase, see Figure 153. This

assumption of impermeability for the mud is reasonable since the permeability for the gas is way higher due to the high ratio in viscosity of the two fluids.

The positioning of the simulation cases with respect to flow regime classification according to Caetano (1992) is given in Figure 154. The two simulation cases representing the porous media boundary configuration share the same position in the churn flow regime of the map. The position is defined by the identical gas superficial velocity, thus one would expect identical flow morphology. However when looking at the phase distribution illustrated in Figure 155 and Figure 157 a strong deviation in flow regimes can be seen.

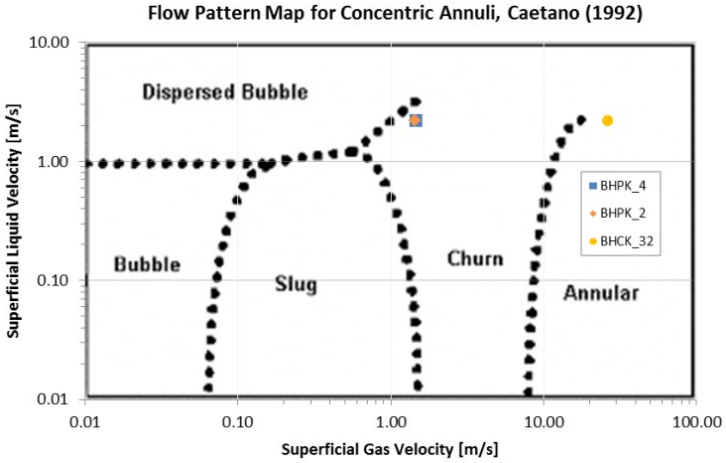


**Figure 154: Flow Pattern Map for Concentric Annuli, Caetano (1992)**

The only difference between simulation case BHPK_2 and BHPK_4 is in terms of applied rotation. For the former case a rotation rate of 100 rpm is applied to the whole fluid domain and inner cylinder, and for the latter simulation case no rotation is active. The flow regime map of Caetano is based on experiments without fluid rotation. Similarly to the lateral cavern kick simulation studies discussed earlier a smoothing of the phase interface can be observed due to fluid zone rotation.

Figure 155: BHPK_2

Figure 156: BHPK_4

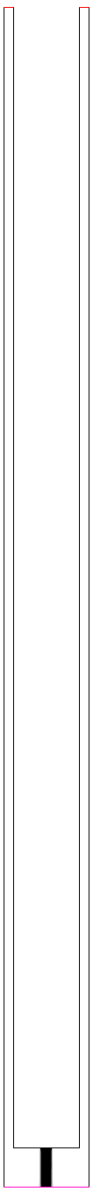

Figure 157: BHCK_32

As can be seen from Table 17 the dimensionless numbers of both simulation cases are identical although the phase distribution shown in Figure 155 and Figure 156 differs considerably. This is due since none of the listed dimensionless numbers covers the effect of rotation, which in this particular case turned out to be quite strong with respect to phase interface distortion. A dimensionless number suitable to characterize the influence of rotation is the Rossby number, described in Chapter 5: Influence of Rotation. The rotation applied to the fluid zone appears to have a strong separating effect on the phases, especially close to the wellbore bottom. The applied radial acceleration to the fluid due to pipe rotation is small and it takes some time until this will push the mud towards the outer cylinder, especially when the movement is overlapped by high axial velocities. Therefore the interface smoothening effect due to the tangential velocity component is larger than the mixing effect due to the radial

velocity component. This can be seen in Figure 155, the heavier mud phase stays close to the inner cylinder and the phase interface is very smooth. The evolving flow morphology corresponds to annular flow as known from flow in pipes. The strong cross-sectional mixing seen in Figure 156 is a result of fluid motion without any rotation applied. Figure 158 and Figure 160 show histograms of axial and radial mixture velocities in the annular channel. The simulation case with no rotation applied, BHPK_4, shows the broadest distribution of radial velocity. The radial component due to radial phase displacement is larger than the radial velocity induced by rotation. The circumferential velocity component induced by rotation is smoothing the phase interface. When looking at the axial shear of the fluid in the annular channel, see Figure 159, the simulation case without rotation shows an almost symmetric distribution of axial shear and the simulation case with rotation shows two distinct ranges of shear values. The lower range of axial shear is occurring at the gas-mud interface, the peak with the higher axial shear values belongs to the axial shear occurring within the bulk mud. Within the bulk gas the axial velocity is almost uniform and axial shear is a minimum.

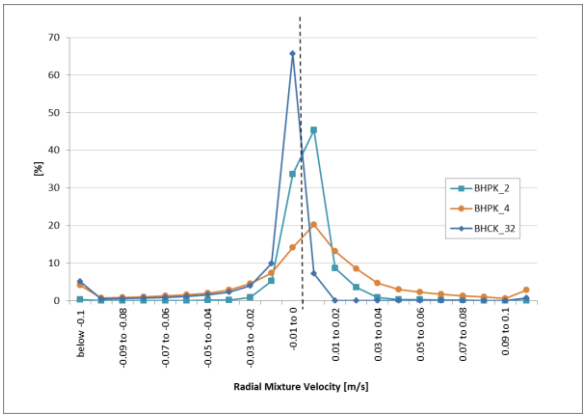


**Figure 158: Histogram of Radial Mixture Velocity**

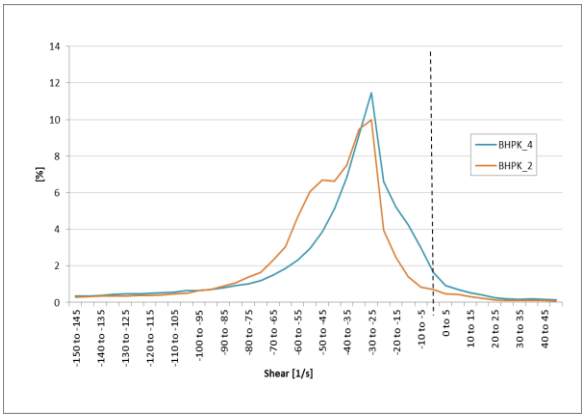


**Figure 159: Axial Shear in Annular Channel**

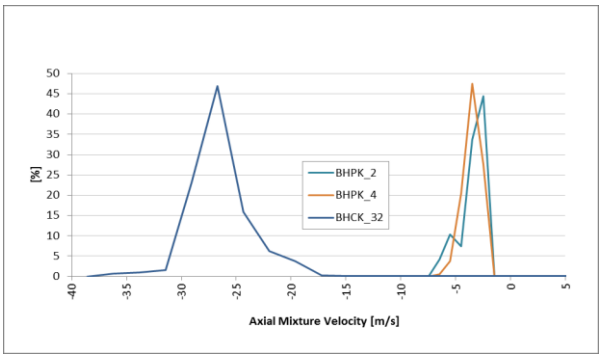


**Figure 160: Histogram of Axial Mixture Velocity**

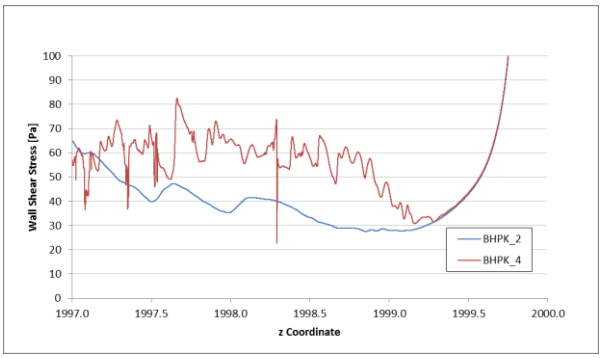


**Figure 161: Wall Shear Stress at Inner Pipe**

**Table 17: Dimensionless Numbers, Bottom-Hole Kick Scenarios**

| | BHPK_2 | BHPK_4 | BHCK_32 |
|---|---|---|---|
| $\dot{E}_{kin,g}$ | **0.54** | **0.54** | **3197** |
| $\dot{E}_{kin,l}$ | 44,116 | 44,116 | 44,116 |
| $\dot{E}_{kin}$ **ratio** | **1.00** | **1.00** | **0.86** |
| $U_{S,mix}$ | **3.64** | **3.64** | **28.36** |
| $Re_{L,in}$ | 3,124 | 3,124 | 3,124 |
| $Re_{G,in}$ | **10,865,707** | **10,865,707** | **196,126,013** |
| $We$ | 335 | 333 | - |
| $Mo$ | 3.65 | 3.65 | 3.65 |
| $Eo$ | 133 | 133 | 133 |
| $Fr_{gas}$ | **7.8** | **7.8** | **60.4** |
| $Ri$ | **18,665** | **18,787** | **-** |

Regarding simulation case BHCK_32 the applied pressure at the bottom-hole inlet amounts 234 bars, which is 0.5 bars more than the average stagnation pressure at the bottom-hole area. In this case only the drill bit section is rotated at a rate of 100 rpm. A time series of phase distribution is shown in Figure 162 to Figure 165, mud is indicated in blue and gas in red.

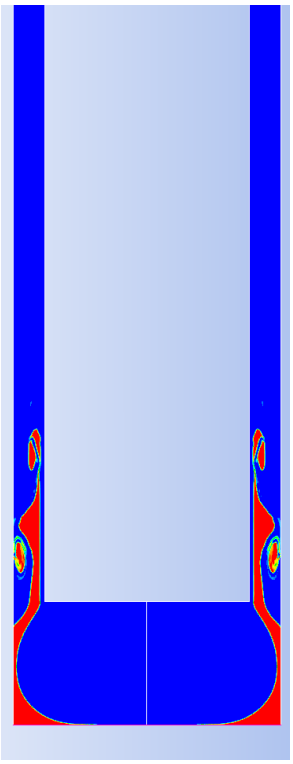

**Figure 162: t = 0.05 s**

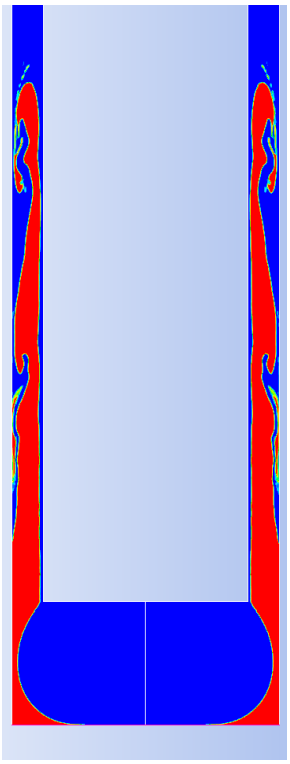

**Figure 163: t = 0.13 s**

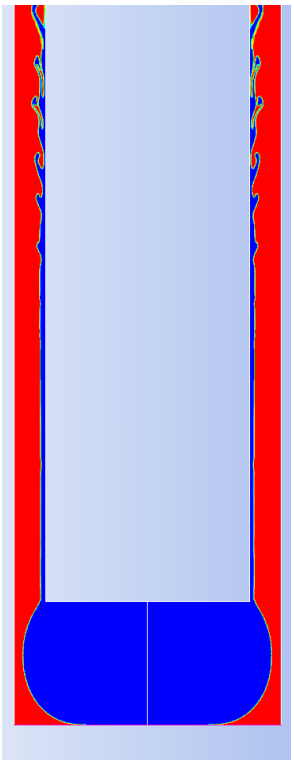

**Figure 164: t = 0.6 s**

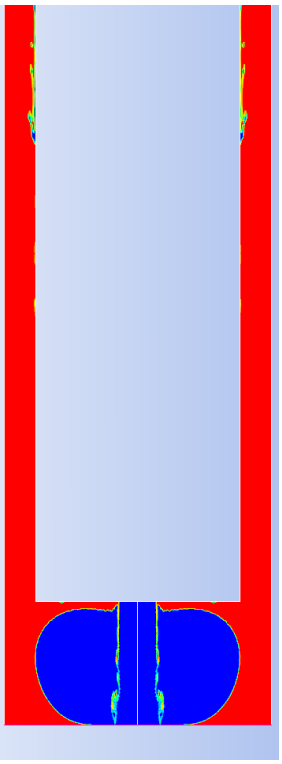

**Figure 165: t = 0.9 s**

Similar to the lateral cavern kick scenarios the large inflow area results in a loss of circulation and a massive gas inflow. The high stagnation pressure in the drill bit section of the model will always lead to mud loss when drilling into a cavern. Initially gas enters in the lower pressure zones at the corners. While mud is flowing into the cavern, the overall pressure in the dill bit area drops. The hydrostatic head of the remaining mud column in the annulus is left to

counteract the gas inflow. As the pressure of the inflowing gas is higher and the well is not closed, the mud is being pushed upwards until the whole channel of the model is filled with gas. The increase in gas volume fraction in the modeled domain is shown in Figure 166. The bend in the time series indicates the removal of the bulk mud. Remaining wall films are removed after ~ 1.3 s when the whole channel is filled with gas.

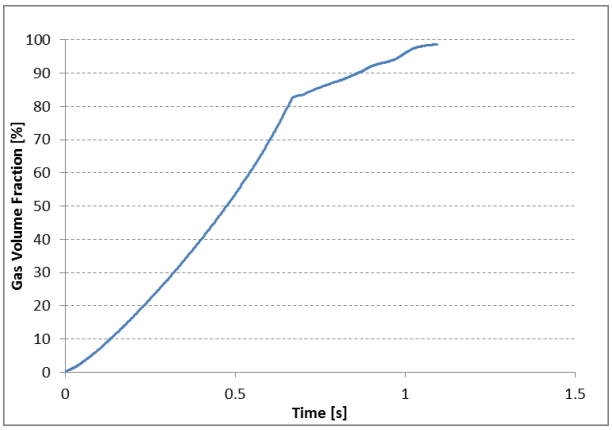


**Figure 166: BHCK_32, Gas Volume Fraction**

Finally simulation case BHPK_2 and BHPK_4 are compared regarding gas dissolution and its major parameters, see Figure 167 to Figure 178 for the details. Average axial mixture velocities are nearly equal. Case BHPK_4 is showing a higher gas volume fraction and naturally a much larger specific interface area along the annulus. However mass transfer coefficients are very similar for both simulation cases. Both mass transfer coefficient definitions show identical values for the two simulation cases near the gas entry and then slowly deviate. Consequently the difference in computed mass transfer rate between BHPK_2 and BHPK_4 is induced by the difference in specific interface area. The difference between the mass transfer computation approaches is again very big, it accounts for a factor of ~ 20, but it is not as big as seen in the lateral fracture kick scenarios. The concentration of dissolved gas along the annular model section is given in Figure 175 and Figure 176Figure 112. Due to the increase in phase interface area case BHPK_4 deviates more and more from the concentration profile of case BHPK_2. It is the small interfacial structures that are responsible for the accumulation of dissolved gas in simulation case BHPK_4. Finally extrapolating the dissolved gas profiles further up the annulus shows the distance needed to reach full gas saturation of the mud.

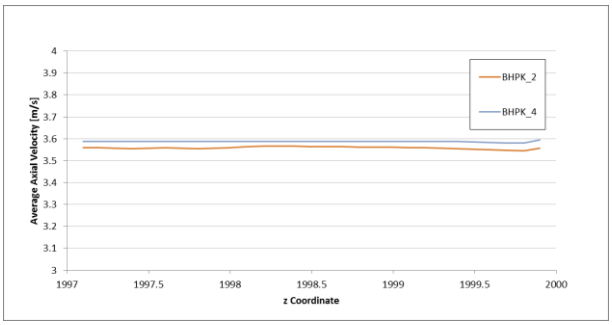


**Figure 167: Average Axial Mixture Velocity**

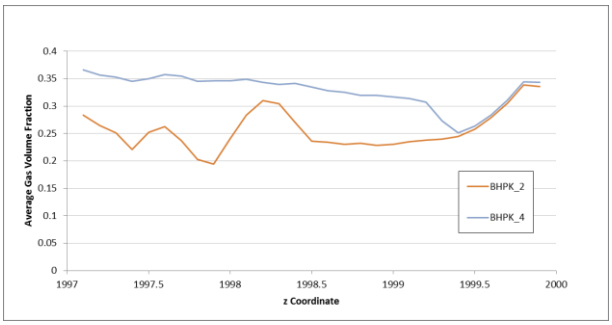


**Figure 168: Average Gas Volume Fraction**

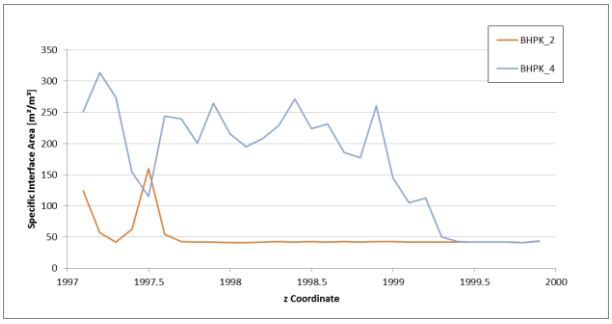


**Figure 169: Specific Interface Area**

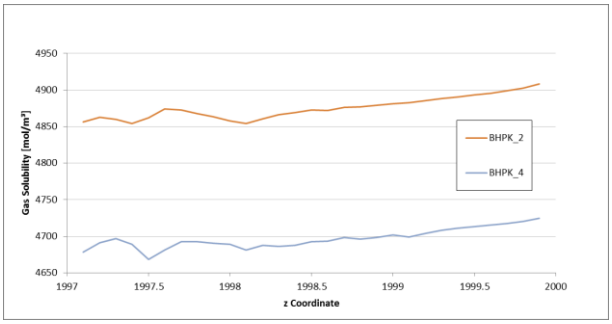


**Figure 170: Gas Solubility**

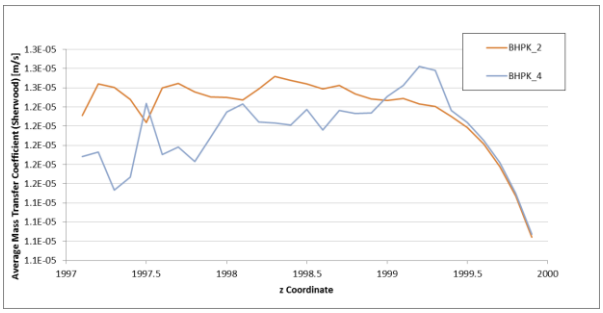


**Figure 171: Average Mass Transfer Coefficient (Sherwood Correlation)**

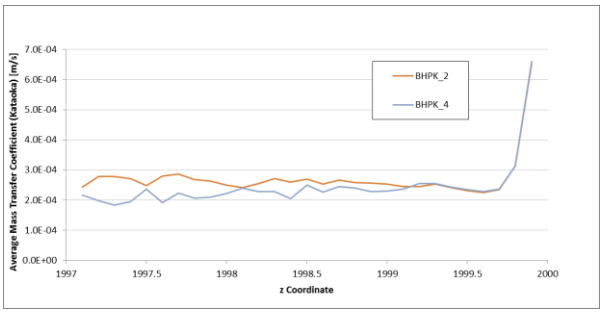


**Figure 172: Average Mass Transfer Coefficient (Kataoka Model)**

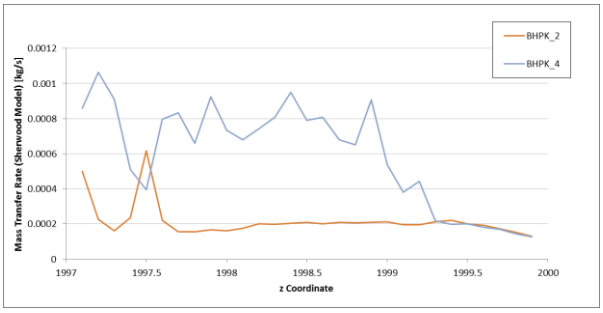


**Figure 173: Mass Transfer Rate (Sherwood Correlation)**

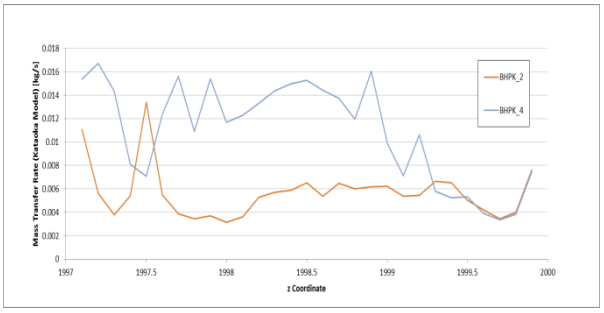


**Figure 174: Mass Transfer Rate (Kataoka Model)**

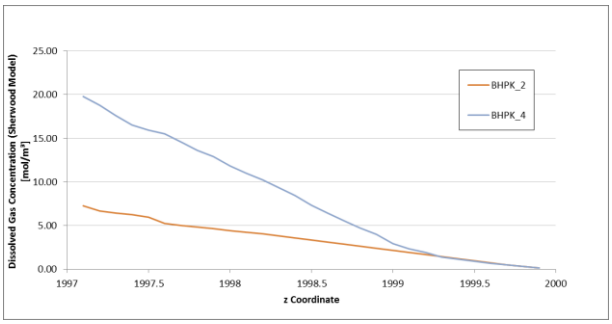


**Figure 175: Dissolved Gas Concentration (Sherwood correlation)**

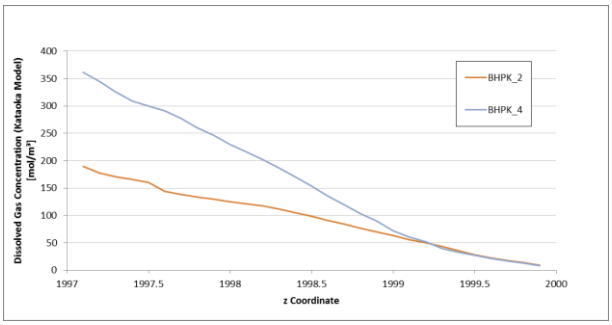


**Figure 176: Dissolved Gas Concentration (Kataoka model)**

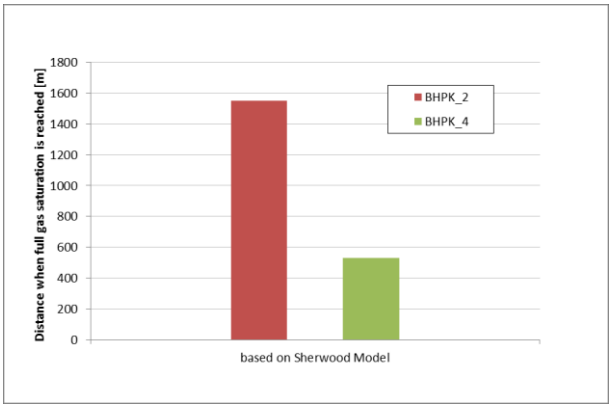


**Figure 177: Distance to Reach Full Mud Saturation (Sherwood Correlation)**

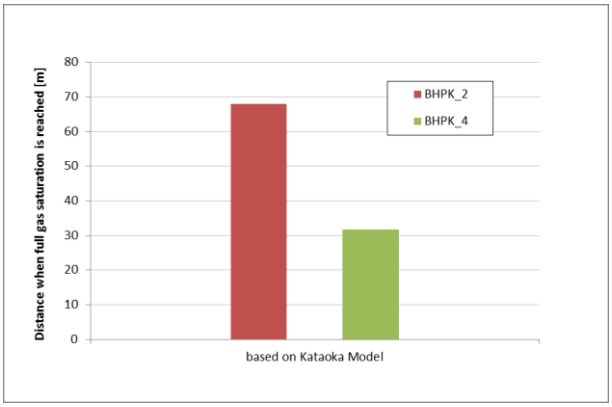


**Figure 178: Distance to Reach Full Mud Saturation (Kataoka Model)**

# 7.Conclusions

The significance of this thesis is to provide a better insight on the two-phase flow situation in a well during a gas-kick and to provide means to assess the corrosive threat. For many applications it is necessary to predict flow patterns as a basis for carrying out calculations on two-phase flow. In the present study it was not the goal to make prior assumptions regarding the evolving flow pattern but instead to gain more insight on two-phase interactions at a close-up view. This thesis describes methodologies to characterize various flow aspects that are of potential interest to corrosion engineers. One of the major difficulties in modeling the corrosive risk to drill pipe during a gas-kick is the determination of the liquid and gas phase distribution in the annulus. As significant chemical reactions are related to the size of the phase interface area, a high resolution CFD simulation focusing on the gas and mud phase distribution is provided. Based on the analysis of these simulation studies, a coarser full scale model of the wellbore including chemical modeling can be established. Basically the kick modeling had to be done without focusing on the validation aspect as such, since no suitable experimental data was available.

Focus of the shown investigations was put on the near drill bit section. This inflow area shows certain characteristics that are dominated by the inflow conditions of the gas as well as by the configuration of the mud stream entering the annulus. After a certain distance, two-phase flow has fully developed and the influence of the gas and fluid inlet configuration is no more dominant. This entrance length accounts approximately 30 times the annular clearance. Stable flow conditions when dealing with time averages have then developed and two-phase flow correlations based on flow pattern maps are becoming valid. The flow pattern map provided by Caetanto (1992) appears to cover well the investigated flow scenarios.

In vertical wellbores the flow pattern will gradually change due to the expansion of the gas caused by the decrease in pressure along the vertical axis. The expansion of gas causes a change in superficial gas velocity along the annulus. Furthermore the sudden inflow of gas into the wellbore represents a transient flow situation, where the steady flow field established by the circulation of the drilling fluid gets interrupted. The magnitude of kick influx is governed by the pressure difference between formation pore pressure and wellbore stagnation pressure at the wellbore-formation interface. While the fluid pressure in the formation will stay more or less constant during the kick, the pressure in the wellbore is subject to change. Two-phase flow patterns mainly depend on the flow rates, geometry and fluid properties of the phases. While the latter two remain more or less the same, it is the flow rates that are continuously changing during a kick. Consequently the two-phase flow pattern will also be subject of change until a new steady flow situation establishes.

As a consequence there is no single flow pattern for an entire wellbore, flow patterns are changing with time and location. Basically the flow regimes will change towards annular flow with decreasing wellbore depth. Based on superficial velocities a range of flow patterns can be defined for a kick event, illustrated as a line in the flow pattern map when the mud rate is

kept constant and no mud is lost to the formation. The starting point is defined by the pressure differential at kick onset and the static bottom-hole pressure affecting gas density. The length of the segment is defined by the difference in bottom-hole and well head pressure. The lower the well head pressure the longer is the range in the flow regime map. However if gas dissolution occurs this line may be interrupted. For instance a kick scenario starts with a bubbly flow regime, gas dissolves and a single phase flow section follows, with decreasing solubility up the annulus gas comes out of solution, starting as dispersed flow but due to gas phase expansion a churn flow period follows until annular flow is reached.

For gas dissolution the influence of flow regime reflected via phase interface area and mass transfer coefficient is the crucial factor. The available phase interface area thus turns out to be the most important parameter to provide a basis for the assessment of corrosive risk.

The gas phase itself has no impact on drill pipe corrosion. It is the water that must be present for sulfide stress cracking to occur. Therefore the simulation model was extended with user defined functions to compute mass transfer due to gas dissolution based on two different modeling approaches. One approach is based on a traditional Sherwood correlation and the other one is based on the model of Kataoka (1969) accounting for the effect of turbulence on mass transfer. The computed values differ considerably. In the Kataoka model fluid motion enhances mass transfer due to turbulence dissipation. In the Shewood approach fluid motion is accounted via a change in fluid viscosity through the rheological model. Basically convection is governing the transport of species to the phase interface, where species are crossing the interface due to diffusion. So increasing convection can enhance the mass transfer rate, but a low diffusion coefficient can be limiting. Convection is enhanced in turbulent flow conditions. Turbulences are transient velocity fluctuations superimposed on the main flow, enhancing momentum and energy transfer and of course the phase mixing process. Turbulences are induced and influenced by drill-string rotation, mud pump-rate, pressure pulsations caused by the drill bit, flow obstacles, rough walls etc..

The modeled kick scenarios discussed in this thesis cover the following flow regimes when allowed to reach steady state:

- Dispersed flow (bubble flow)
- Intermittent flow (churn flow)
- Separated flow (annular flow)

A detailed analysis of the occurring flow phenomena is given including the assessment of specific phase interface area and gas dissolution parameters. The gas dissolution process depends on the local mass transfer coefficient, the available phase interface as well as the current grade of gas-saturation of the mud. The mud is fully saturated when gas concentration is reaching gas solubility, which is a function of pressure and temperature. Basically high mass transfer coefficients occur where gas and mud velocity differ the most. This is typically the case next to the gas inlet location. Gas-kicks with superficial gas velocities categorized in the churn flow regime show annular flow separation near the gas inlet resulting in a minimum

specific surface area at this location. Kicks with even higher superficial gas velocities show an earlier onset of disturbances at the initially well separated gas mud interface resulting in a faster increase of phase interface area. The effect of phase interface area on mass transfer rate is most pronounced for "small kicks" with low gas inflow pressure were dispersion occurs right at the inlet. The expansion of the gas when travelling upwards changes the local void fraction and fluid velocities, and consequently alters the available phase interface area for mass transfer. Basically the mass transfer process is dominated by the available phase interface area. Looking at the overall wellbore it will start at a high rate according to the large difference in concentration between the "fresh mud" and the maximum solubility, and decrease until full saturation is reached. Eventually when the pressure drops below the bubble point gas will be released from the drilling mud.

As a result of the annular velocity field, dissolved gas travels faster in the center of the annulus than at the walls. From a corrosive point of view it is desirable to maintain the amount of dissolved gas low, especially near the drill pipe. Corrosion will occur when the amount of dissolved $H_2S$ exceeds a certain value and the solution is in continuous contact with the drill pipe. The buildup of a laminar and almost pure mud layer along the drill pipe can serve as a protective shield against corrosive attack and is therefore desirable. This can be achieved by controlling the pump rate and surface back pressure to ideally establish an annular flow regime. The mass transfer rate will be lowest for this flow configuration but not zero. The kick entry zone needs to be isolated and the gas already entered into the annulus has to be quickly removed from the wellbore.

## *Suggestions for Future Work*

It has been shown that the upward flow of gas and liquid in a wellbore is accompanied by potential changes in flow patterns affecting the severity of corrosion. The amount of gas that goes into dissolution is small from a volumetric perspective when compared to oil based muds. But already small amounts of dissolved $H_2S$ can pose a potential risk for the drilling equipment, especially if the mud is well mixed with the gas and in continuous contact with the drill pipe. From simulation results it can be seen that as long as mud circulated, the drill pipe is covered with a mud film. This is a desired situation when dealing with oil based muds, but in case of water based muds this can be an unfavorable condition with respect to corrosion. Stagnant or recirculation zones of the flow next to the drilling equipment will suffer reduced exchange of drilling mud and hence elongated exposure times for gas dissolution. Therefore these areas show higher concentrations of dissolved gas than in the free flow. These locations will be spots of increased corrosive potential. Detailed investigations of such spots can help to find design optimizations.

The observation of protective scale formation like Mackinawite iron sulfide on the steel surface is widely mentioned in literature. Models exist to calculate scale formation and damage rates. Fluid mechanical abrasion of protective scales on the drill pipe is increased by certain flow patterns, i.e. slug flow. Film velocity and slug frequency may be utilized as a measure for the fluid mechanical influence on corrosion. With the current simulation

framework such aspects could be incorporated and would pose an interesting area for the extension of the current work.

This work demonstrates tools and methodologies to model the spatial distribution and phase interface area of two-phase flow in a selected section of a vertical wellbore. The models studied in this work are limited in size, due to the high model resolution and the computational cost involved. A full scale wellbore model with equivalent modeling detail is not computationally feasible. To cover the entire wellbore a different approach is needed. As a result of this research effort a combined simulation approach, linking a detailed multiphase flow simulation with a full scale 1-D model is suggested and illustrated in Figure 179. The detailed CFD simulations at subscale are used to set up a database containing correlations and probabilities of parameters applicable to the full scale model.


**Figure 179: Schematic of Model Interaction**

While the high resolution sub-model is meant to provide information on the flow pattern, specific gas-liquid interface area and mass transfer coefficients for a certain model setup (i.e., wellbore configuration and fluid properties), the 1-D wellbore simulator shall determine phase volume fraction, dissolved gas and free gas at any position along the wellbore and the probability and severity of a corrosive impact. Figure 179 shows a schematic of the link between the two modeling levels. The high resolution subscale model feeds a database with flow and corrosion relevant parameters. The full scale 1-D simulator picks relevant parameters like specific interface area and mass transfer coefficients based on 1-D flow variables like i.e., superficial momentum fluxes, from the database.

Future research may focus on the development of the 1-D full scale wellbore model, capable to model the transient nature of a complete gas-kick event, including well control measures set by the operator, i.e. stopping mud pumps and shutting in the well. The reduction in dimension and lumping of parameters provides a considerable reduction in computational time. The 1-D simulator can thus be used to perform dynamic simulations of kick scenarios including all the uncertainty in input parameters. This allows for stochastic analysis of kick events which will be a basis for making corrosion tolerance calculations during well control operations.

There is a large requirement for reliable multiphase flow simulators by the oil and gas industry. Smaller profit margins increase the need for accuracy and planning reliability. Therefore the demand for a more detailed fluid flow simulation continues to grow. With the use of CFD flow situations can be investigated where measurements are not available or experiments are even too difficult to conduct. The design process of new measurement tools for early kick detection can be supported. In this context Computational Fluid Dynamics is a valuable tool to validate measurement approaches, i.e. find best measurement locations and identify key parameters to measure. In general CFD simulations help to better understand and to review assumptions made about the flow conditions in a kicking well.

Existing wellbore simulators provide good planning assistance but the trend for future simulators goes to include risk assessment tools as well as real-time data to optimize well control. Simulators capable to assess the corrosive risk to drilling equipment and to develop strategies on when to replace drill strings will be needed. Especially when encountering sour gas (i.e. hydrogen sulfide) influxes into high-pH drilling fluid systems, the prediction of actual downhole pH development during shut-in and well-killing operations is of prime interest when deciding on potential damage to high-strength drill string components due to sulfide stress cracking.

The need for an adequate decision making tool that permits real-time studies of the effects of risk reducing measures thereby accounting for all the uncertainties involved requires a probabilistic approach. Stochastic modelling of kick scenarios and the analysis of associated corrosive damage probability must be based upon a thorough understanding of the physical phenomena involved. Providing a step towards this fundamental fluid mechanical understanding, with the help of a highly detailed CFD investigation, was given in this work.

# Bibliography

Al-Rawajfeh A.E., *Modelling and Simulation of $CO_2$ Release in Multiple-Effect Distillers for Seawater Desalination*, PhD thesis, Martin-Luther-Universität Halle-Wittenberg, 2004

Anglart H., Podowski M.Z., *Fluid Mechanics of Taylor Bubbles and Slug Flows in Vertical Channels*, Nuclear Science and Engineering, Vol. 140, 2002

ANSYS, Multiphase Flow Conference, HZDR Dresden Rosdorf, Nov. 2015

ANSYS FLUENT, User Guide Manual 14.5, http://www.ansys.com/Products/Fluids/ANSYS-Fluent, 2015

Barnea D., *A unified model for predicting flow-pattern transitions for the whole range of pipe inclinations*, International Journal of Multiphase Flow, Volume 13, Issue 1, 1987

Bendiksen K., Brandt I., Jacobsen K.A., Pauchon C., *Dynamic simulation of multiphase transportation systems*, Multiphase Technology and Consequences for Field Development Forum, Stavanger, Norway, 1987

Bennett A.W., Hewitt G.F., Kearsey H.A., Keeys R.K.F. and Lacey M.P.C., *Flow visualisation studies of boiling at high pressure*, Proc. Inst. Mech. Eng., 180 (Part 3C), 1965

Brennen C.E., *Fundamentals of Multiphase Flows*, Cambridge University Press, 2005

Butterwoth D. and Hewitt G.F., *Two Phase Flow and Heat Transfer*, Oxford University Press, 1977

Benediksen K.H., Maines D., Moe R., Nuland S., *The Dynamic Two-Fluid Model OLGA: Theory and Application*, SPE production Engineering, May 1991

Caetano E.F., Shoham O., Brill J.P., *Upward Vertical Two-Phase Flow through an Annulus – Part I: Single-Phase Friction Factor, Taylor Bubble Rise Velocity, and Flow Pattern Prediction*, Journal Energy Resources Tech., Vol. 114, March, 1-13, 1992

Caetano E.F., Shoham O., Brill J.P., *Upward Vertical Two-Phase Flow through an Annulus – Part II: Modelling Bubble, Slug, and Annular Flow*, Journal Energy Resources Tech., Vol. 114, March, 14-30, 1992

Campos J.B.L.M., Guedes de Carvalho J.R.F., *An experimental study of the wake of gas slugs rising in liquids*, Journal of Fluid Mechanics, Vol. 196, 1988

Chen L., Tian Y.S., Karayiannis T.G., *The effect of tube diameter on vertical two-phase flow regimes in small tubes*, International Journal of Heat and Mass Transfer 49, 2006

Chilingar G.V., Mourhatch R., Al-Qahtani G.D., *The Fundamentals of Corrosion and Scaling for Petroleum & Environmental Engineers*, Gulf Publishing Company, 2008

Chilingar G.V., Vorabutr P., *Drilling and Drilling Fluids*, Elsevier Science Ltd, 1981

Clarke A., Issa R. I., *Numerical Model of Slug Flow in Vertical Tubes*, Computers & Fluids, Vol. 26(4), 1997

Cussler E.L., *Diffusion: Mass Transfer in Fluid Systems*, Cambridge University Press, 2009

Duan Z., Sun r., Liu r., Zhu C., *Accurate Thermodynamic Model for the Calculation of $H_2S$ Solubility in Pure Water and Brines*, Energy & Fuels, 21, 2056 – 2065, 2007

Dukler A.E. and Taitel W., *Flow Pattern Transitions in Gas-Liquid Systems: Measurement and Modelling*, Chapter 1 of Multiphase Science and Technology, Vol. 2, Hemisphere Publishing Corporation, 1986

Fair J.R., *What you need to know to design thermosyphon reboilers*, Petroleum Refiner 39, 1960

Fernandes R.C., *Experimental and Theoretical Studies of Isothermal Upward Gas-Liquid Flows in Vertical Tubes*, Ph.D. Dissertation, University of Houston, Chemical Engineering Department, 1981

Fraser D., Lindley R., Moore D., Staak M., *Early Kick Detection Methods and Technologies*, SPE Annual Technical Conference and Exhibition, Amsterdam, October 2014

Griffith P., Wallis G.B., *Two-Phase Slug Flow*, ASME, Journal of Heat Transfer, Vol. 83, 1961

Hall-Taylor N.S., Hewitt G.F., Lacey P.M.C., *The motion and frequency of large disturbance waves in annular two-phase flwo of air-water mixtures*, Chem. Eng. Sci., 18, 537, 1963

Hewitt G.F., *Handbook of Multiphase Systems*, Chapter 2, Hemisphere Publishing Corporation, New York, 1982

Hewitt G.F., Hall-Taylor N., *Annular Two-Phase Flow,* Oxford: Pergamon Press, 1972

Hewitt G.F., Jayanti S., *To Churn or Not To Churn*, International Journal of Multiphase Flow, Vol. 19, No. 3, 1993

Hewitt G.F., King R.D., Lovegrove P.C., *Liquid film and pressure drop studies*. Chem. Proc. Eng., 45, 191, 1964

Hewitt G.F., Robertson D.N., *Studies of Two-Phase Flow Patterns by Simultaneous X-ray and Flash Photography*, Rept. AERE-M2159, UKAEA, Harwell, 1969

Hibiki T., Ishii M., *Two-group interfacial area transport equations at bubbly-to-slug flow transitions*, Nucl. Eng. Des., 202, 39-76, 2000

Hirt C.W., Nichols B.D., *Volume of Fluid (VOF) method for the dynamics of free boundaries*, J. Comp Phys, Vol. 39, 1981

Hovland F., Rommetveit R., *Analysis of Gas-Rise Velocities from Full-Scale Kick Experiments*, 67th Annual Technical Conference and Exhibition of the Society of Petroleum Engineers, Washington, DC. October 4-7, 1992

Hubbard M.G., Dukler A.E., *The characterization of flow regimes for horizontal two-phase flow: statistical analysis of wall pressure fluctuations*, Proceedings of the 1966 Heat Transfer and Fluid Mechanics Institute, pp. 100–121, 1966

Ishii M., *Thermo-fluid dynamic theory of two-phase flow*, Collection de la Direction des Etudes et Researches d'Electricite de France, Eyrolles, Paris, France, 1975

Ishii M., Hibiki T., *Thermo-Fluid Dynamics of Two-phase Flow*, Springer, New York, USA, 2010

Julia J. E., Hibiki T., *Flow regime transition criteria for two-phase flow in a vertical annulus,* International Journal of Heat and Fluid Flow, 32, 2011

Johnson A.B., Cooper S., *Gas Migration Velocities During Gas Kicks in Deviated Wells*, 68th Annual Technical Conference and Exhibition of the Society of Petroleum Engineers, Houston, Texas, 3-6 October 1993

Johnson A. B., White D.B., *Gas Rise Velocities During Kicks*, SPE 20431, SPE Drilling Engineer, December 1991

Jones O.C., Zuber N., *The Interrelation between Void Fraction Fluctuations and Flow Patterns in Two-Phase Flow*, Int. I. Multiphase Flow, Vol. 2, pp. 273-306, 1975

Kataoka H., Miyauchi T., *Gas absorption into the free liquid surface of water tunnel in turbulent region*, Kagaku-Kogaku, 33, pp. 181–186, 1969

Kawaji M. et al., *Investigation of Flow Structures in Vertical Slug Flow*, Nuclear Engineering and Design, Vol. 175, 1997

Kreith F., Berger S.A., et al., "*Fluid Mechanics"Mechanical Engineering Handbook,* Ed. Frank Kreith, Boca Raton: CRC Press LLC, 1999

Mao Z.S., Dukler, A. E., *The Motion of Taylor Bubbles in Vertical Tubes. I. A Numerical Simulation for the Shape and Rise Velocity of Taylor Bubbles in Stagnant and Flowing Liquid*, Journal of Computational Physics, Vol. 91, 1990

McQuillan K.W., Whalley P.B., *Flow Patterns in Vertical Two-Phase Flow*, International Journal of Multiphase Flow, Vol. I 1, No. 2, 1985

O'Brien T.B., *Handling Gas in an Oil Mud Takes Special Precautions*, World Oil, 1981

OLGA: https://www.software.slb.com/products/olga

Owen, D.G., *An experimental and theoretical analysis of equilibrium annular flows*, Ph.D. Thesis, University of Birmingham, UK, 1986

Ozar B., Jeong J.J., Dixit A., Juliá J.E., Hibiki T., Ishii M., *Flow structure of gas-liquid two-phase flow in an annulus*, Chemical Engineering Science 63, p. 3998-4011, 2008

Pauchon C., Dhulesia H., Lopez D., Fabre J., *TACITE: A comprehensive mechanistic model for two-phase flow*, Proceedings of the 6th International Conference on Multiphase Production, Cannes, France, 1993

Pauchon C., Dhulesia H., Binh-Cirlot G. and Fabre J., *TACITE: A transient tool for multiphase pipeline and well simulation*, SPE Annual Technical Conference, New Orleans, LA, USA, 1994

Pilliod J.E., Puckett E.G., *Second-order accurate volume-of-fluid algorithms for tracking material interfaces*, Journal of Computational Physics, Vol. 199, 2004

Rommetveit R., Olsen T.L., *Gas Kick Experiments in Oil-Based Drilling Muds in a Full-Scale, Inclined Research Well*, SPE 19561, 64th Annual Technical Conference and Exhibition of the Society of Petroleum Engineers, San Antonio, TX, October 8-11, 1989

Schicht, H.H., *Flow patterns for an adiabatic two-phase flow of water and air within a horizontal tube*, Verfahrenstechnik, 3, No.4, 1969

Schmidtke M., *Untersuchung der Dynamik fluider Partikel auf Basis der Volume of Fluid Methode*, Dissertation, Department Chemie, Universität Paderborn, 2009

Serizawa A., Kataoka I., *Phase Distribution in Two-Phase Bubbly Flow*, ICHMT Int. Sem. Transient Two-Phase Flow, Dubrovnik, Yugoslavia, 177, 1987

Shyy W., Udaykumar H.S., Rao M.M., Smith R. W., *Computational Fluid Dynamics with Moving Boundaries*, Taylor & Francis, Bristol, Pennsylvania, 1996

SINTEF Flow Loops, website: www.sintefloops.com

Srinivasan S., Kane R., *Prediction of corrosivity of $CO_2/H_2S$ production environments*, NACE International Corrosion Conferenc & Expo, 1996

Stenberg O., Andersson B., *Gas-liquid mass transfer in agitated vessels - II. Modelling of gas-liquid mass transfer,* Chem. Eng. Sci. 1988; 43: 725-730.

Sun W., Nesic S., *A mechanistic model of H2S corrosion of mild steel*, NACE International Corrosion Conference & Expo, 2007

Taha T., Cui Z.F., *CFD modelling of slug flow in vertical tubes*, Chemical Engineering Science, Vol. 61, 2006

Taitel Y., *Advances in Two Phase Flow Mechanistic Modeling*, University of Tulsa Centennial Petroleum Engineering Symposium, Tulsa, Oklahoma, August 1995

Taitel Y., Barnea D. and Dukler A.E., *Modeling Flow Pattern Transitions for Steady Upward Gas-Liquid Flow in Vertical Tubes*, AIChE Journal 26, no. 6, May 1980

Taitel Y., Dukler A.E., *A model for prediction flow regime transitions in horizontal and near horizontal gas–liquid flow*, AIChE Journal 22, 1976

*Thermopedia: A-to-Z Guide to Thermodynamics, Heat and Mass Transfer, and Fluids Engineering*, Begellhouse, Digital Library, 2006

Tong L.S. and Tang Y.S., *Boiling Heat Transfer and Two Phase Flow*, CRC Press, 1997

Ubbink O., *Numerical prediction of two fluid systems with sharp interfaces*, Dissertation, Department of Mechanical Engineering, Imperial College of Science, London University, 1997

Viana F., Pardo R., Ýanez R., Trallero J., Joseph D., *Universal correlation for the rise velocity of long gas bubbles in round pipes*, Journal of Fluid Mechanics, Vol. 494, 2003

Waclawczyk T., Koronowicz T., *Modeling of the flow in systems of immiscible fluids using Volume of Fluid method with CICSAM scheme*, Turbulence, Vol. 8, 2005

Wallis G.B., *One dimensional two phase flow*, McGraw-Hill, New York, 1969

Wang S., Nesic S., *On coupling CO2 Corrosion and Multiphase Flow Models*, Corrosion 2003, Paper No. 03631

Weisman J., Duncan D., Gibson J., Crawford T., *Effects of fluid properties and pipe diameter on two-phase flow patterns in horizontal lines*, International Journal of Multiphase Flow 5, 1979

Weisman J., Kang S., *Flow pattern transitions in vertical and upwardly inclined lines*, International Journal of Multiphase Flow 7, 1981

Whalley P.B., *Two Phase Flow and Heat Transfer*, Oxford University Press, 1996

Whalley P.B., *Boiling and Condensation and Gas-Liquid Flow*, Clarendon Press, Oxford, 1987http://dx.doi.org/10.1017/S0022112088211739

Xiaodong Z., *Mechanistic-based models for slug flow in vertical pipes*, Dissertation, 2005

Youngs D.L., *Time-dependent multi-material flow with large fluid distortion*. In: Morton K.W., Baibnes M.J. (Eds.), Numerical Methods for Fluid Dynamics. Academic Press, New York, p. 273, 1982

Zheng L., Yapa P.D., Chen F., *A model for simulating deepwater oil and gas blowouts – Part I: Theory and model formulation*, Journal of Hydraulic research, Vol. 41, No. 4, 2002

Zuber N., Findlay J.A., *Average volumetric concentration in two phase flow system*, ASME, Journal of Heat Transfer, Vol. 87, 1965